SSC-EOI0003
SDC-90-00085

C
I
03

ary
e
y

SSCL-SR-1158
SSC-EOI0003

Solenoidal Detector Collaboration

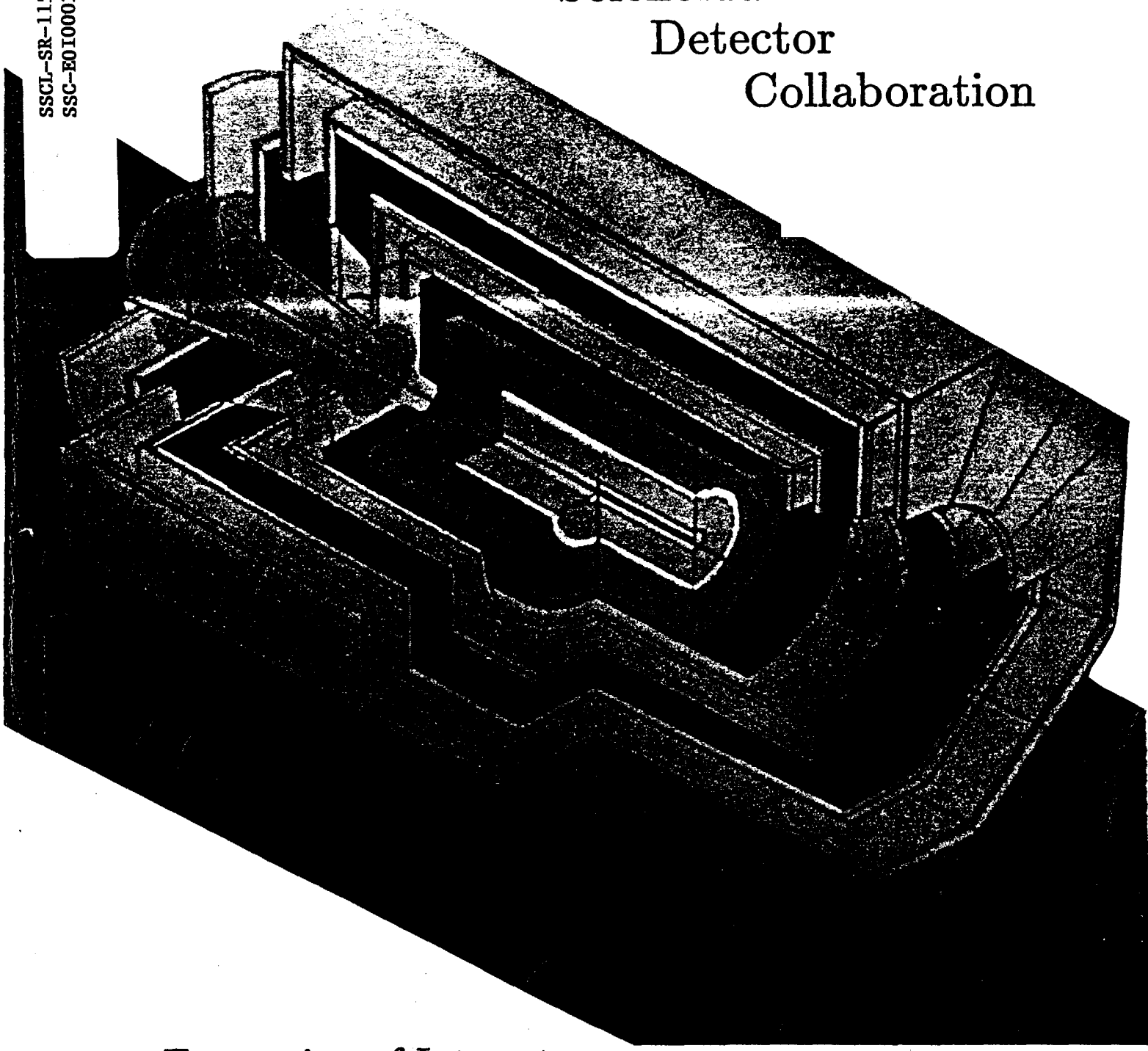

Expression of Interest
24 May 1990

Expression of Interest
by the
SOLENOIDAL DETECTOR COLLABORATION
to construct and operate a detector at the
Superconducting Super Collider
24 May 1990

Summary

A general-purpose detector for a high-luminosity interaction region at the SSC will be proposed by the Solenoidal Detector Collaboration (SDC). The proposed detector is not only optimized for high-p_t physics, where processes beyond the context of the standard model are most likely to be observed, but also has diverse capabilities that make it a premier exploratory tool well matched to the opportunities and potential surprises of a totally new energy domain. Its solenoidal magnet, calorimetry, and central tracking system borrow heavily from the highly successful CDF experience. The solenoid and tracking provide the means for charged particle measurement and for monitoring the performance of other detecting elements. Outside the magnet is a high-performance calorimeter, followed by an iron toroid magnet and a set of muon tracking detectors. These systems identify and measure electrons, muons, and jets with transverse momenta above a few GeV/c for $|\eta| < 3$. We are studying the possibility of using air-core toroidal magnets to improve the precision of muon momentum measurements in the region $1.5 < |\eta| < 2.5$. Forward calorimetry covering the pseudorapidity region $3 < |\eta| < 5$ provides information on missing transverse energy. We are keeping open several technological options for both calorimetry and tracking, as well as some of the details of the solenoid configuration. Members of our collaboration are engaged in vigorous R&D efforts to provide the technical basis for choices among these options to be incorporated in our proposal. The SDC plans to have the detector in place and operational in time to take advantage of the first physics opportunities provided by SSC operation.

Contact person:

George H. Trilling, Spokesperson
50A-2160 Lawrence Berkeley Laboratory
Berkeley CA 94720
415/486-6801, Bitnet GHT@LBL

Members of the Solenoidal Detector Collaboration

Argonne National Laboratory: E. L. Berger, R. E. Blair, J. W. Dawson, M. Derrick, T. H. Fields, R. T. Hagstrom, N. F. Hill, P. Job, T. B. Kirk, E. N. May, L. J. Nodulman, L. E. Price, J. Proudfoot, H. M. Spinka, R. L. Talaga, H.-J. Trost, D. G. Underwood, R. G. Wagner, A. B. Wicklund

University of Arizona: K. A. Johns

Brandeis University: S. Behrends, J. R. Bensinger, C. Blocker, P. Kesten, L. Kirsch

Bratslava State University, Checkoslovakia: P. Povinec, P. Strmen

University of Bristol: B. Foster, G. P. Heath

Brown University: D. Cutts, R. Partridge

University of California at Davis: D. Pellett

University of California at Los Angeles: K. Arisaka, D. Chrisman, D. Cline, J. Park, D. Roberts, W. Slater, H. Yamamoto

University of California at Riverside: J. Ellison, S. J. Wimpenny,

University of California at San Diego: M. Sivertz, D. Thomas

University of California at Santa Cruz: D. Dorfan, C. Heusch, B. Hubbard, A. L. Litke, W. Lockman, D. Pitzl, H. Sadrozinski, A. Seiden

Chiba University: H. Kawai

University of Chicago: C. Campagneri, S. Eno, H. Frisch, C. Gross-Pilcher, M. Miller, L. Rosenberg, M. Shochet, G. Sullivan

University of Colorado: G. J. Baranko, J. Carr, H. W. K. Cheung, J. P. Cumalat, W. T. Ford, U. Nauenberg, P. Rankin, J. G. Smith

*Joint Institute for Nuclear Research, Dubna, USSR:*V. I. Astakhov, B. V. Batyunia, A. Bischoff, Y. A. Budagov, K. G. Denisenko, N. L. Denisenko, S. B. Gerasimov, V. M. Golovatyuk, Z. Guzik, D. I. Hubua, R. B. Kadyrov, Y. N. Kharzheev, I. F. Kolpakov, A. D. Kovalenko, F. V. Levchanovsky, Y. F. Lomakin, A. I. Malakhov, A. A. Omelianenko, Y. A. Panebratsev, I. V. Puzynin, A. A. Semenov, A. E. Senner, V. T. Sidorov, A. N. Sinaev, A. N. Sissakian, V. A. Smirnov, T. Spassoff, E. N. Tsyganov, I. A. Tyapkin, G. V. Velev, V. B. Vinogradov, A. S. Vodopianov, V. Vrba, Y. V. Zanevsky, N. I. Zhuravlev, N. I. Zimin, A. I. Zinchenko

Duke University: L. R. Fortney, A. T. Goshaw, W. Kowald, S. H. Oh, W. J. Robertson, W. D. Walker

Erevan Institute of Physics, USSR: A. C. Amatuni, G. A. Vartgapetian

Fermilab: D. Amidei, M. Atac, A. E. Baumbaugh, A. Beretvas, R. Bernstein, M. Binkley, A. D. Bross, A. G. Clark, J. W. Cooper, D. P. Eartly, J. E. Elias, R. W. Fast, D. Finley, G. W. Foster, J. Freeman, I. Gaines, S. A. Gourlay, D. R. Green, S. R. Hahn, R. M. Harris, J. Hauser, J. Huth, R. D. Kephart, J. Kuzminski, P. S. Martin, M. Mishina, A. Mukerjee, T. Nash, C. Newman-Holmes, A. Para, J. Patrick, R. Plunkett, E. E. Schmidt, S. L. Segler, S. Tkaczyk, R. Vidal, R. L. Wagner, G. P. Yeh, J. Yoh

University of Florida: R. Field, J. Harmon, J. Walker

Florida State University: M. Corden, V. Hagopian, K. Johnson, H. Wahl

Fukui University: M. Kawaguchi, H. Yoshida

Gomel State University, USSR: A. M. Dvornik, N. B. Maksimenko

Harvard University: G. Brandenburg, G. Feldman, M. Franklin, S. Geer, J. Konigsberg, J. Oliver, T. Phillips, R. Wilson

University of Hawaii: C. Kenney, S. Parker

Hiroshima University: Y. Chiba, T. Ohsugi

Hiroshima Institute of Technology: M. Asai

Ibaraki College of Technology: M. Shioden

University of Illinois at Chicago: H. Goldberg, S. Margulies, J. Solomon

University of Illinois at Urbana: R. Downing, S. Errede, A. Gautier, M. Haney, L. Holloway, I. Karliner, A. Liss, T. O'Halloran, J. Thaler, P. Sheldon, V. Simaitis, J. Wiss

Indiana University: D. Blockus, B. Brabson, A. Dzierba, G. Hanson, X. Lou, H. Ogren, D. Rust,

Iowa State University: J. Hauptman

Johns Hopkins University: J. A. Bagger, B. A. Barnett, B. J. Blumenfeld, P. H. Fisher, J. A. J. Matthews

National Laboratory for High Energy Physics (KEK): F. Abe, K. Amako, Y. Arai, Y. Doi, H. Fujii, Y. Fukui, T. Haruyama, H. Ikeda, M. Ikeda, S. Inaba, T. Inagaki, H. Iwasaki, S. Kabe, J. Kanzaki, S. K. Kim, T. Kondo, A. Maki, A. Manabe, M. Mishina, M. Noumachi, S. Odaka, K. Ogawa, Y. Sakai, H. Sakamoto, T. Shinkawa, Y. Takaiwa, S. Terada, T. Tsuboyama, K. Tsukada, N. Ujiie, Y. Unno, Y. Watase, A. Yamamoto, Y. Yasu

Slovak Academy of Science, Košice, Czechoslovakia: F. Krivan, M. Seman, J. Špalek

Kyoto University: R. Kikuchi, K. Miyake

Lawrence Berkeley Laboratory: G. S. Abrams, A. Barbaro-Galtieri, R. M. Barnett, R. N. Cahn, P. H. Eberhard, K. Einsweiler, R. Ely, M. G. D. Gilchriese, D. E. Groom, C. Haber, C. Hearty, I. Hinchliffe, R. W. Kadel, J. A. Kadyk, M. E. Levi, P. J. Limon, S. C. Loken, D. R. Nygren, A. P. T. Palounek, M. Pripstein, M. Shapiro, J. L. Siegrist, H. G. Spieler, M. Strovink, G. H. Trilling, E. M. Wang, W. A. Wenzel

University of Liverpool: J. Bailey, G. A. Beck, J. B. Dainton, E. Gabathuler, S. J. Maxfield

University of Maryland: A. R. Baden, A. H. Ball, C. Y. Chang, D. G. Fong, J. A. Goodman , N. J. Hadley, A. Jawahery, R. G. Kellogg, S. Kunori, A. Skuja, G. T. Zorn

University of Michigan: R. C. Ball, M. Campbell, J. Chapman, H. R. Gustafson, S. Hong, L. W. Jones, M. J. Longo, M. R. Marcin, H. A. Neal, D. Nitz, B. P. Roe, G. Snow, R. Thun

University of Minnesota: P. Border, H. Courant, K. Heller, Y. Kubota, M. Marshak, E. Peterson, R. Poling, K. Ruddick

Academy of Science of BSSR, Minsk, USSR: J. A. Kulchitsky, L. G. Moroz

University of Mississippi: D. Moore, D. Summers

Miyazaki University: T. Nakamura

Nagoya University: M. Nakamura, K. Niwa

Niigata University: K. Miyano, H. Miyata

University of Notre Dame: J. Bishop, N. Biswas, N. Cason, J. Godfrey, V. P. Kenney, J. Piekarz, R. Ruchti, W. Shepard

Oak Ridge National Laboratory: G. Alley, R. G. Alsmiller, Jr., F. S. Alsmiller, C. Y. Fu, C. W. Glover, D. Vandergriff

Ohio State University: B. Byslma, L. S. Durkin, T. Y. Ling, S. K. Park, T. A. Romanowski

Okayama University: N. Tamura

Osaka City University: T. Okusawa, T. Takahashi, Y. Teramoto, T. Yoshida

Osaka University: Y. Nagashima, S. Sugimoto

University of Oxford: R. Cashmore, N. Harnew, R. Nickerson, A. Weidberg, W. Williams

University of Pennsylvania: L. Gladney, R. J. Hollebeek, M. Newcomer, K. J. Ragan, P. K. Sinervo, H. H. Williams

Pennsylvania State University: T. A. Armstrong, K. W. Hartman, A. Hasan, S. F. Heppelmann, R. A. Lewis, E. D. Minor, B. Y. Oh, G. A. Smith, W. S. Toothacker, J. Whitmore

University of Pisa: R. Amendolia, F. Bedeschi, G. Bellettini, S. Galeotti, H. Grassman, M. Mangano, A. Menzione, G. Pauletta, D. Passuello, G. Punzi, L. Ristori

University of Pittsburgh: E. E. Engels, Jr., T. Humanic, S. Mani, P. F. Shepard

Purdue University: V. E. Barnes, A. F. Garfinkel, D. S. Koltick, A. T. Laasanen, R. McIlwain, D. H. Miller, E. Shibata, I. P. Shipsey

Rice University: D. Adams, S. Ahmad, B. Bonner, M. Corcoran, H. Miettinen, G. Mutchler, J. Roberts, J. Skeens

University of Rochester: A. Bodek, F. Lobkowicz, A. Sill, P. Slattery, E. H. Thorndike

Rockefeller University: N. Giokaris, D. Goulianos, P. Melese, R. Rusack, S. White

Rutgers University: T. Devlin, T. Watts

Rutherford Appleton Laboratory: N. Gee, J. Harvey

Saga University: A. Murakami, S. Kobayashi

Saitama College of Health: K. Masuda

Sofia State University, Bulgaria: R. V. Tsenov, A. B. Iordanov

Stanford Linear Accelerator Center: A. Lankford

Superconducting Super Collider Laboratory: D. Bintinger, H. Johnstad

Physical Technical Institute, Tashkent, USSR: Sh. Aliev, M. Alimov, K. Gulamov, S. Kan, V. Kaprior, A. Khaneles, V. Myalkovski, A. Pak, E. Surlin, K. Turdaliev, A. Yuldashev, B. Yuldashev

Institute of High Energy Physics, Tbilisi State University, USSR: N. S. Amaglobely, B. G. Chiladze, D. I. Hubua, R. G. Salukvade

Texas A&M University: P. M. McIntyre, T. Bowcock, F. R. Huson, J. T. White

University of Texas at Dallas: R. C. Chaney, E. J. Fenyves, H. Hammack, J. Orgeron, W. B. Lowery, N. P. Johnson,

Tohoku Gakuin University: M. Higuchi, Y. Hoshi

Tohoku University: K. Abe, K. Hasegawa, H. Yuta

University of Tokyo (Institute for Nuclear Study): S. Kato, K. Nishikawa, S. Homma, T. Miyachi

Tokyo Institute of Technology: Y. Watanabe, T. Tanimori

Tokyo Metropolitan University: M. Chiba, R. Hamatsu, T. Hirose, S. Kitamura

Tokyo University of Agriculture and Technology: T. Emura, K. Takahashi

University of Tsukuba (Institute of Physics): Y. Funayama, K. Hara, S. Kanda, T. Kaneko, S. Kim, K. Kondo, T. Mimashi, S. Miyashita, Y. Morita, I. Nakano, H. Sakurabata, K. Takikawa, K. Yasuoka

University of Tsukuba (Institute of Applied Physics): Y. Asano, S. Mori, Y. Takada

Tufts University: T. Kafka, W. A. Mann, R. H. Milburn, A. Napier, K. Sliwa

Virginia Polytechnic Institute: B. Lu, L. W. Mo, L. E. Piilonen

Wakayama Medical College: M. Daigo

University of Washington: R. J. Davisson, G. Liang, H. J. Lubatti, R. J. Wilkes T. Zhao,

University of Wisconsin: J. Bellinger, D. Carlsmith, A. Erwin, C. Foudas, R. Handler, R. Loveless, G. Ott, D. D. Reeder, W. Smith, C. Wendt, S. L. Wu

Table of Contents

1. Introduction . . . 1
2. Physics goals . . . 3
   2.1. Introduction . . . 3
   2.2. Electroweak symmetry breaking . . . 4
   2.3. The t quark . . . 6
   2.4. New, heavy bosons . . . 6
   2.5. Quark and lepton substructure . . . 7
   2.6. Supersymmetry . . . 7
3. Detector overview . . . 8
   3.1. General detector requirements . . . 8
   3.2. Detailed reasons for a solenoid . . . 9
   3.3. Determination of detector configuration and scale . . . 9
   3.4. Critical detector issues . . . 10
   3.5. Detector description . . . 12
   3.6. Radiation environment . . . 19
   3.7. High-luminosity potential . . . 21
4. Detector subsystems . . . 22
   4.1. Tracking . . . 22
   4.2. Solenoid magnet . . . 31
   4.3. Calorimetry . . . 38
   4.4. Electron identification . . . 49
   4.5. Muon system . . . 50
   4.6. Electronics, trigger, and data acquisition . . . 54
   4.7. Computing, software, and networking . . . 64
5. Detector Performance . . . 68
   5.1. Methodology and overview . . . 68
   5.2. Definition of detector parameters for simulation . . . 69
   5.3. Examples of detector performance . . . 70
   5.4. Simulation work to be done . . . 84
6. Detector assembly, facilities and test beam requirements . . . 86
   6.1. Assembly of detector components . . . 86
   6.2. Test beam requirements . . . 89
7. Detector cost and schedule estimates . . . 90
8. Organization and management of the collaboration . . . 93
   8.1. Governance . . . 93
   8.2. Structure and responsibilities . . . 95
   8.3. Procedures for admission of new members . . . 95
9. Preparation of the proposal and budget request . . . 97
   9.1. Preparation of the proposal . . . 98
   9.2. Budget request . . . 104
10. References . . . 105

1. Introduction

This document is an Expression of Interest submitted by the Solenoidal Detector Collaboration (SDC) for a detector aimed at pursuing a broad range of physics at the SSC. The proposed detector is not only optimized for high-p_t physics, which provides the principal motivation for building the SSC, but also has diverse capabilities that make it a premier exploratory tool for a wide range of physics, even in the operating period before the luminosity has reached its design value.

As a solenoidal detector with powerful calorimetry, tracking, and muon detection, the SDC detector draws heavily on the very positive CDF experience at a hadron collider. The solenoid and its associated tracking system provide all-important redundancy through measurements of charged particles and monitoring of the performance of the other detecting elements. Since the events of interest will represent a minute fraction of all interactions, this redundancy plays a vital role in establishing the credibility of important new observations.

The proposed detector will identify and measure electrons, muons, and jets with transverse momenta above a few GeV/c over the pseudorapidity range $|\eta| < 3$. To allow determination of missing transverse energy, additional calorimetry is planned covering pseudorapidities up to about five.

While the basic design concept of the detector is determined, we are keeping open a number of technological options, especially in calorimetry and tracking, to take advantage of R&D efforts presently under way. Some details of the solenoid configuration are also open. Cost estimation is still in a very rudimentary state, but eventually cost/benefit optimization will play an important role in the development of the detector design. To proceed beyond the EoI stage to the proposal, continuation of the present subsystem R&D efforts will be important, as will the support of engineering efforts to establish costs, schedules, and to provide for integration of the whole detector concept. A request for such support is developed in later sections of this EoI.

The SDC presently consists of about 300 physicists from U.S. universities and national laboratories plus around 100 physicists from KEK and universities in Japan, and about 80 scientists from Bulgaria, Czechoslovakia, Italy, the Soviet Union, and the United Kingdom. Most of these physicists are presently spending part of their time on other experiments, but expect to put in significant effort on this detector, either directly or through relevant subsystem R&D efforts. A governance document, which has been ratified by the collaboration, provides an overall management structure. Most of this structure is already in place. Thus the SDC is ready to move forward, expand its membership as appropriate, and develop a strong proposal for a detector that will be operational at SSC turnon.

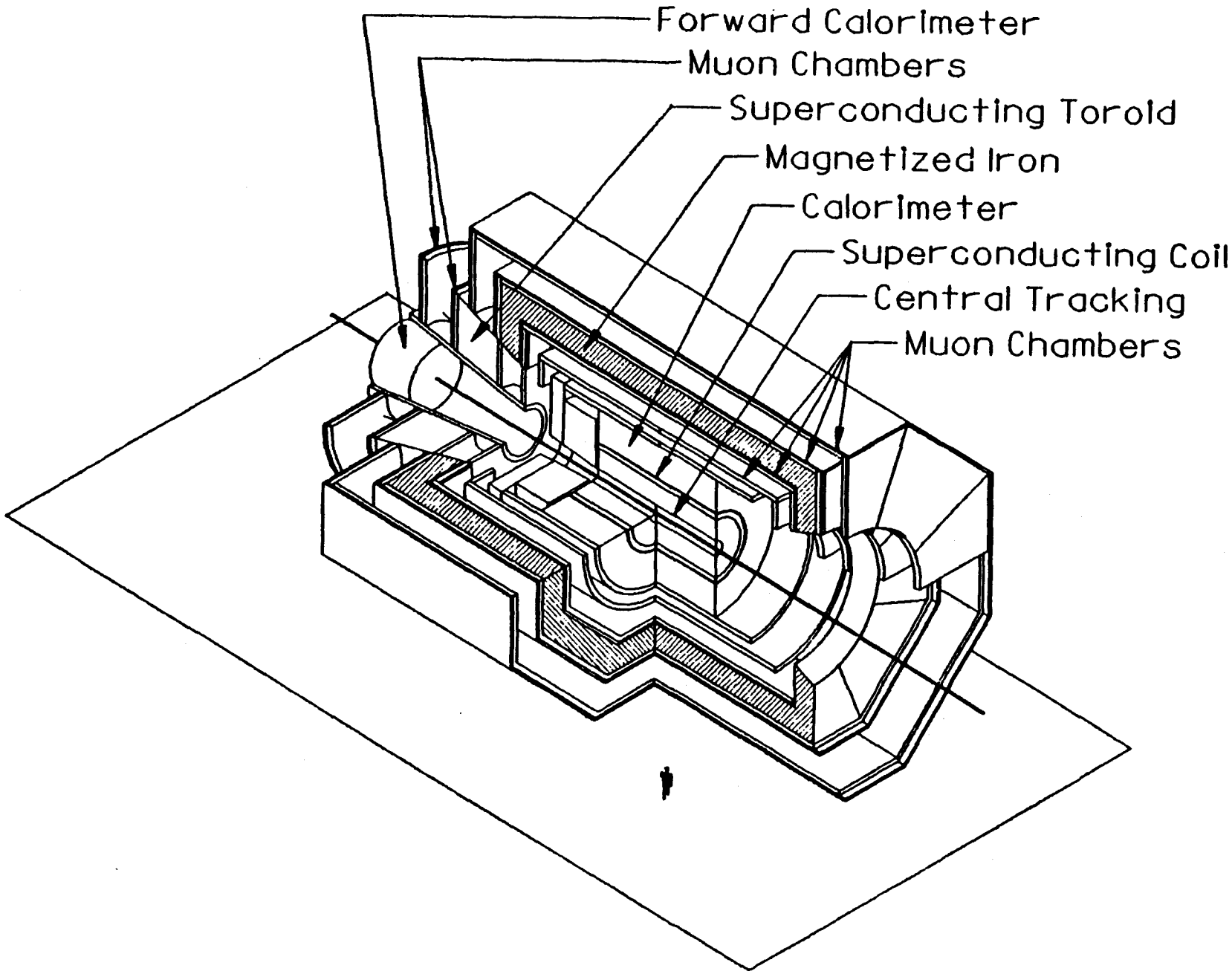

FIG. 1. Cutaway view of the SDC detector.

FIG. 1. Cutaway view of the SDC detector.

2. Physics goals

2.1. Introduction

The SSC will provide unprecedented collision energies and intensities when it begins operation at the turn of the century. Compared to the present frontier collider facility, the Fermilab Tevatron, the SSC will extend the energy reach of experimental particle physics by a factor of twenty, while providing collision rates that are three orders of magnitude higher. This leap in collider performance is almost certain to open up new frontiers in particle research even if the precise nature of possible discoveries cannot now be foreseen. We are therefore proposing a detector which can observe a broad range of physical phenomena.

This detector, shown in Fig. 1, consists of a large magnetic spectrometer surrounded by calorimeters and muon detectors. It completely encloses the interaction point, except for small openings for the entering and exiting beams, and is designed to operate at the standard SSC luminosity of $10^{33}\mathrm{cm}^{-2}\mathrm{s}^{-1}$. The momenta of charged particles are measured with tracking devices placed inside the solenoidal magnetic field, and the energies of hadrons, photons, and electrons are determined with the surrounding calorimeter. Muon momenta are also measured with an external set of magnets and chambers. The powerful tracking system at the center of the detector yields a complete view of the event structure in the central region, including the observation of secondary vertices from the decay of long-lived particles. The capability to make redundant measurements of electron, muon, and hadron energies, the ability to determine the signs of charges, and the availability of detailed event information will be essential for understanding new phenomena at the SSC.

The general, exploratory nature of our proposed research program can be expressed in the form of specific questions:

(*a*) What is the mechanism for electroweak symmetry breaking, the process by which particles obtain mass?

(*b*) What are the properties of the t (top) quark?

(*c*) Are there additional heavy bosons to indicate the presence of new, as yet undiscovered forces?

(*d*) Are leptons and quarks elementary or are they composed of more fundamental particles?

(*e*) Do particles exhibit a larger symmetry pattern such as supersymmetry?

The first two questions arise from the present direction of particle physics research and are of great current interest. Models of electroweak symmetry generally postulate the existence of one or more new particles such as the Higgs boson. If the Higgs boson exists it will be produced at the SSC, as will the top quark, and their detection is given high priority in our proposal. Questions (*c*), (*d*), and (*e*) are more general but also more speculative. They illustrate the exploratory nature of experimentation in a new energy

regime and help guide the design of our proposed detector. Before discussing these five topics in greater detail, we emphasize that we intend to pursue a very general study of proton-proton interactions at the SSC that is not limited to any particular example of possible new physics.

2.2. Electroweak symmetry breaking

One of the central aims of the SSC physics program is the exploration of the mechanism that generates particle masses. In the simplest form of the Standard Model, the masses of the W boson, the Z boson, and the charged fermions result from their interaction with a fundamental scalar field whose vacuum expectation value is not zero. The dynamical component of this scalar field, the Higgs boson, is expected to decay predominantly into W^+W^- and ZZ pairs if its mass exceeds 180 GeV. The expected cross section for producing Higgs bosons at the SSC is shown in Fig. 2 and depends on the unknown Higgs and t quark masses. In other theories, such as technicolor, the fundamental scalar Higgs field is replaced with a condensate of new, strongly interacting fermions that gives mass to the W and Z. In such theories new particle states are expected which decay to ZZ, WW, WZ or γZ pairs. A study of the production of such boson pairs is therefore a promising avenue for investigating electroweak symmetry breaking.

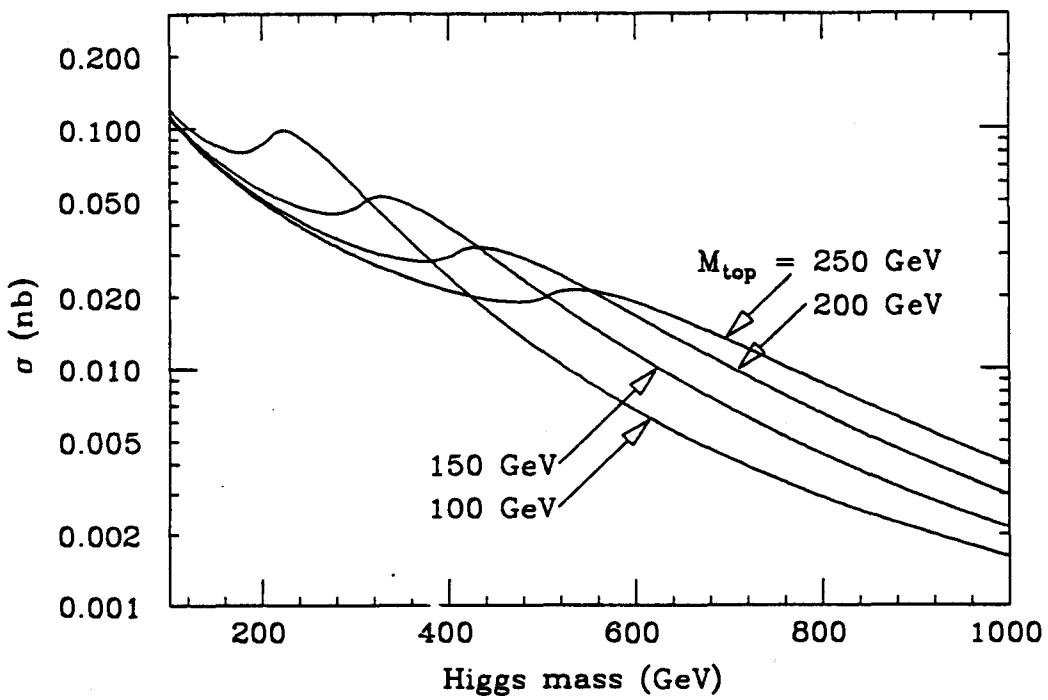

FIG. 2. Cross section for Higgs production at $\sqrt{s} = 40$ TeV as a function of the Higgs and t-quark masses.

The cleanest and perhaps most straight-forward way of observing a Higgs signal at the SSC is in ZZ pairs that decay to four-lepton final states containing electrons and muons. The branching ratio for this Higgs decay is about 1.1×10^{-3}. The corresponding yield of

Higgs bosons with a mass of 300 GeV is of order 500 per standard SSC year (defined as an integrated luminosity of $10^{40}\,\mathrm{cm}^{-2}$) and decreases to about 20 events at 1000 GeV.

For masses below the Z pair threshold, the detection of the Higgs boson becomes difficult. The most promising channel appears to be ZZ^* (where Z^* denotes a virtual Z) with decay to a final state of four charged leptons. The branching ratio to ZZ^* falls rapidly with decreasing Higgs mass, effectively limiting the search to the mass region above 140 GeV.

If no Higgs boson is observed below 1 TeV, strong-interaction effects (from technicolor or other forces) are expected in the scattering of longitudinally polarized W and Z bosons at high energy. In this case, resonances may occur in the 1–2 TeV mass region in ZZ, W^+W^-, WZ, and γZ channels. Nonresonant, strong-scattering effects are also possible in these channels, as well as in W^+W^+ and W^-W^-. Expected event rates for these high-mass processes in the purely leptonic decay modes containing electrons and muons are small, at the level of 10 to 20 events per year for ZZ and WZ, and perhaps 50 for like-sign WW pairs.

A sensitive investigation of electroweak symmetry-breaking effects in ZZ, WZ, and WW scattering requires the efficient detection of electrons and muons at angles to within about 5° to 10° of the beams ($|\eta| = 2.5$–3.0) with a detector that can operate at the SSC design luminosity of $10^{33}\mathrm{cm}^{-2}\mathrm{s}^{-1}$. Detailed studies of the Higgs boson or the discovery of strong interaction effects will require a capability to operate at even higher luminosities, which should eventually be achieved at the SSC. Electrons and muons must be measured with sufficiently good resolutions to distinguish real Z bosons from possible dilepton backgrounds. In addition, hadronic calorimetry will be essential for the rejection of backgrounds from semileptonic decays of heavy quarks by allowing the implementation of lepton isolation criteria. By extending such calorimetry to within about one degree of the beams ($|\eta| = 5$), high-mass Z pairs can also be identified by missing transverse-momentum techniques when one Z decays to neutrinos and the other Z decays to electron or muon pairs. Sensitivity to these additional decay modes will help extend the mass reach of Higgs searches.

The measurement of ZZ, WZ, and WW pairs is given high scientific priority in our Expression of Interest since it represents one sure way of probing the boundaries of physics as codified in the Standard Model. The SSC will begin to yield clues about the origin of mass and thereby open a qualitatively new era in particle physics. Our proposed detector, with its central magnetic field, provides redundant measurements of electron and muon energies, and a determination of lepton charges. These capabilities may be essential in the detection of processes which occur at the level of 10^{-13} of all p-p interactions.

2.3. THE t QUARK

The t quark has not yet been found despite careful searches at PEP, PETRA, TRISTAN, SLC, LEP, and at the CERN and Fermilab hadron colliders. The result of these searches constrains the t-quark mass to be higher than 89 GeV[1]. An indirect upper limit of about 250 GeV is obtained from bounds on the self-energy contributions to the known W and Z masses from loops containing the t quark[2]. Detection of the t quark and a measurement of its mass will yield one more, perhaps critical, clue to the general puzzle of the fermion mass spectrum.

The expected cross section for t-quark pair production at the SSC is very large, with the yield of t quarks exceeding 10 million per standard SSC year. This will provide a unique opportunity for precision measurements of t-quark properties. Another important consequence is that the rate of W^+W^- pairs from t-quark decays will dominate all other sources by one or two orders of magnitude since the t-quark mass is above the W-b threshold. The search for the Higgs boson in the W^+W^- channel will therefore encounter severe backgrounds. The leptons from t-quark semileptonic decays may also generate formidable backgrounds in other particle searches. Measurements of t-quark production at the SSC are therefore not only interesting for determining t-quark properties, but they are also essential for estimating the backgrounds to other possible physical processes.

Events with t quarks will be identified by searching for one or two isolated leptons (electrons or muons) resulting from semileptonic decays. The spectrum of lepton pairs from the decay of either single t quarks or t pairs will be sensitive to the top mass. The mass may be determined from events in which one t decays semileptonically to provide identification and the other one decays to three reconstructible jets, two of which must be compatible with W decay. Identification of the b-quark jets in such events is essential for reducing backgrounds from W-multijet production.

The proposed detector capabilities for measurements of electrons and muons (including signs of charges), as well as of hadron jets and missing transverse momentum are well-matched to these studies. Vertex detection provides additional information through identification of b jets and the separation of prompt leptons from b decay products. Operation at a luminosity well below the SSC design value is sufficient for initial t-quark studies because of the large production cross section.

2.4. NEW, HEAVY BOSONS

The Higgs boson and the t quark are the only undiscovered components of our standard picture of particle physics. The remarkable consistency between measurements and Standard Model predictions gives little or no clue about the physics that may lie at higher mass scales. Nevertheless, it is almost certain that additional physical processes must exist. For example, the three-fold replication of fermion families is not at all understood and points towards a more extended dynamical framework. Similarly, the handedness of the weak interactions leads to speculations about the existence of additional interactions between right-handed fermions at higher energies. It is natural to assume that new,

as yet undiscovered forces may manifest themselves in the form of massive bosons similar to the W and Z. Detection of heavy, charged bosons will be based on searches for events with energetic, isolated leptons and a large imbalance in the observed transverse momenta. The SSC will be sensitive to such new bosons with masses up to about 8 TeV. The search for heavy, neutral bosons decaying to lepton pairs will be most easily carried out with electron detectors, since the energy resolution $\delta E/E$ of electromagnetic calorimeters improves or remains constant with increasing energy, whereas the resolution of muon momenta worsens. Nonetheless, an observation in the muonic channel, even with modest resolution, will provide a test of e-μ universality.

2.5. Quark and Lepton Substructure

The existence of numerous, seemingly "fundamental" particles leads to the speculation that a deeper layer of matter may exist and that the particles we observe are composite systems of yet other, more basic entities. If quarks consist of other particles bound by some new, strong force, then at sufficiently high energies the scattering of quarks will exhibit deviations from the expectations based on QCD. An unexpected excess of hadronic jet events at high transverse momenta would be an indication of quark compositeness. The most important detector requirement is a hadron calorimeter whose response is well understood up to energies of about 7 TeV.

Lepton substructure can also be probed at the SSC by measuring the lepton pair spectrum in the mass region above 1 TeV. Deviations from the expected Drell-Yan contribution would be a signal for possible lepton substructure. The experimental requirements for observing such substructure are similar to those for the search for new, heavy bosons.

2.6. Supersymmetry

Supersymmetry is an elegant concept that postulates a relationship between fermions and bosons and predicts a rich spectrum of new particles. One example is the gluino, the supersymmetric partner of the gluon. This particle would be produced copiously at the SSC if its mass lies below 2 TeV. The decay chain of the gluino ends in at least one stable, presumably neutral particle which is unobservable. The resulting imbalance in the observed transverse momentum is one of several typical signatures of the production of supersymmetric particles. The main experimental requirement is a hadronic calorimeter, free of significant dead regions, which covers the full solid angle down to within about 1° of the beams ($|\eta| = 5$). Here also, the redundancy coming from the combination of tracking and calorimetry should help make more credible the observation of new phenomena. Charge determination will be essential for identifying gluino decays that are signalled by like-sign dileptons.

The five examples given above do not represent a complete summary of what motivates our interest in the SSC physics program; our proposed study of proton-proton interactions will be sensitive to a wide variety of processes. These examples are, however, sufficient to illustrate the requirements for a detector design as discussed in the next section.

3. Detector overview

3.1. General detector requirements

A detector for pursuing the physics goals discussed above must be able to:

(*a*) Identify and measure electrons, muons, and hadron jets with good efficiency and resolution at all angles greater than about 10 degrees with respect to the beams (corresponding to the pseudorapidity interval $-2.5 < \eta < 2.5$).

(*b*) Determine the charges of leptons.

(*c*) Extend the detection of hadron jets to within about 1° of the beams ($|\eta| = 5$) for measurements of missing transverse momenta.

(*d*) Find the vertices of primary interactions and of secondary decays.

(*e*) Operate at the SSC design luminosity of $10^{33}\mathrm{cm}^{-2}\mathrm{s}^{-1}$, with a potential for accommodating eventual luminosity upgrades.

The detection of electrons and muons is essential to much of our proposed physics program and is given high priority in the design of the detector. Hadron calorimetry is required not only for measuring jet production but also for improved electron identification and for a general understanding of the sources of observed leptons. The ability to measure the signs of charges is important for some physics topics and background studies. Tracking systems that provide good vertex measurements will help resolve multiple primary interactions that are produced inevitably at high luminosity, and they also help tag the production of c and b quarks and of τ leptons. The ability to operate at high luminosity is essential for investigating rare phenomena such as the production of gauge boson pairs with large effective masses.

The inspiration for proposing a general-purpose detector which meets the above requirements is provided by the great success of existing, large detectors at electron-positron and proton-antiproton colliders. Many of the possible physics signals of interest at the SSC produce leptons and hadron jets at large angles and with large transverse momenta. It is thus natural to consider a detector which combines a large solenoidal magnet for determining the momenta of charged particles with a hermetic calorimeter to measure jet and electron energies and missing transverse energy. The measurement of momenta with a magnetic field has the outstanding advantage of providing an absolute, stable energy scale, something not easily achieved with calorimetric techniques. Moreover, the signs of charged particles can be determined, a capability that is essential for a number of physics topics such as charge asymmetries and like-sign dilepton production. A solenoid field configuration provides azimuthal symmetry and simplifies detector construction and event analysis. The detector we envision consists therefore of a solenoidal spectrometer, surrounded by electromagnetic shower counters, hadronic calorimeters, and systems for detecting muons.

3.2. Detailed reasons for a solenoid

A sophisticated tracking system immersed in a solenoid magnetic field will provide the following capabilities:

(*a*) Detection of individual, charged particles and precise measurements of their momenta.

(*b*) Determination of charge sign, essential for asymmetry measurements, identification of like-sign WW pairs, and rejection of certain backgrounds.

(*c*) Ability to impose triggers with variable transverse momentum thresholds via track stiffness criteria.

(*d*) Improved electron identification by comparison of track momentum with calorimeter energy measurement.

(*e*) Full visualization of the charged-particle content and momentum flow in the central pseudo-rapidity region.

(*f*) Measurements of jet fragmentation.

(*g*) Identification of secondary decays and reconstruction of long-lived particles such as K^0, D, and B mesons.

(*h*) Cross-check and calibration of calorimeter response.

(*i*) Identification and removal of photon conversion backgrounds.

(*j*) Improved capability to reconstruct narrow dilepton resonances such as the J/ψ, Υ, and Z.

(*k*) Redundant measurements of electron and muon energies within the overall detector scheme.

This list indicates the great analyzing power of a solenoidal magnetic spectrometer. When combined with external calorimeter and muon systems, this spectrometer becomes an extremely flexible and powerful tool for the study of proton-proton collisions. The resulting general-purpose detector, unlike more specialized devices, will allow multi-faceted studies of any given process as outlined in Section 2 and described in Section 5.

3.3. Determination of detector configuration and scale

The scale and layout of the design, shown in Fig. 1, emerges naturally from very general considerations. The solenoid coil is placed inside the calorimeter to keep magnet dimensions to a manageable size. Engineering considerations set an upper limit of about 2 tesla on the field that can be generated with a coil sufficiently thin to avoid significant degradation of calorimetric energy measurements. It then follows that a minimum interior coil radius of 1.8–1.9 m is required to assure a momentum resolution of $\delta p_t/p_t = 0.20 p_t$ (TeV/c). This level of resolution is desirable for the identification of lepton pairs as Z's and is adequate for other physical processes of interest. One exception is the production

of narrow dilepton resonances in the multi-TeV region. For the precise measurement of the mass of such particles, we rely on calorimetric measurements of electron energies.

A solenoid geometry is highly effective for measuring the momenta of particles produced in the central 90% of the full solid angle, corresponding to the pseudorapidity range $-1.5 < \eta < 1.5$. A tracking system extending to a radius of 1.8–1.9 m is required to have a total length of 8–9 m to assure uniformly good momentum resolution over this central region. The proposed tracking volume and tracking technologies also permit the measurement of momenta of charged particles at intermediate angles, in the range $1.5 < |\eta| < 2.5$, albeit with reduced resolution.

The scale of the remainder of the detector is set by the demands of calorimetry and muon detection. Calorimeter depths of 9–11 interaction lengths near 90 °and somewhat more for the forward direction are adequate for shower containment. The calorimeter system is surrounded by a set of detectors and magnets designed to identify and measure muons. At intermediate angles ($1.5 < |\eta| < 2.5$), we are considering the installation of superconducting, air-core, toroidal magnets to achieve a muon transverse momentum resolution similar to that obtained in the central region. At larger angles, the calorimeter is surrounded by a magnetized iron toroid that provides a trigger for high-p_t muons and a second measurement of muon momenta for better background rejection. The external muon system allows the identification of muons even when accompanied by complex hadronic jet activity.

The performance goals for this detector, summarized in Table 1, are the result of an overall judgment that takes into account both scientific goals and technical feasibility. The conceptual design of the detector is clear, but we have not yet made final decisions on the exact configuration or technology of the various components. Such decisions will be made on the basis of ongoing detector R&D efforts and detailed optimization studies.

3.4. Critical detector issues

The construction of the large detector outlined above represents a major engineering challenge. For example, the precise alignment of hundreds of thousands of tracking elements distributed throughout the huge detector volume is a daunting task. The detector design must also take into account the SSC environment which imposes rates and radiation levels far higher than those encountered in previous collider physics experiments.

With respect to rates, the most vulnerable part of our proposed detector is the central tracking system since it must detect individual particles while being exposed to the entire flux of secondary particles produced in the central region. As described below, we are confident that a combination of silicon devices at small radii and proportional wire tubes or scintillating fibers at larger radii represents technologies that will be able to track particles at luminosities up to the SSC design value of $10^{33}\,\mathrm{cm}^{-2}\mathrm{s}^{-1}$. We believe that at higher luminosities tracking layers at the outer radii of the tracker can survive and provide useful data.

Table 1

Detector description and design goals.

	Central $\lvert\eta\rvert \lesssim 1.5$	Intermediate $1.5 \lesssim \lvert\eta\rvert \lesssim 3.0$	Forward $3.0 \lesssim \lvert\eta\rvert$
Inner tracking:			
Magnetic field	2.0 T	2.0 T	No
Radius	1.85 m	1.85 m	
Combined $\delta p_t/p_t^2$ at 1 TeV/c	0.2 (TeV/c)$^{-1}$	1.0 (TeV/c)$^{-1}$ [a]	
Calorimeter:			
Inner radius or z	2.2 m	4.7 m	17 m[b]
Depth	$\gtrsim 9\lambda$	$\gtrsim 11\lambda$	$\gtrsim 14\lambda$
Segmentation (Had)	0.05–0.10[c]	0.05–0.10[c]	10 cm × 10 cm
Resolution (Had) $\delta E/E$	$< 0.7/\sqrt{E} \oplus 0.04$[d,e]	$< 0.7/\sqrt{E} \oplus 0.04$	$< 1.0/\sqrt{E} \oplus 0.05$
Resolution (EM) $\delta E/E$	$< 0.25/\sqrt{E} \oplus 0.02$	$< 0.25/\sqrt{E} \oplus 0.02$	
Electron ID	Yes	Yes	None
Muon system:			
Total absorber	$\geq 14\lambda$	$\geq 14\lambda$	—
Combined $\delta p_t/p_t^2$ at 1 TeV/c (with central tracker and toroids)	$\lesssim 0.18$(TeV/c)$^{-1}$	$\lesssim 0.25$(TeV/c)$^{-1}$ [a]	—

[a] At $\lvert\eta\rvert = 2.5$.
[b] For version shown in Fig. 3.
[c] $\Delta\eta = \Delta\phi$.
[d] E is in GeV unless otherwise specified.
[e] Here and elsewhere, $\oplus$ indicates addition in quadrature.

Radiation levels at the SSC from the proton-proton interactions are sufficiently high at small angles or at small distances from the beams that special precautions must be taken to avoid radiation damage to detector components in these areas. Silicon vertex detectors placed 10 cm from the beams will experience exposures of about 0.4 Mrad and 10^{12} neutrons cm^{-2} during a standard SSC year. Radiation-hardened devices can be expected to survive such exposures for the expected lifetime of the experiment. Another area of concern is electromagnetic calorimetry at small angles. At $\lvert\eta\rvert = 3$, for example, we expect doses of several Mrad per standard SSC year. This requires care in the choice of calorimeter materials and placement of electronic readout components in this region. Fortunately, radiation levels are much less severe at larger angles, and we are confident that suitable calorimeters can be constructed.

Another area of concern, related to the SSC rate problem, is the design of trigger schemes that will identify the events of interest amid the intense stream of inelastic proton-proton collisions. The physics examples described in the previous section have rather unique event signatures with relatively low rates of background processes. Nevertheless, care must be exercised to design triggers that will tag events from unexpected physics

sources without being swamped by uninteresting events. A further discussion of this point is found in Section 4.6.

3.5. Detector description

In Fig. 1 we present a design example (shown in cross-section in Fig. 3) that meets the physics goals described above, and at the same time begins to deal with the engineering realities of a 4π magnetic spectrometer. The solenoid magnet coil is inside the calorimeter to keep the dimensions of the coil manageable. The coil can be made sufficiently thin that calorimeter performance and electron identification are not degraded.

The detector of Fig. 1 is based on a solenoidal magnet design which we label "Type-S". This coil does not have a conventional iron return yoke or iron near the ends of the coil, and represents an extrapolation of that used in the ZEUS detector. We discuss the details of this design in the following section and later in this report. We are also considering two alternatives, in which the magnetic field is returned either (a) by adding iron to the calorimeter ("Type-I"), or (b) via an explicit iron return yoke ("Type-L") . These variants are shown in Figs. 4 and 5. Detector configurations for these two additional cases are discussed below and the properties of the coils in all three configurations are reviewed in section 4.2.

Before proceeding it is useful to define the detector coordinate system. The x axis points radially outward in the plane of the ring, y is upward, and z points along the beam bisector to complete a right-handed coordinate system. Spherical polar (r, θ, ϕ) and cylindrical (r, ϕ, z) coordinate systems are obtained from the Cartesian system in the usual way.

3.5.1. Detector based on the Type-S solenoid

In the detector shown in Figs. 1 and 3, about 60% of the magnetic flux is returned through the volume of a non-magnetic calorimeter. The remaining flux is returned in a layer of steel about 30 cm thick on the outside of the calorimeter, approximately 2.5 m from the coil, in order to create a field-free region outside the calorimeter for electronics and/or photomultiplier tubes. The absence of a return yoke minimizes the external decentering forces between the coil and other magnetic elements, and hence the size of coil and cryostat supports are dominated by gravitational rather than electromagnetic forces. At 90° the total calorimeter thickness is 9 interaction lengths, and with the inclusion of muon iron toroids there are more than 14 interaction lengths between the interaction point and the outer layers of muon chambers. This is sufficient to insure that hadronic cascades are completely absorbed and that only muons exit from the back of the detector.

In both the Type-S and Type-I coil designs, the endcap calorimeter can be retracted about 1 meter to permit personnel access to the central tracking volume. For installation of major components in the tracking volume, the endcap calorimeters must be fully retracted. Penetrations for the coil cryogenic services, central tracking cables, cooling, low voltage power, calibration and timing signals are also brought into the tracking volume at this

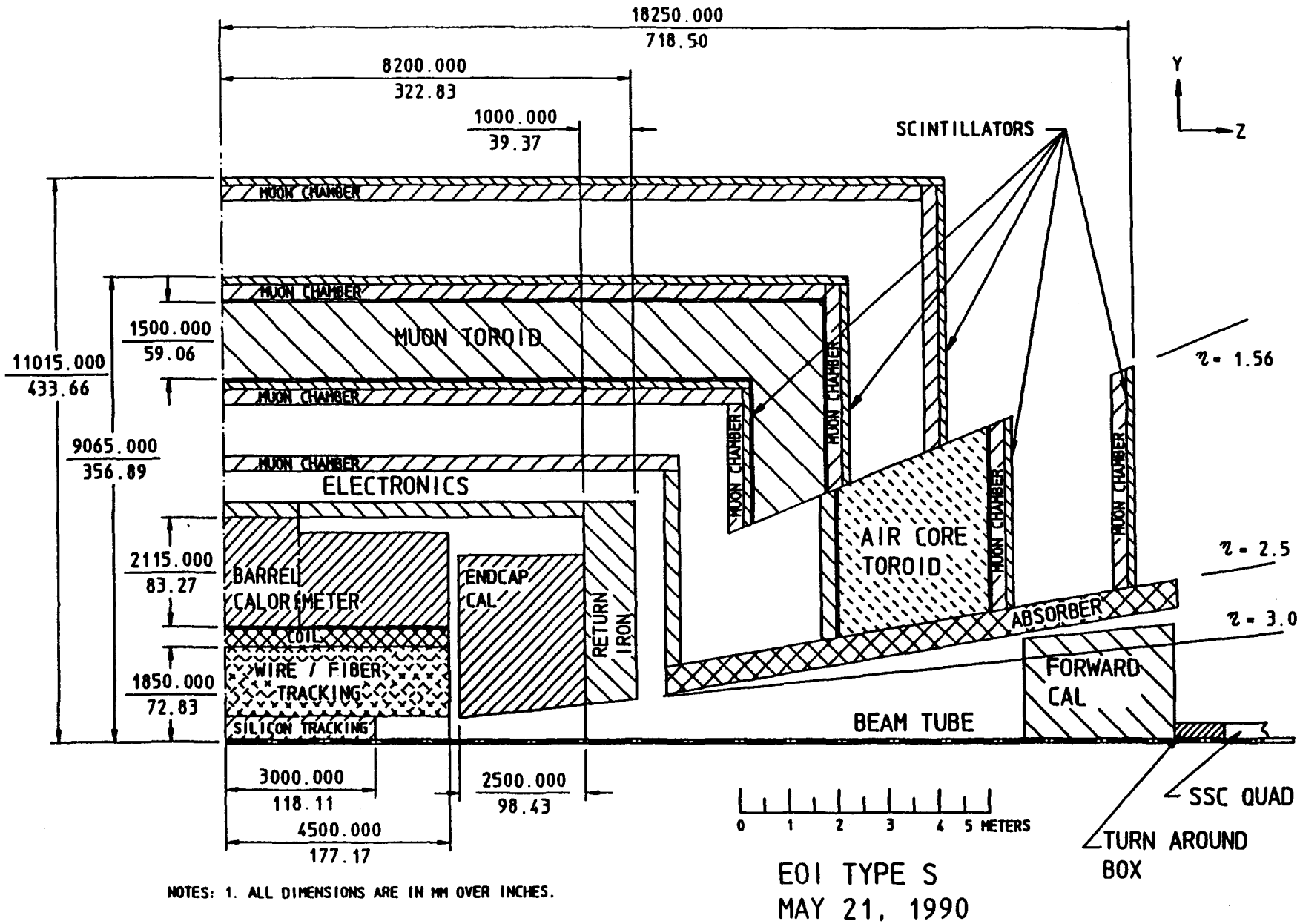

FIG. 3. Quadrant plan view of the detector with the short, or Type-S solenoid, also shown in Fig. 1. In this version we have shown air-core toroids for muon momentum analysis at intermediate angles.

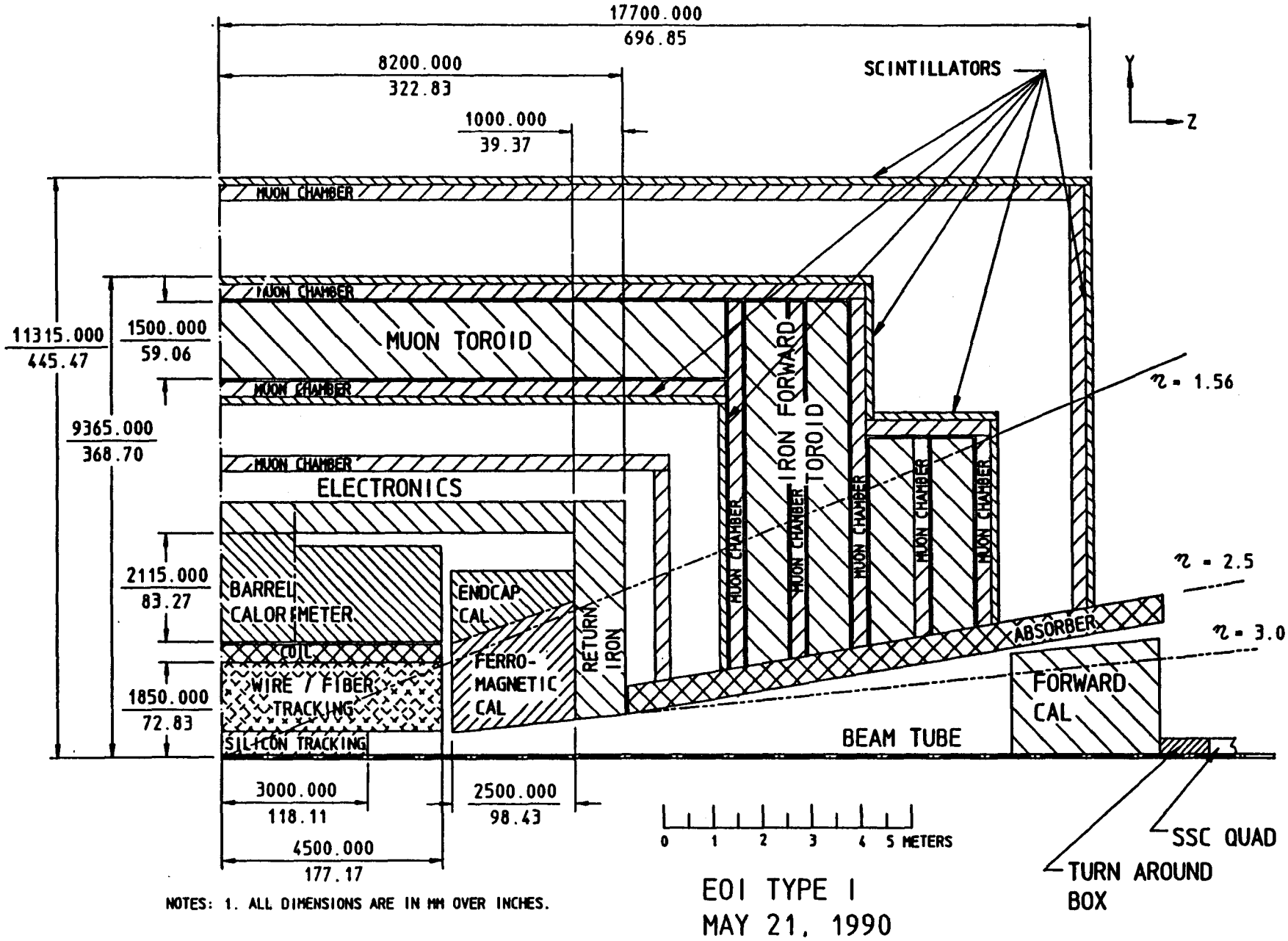

FIG. 4. Quadrant plan view of the short-coil solenoidal detector with iron-laced endcap calorimeters (Type-I). This drawing also shows an iron toroid for the intermediate-angle muon system, an alternative to the air-core toroids shown in Figs. 3 and 5.

The calorimeter thickness is chosen to contain almost all of a high-energy shower, but at least 14 interactions lengths are needed to limit hadron punch-through to the degree necessary for muon detection. Iron is the most cost-effective material for the additional absorber, and the muon iron toroids are the most massive part of the detector. The iron is magnetized in the azimuthal direction for muon momentum analysis. Four stations of muon chambers, two inside the iron toroids and two outside, are used to measure muon trajectories. The spacing between the measuring stations is chosen to obtain sufficient angular resolution for muon charge determination up to a transverse momentum of 1 TeV/c, using standard drift chamber technology. The annular space inside the muon toroids can used for personnel access to the calorimeter and muon chamber electronics without moving heavy components. This space is also used as an air duct for cooling that part of the electronics inside the muon steel which cannot be directly liquid-cooled. A fast muon trigger is obtained from three layers of scintillation counters; these crudely measure the bend angle in the toroids.

Given the azimuthal symmetry of the solenoid and return yoke, high momentum muons will exit the calorimeter and solenoid return yoke along radial trajectories except for a multiple-scattering contribution. Hence, the first muon measuring station just outside the calorimeter includes chambers that measure the particle trajectories in both the r-ϕ and r-z planes with high precision.

The design of the detector in the forward region between $3 < |\eta| < 5$ poses several problems, since there are conflicts between different detector and accelerator subsystems which are compounded by the radiation environment of the SSC. In Fig. 3 we show one possible configuration for the intermediate-angle and forward systems, with air-core toroids for muon measurement and a simple forward calorimeter. The design in this region must deal with the following problems and practical requirements:

(a) The calorimeter covering $3 < |\eta| < 5$ must be sufficiently far removed from the interaction region that the finite size of hadronic showers will not degrade the missing transverse energy ($\not{E}_t$) resolution of the detector.

(b) The calorimeter must withstand extremely high radiation levels.

(c) The presence of the forward calorimeter should not substantially increase the radiation dose in the central tracking chambers or the central calorimeter resulting from albedo particles.

(d) Back-scattering from the forward calorimeter must not affect the ability to make cuts on the ratio of electromagnetic to hadronic energy in the endcap calorimeter.

(e) Division of the calorimetry into "endcap" and "forward" sections should not degrade the $\not{E}_t$ resolution of the detector.

(f) The muon chambers must be protected from particles scattered from the calorimeter and quadrupoles, as well as low-energy neutrons and photons in the hall.

(g) Sufficient space must be available to provide access routes to the central detector for maintenance and assembly.

(*h*) Access and maintenance plans must take into account the radioactivation of all forward components.

(*i*) Sufficient space must be left for servicing, alignment and operation of the accelerator components. Energizing of the forward muon toroids should not, for example, affect accelerator operation[4].

Items (*a*) through (*d*) in this list argue for moving the forward calorimeter far from the interaction point. However, we are concerned that the presence of a calorimeter downstream of air-core toroids will subject the muon chambers near the air-core toroids to an overwhelming flux of low-energy particles, from the high-$|\eta|$ edge of the central calorimeter, the front face of the forward calorimeter, and possibly the front face of the accelerator quadrupole and its associated collimator. On the other hand, if the endcap calorimeter is extended to nearly $|\eta| = 5$ (*i.e.* eliminate the forward calorimeter), the angular resolution may be unacceptable, the radiation dose on the endcap calorimeter may be intolerable, and albedo neutrons from this region may "fill" the central cavity to an excessive degree.

Alternatively, iron muon toroids could be used in the intermediate-angle region, as shown in Fig. 4. This protects all but the outermost of the muon chambers from albedo, but the momentum resolution of the system is degraded. No firm decision about the exact configuration of the forward calorimeter and muon systems has yet been made. The definition of the detector in this region will be among our highest priorities in the coming year.

3.5.2. Short coil with an iron calorimeter: Type-I

As discussed in section 4.2, the radial field components inherent in the short-coil design lead to large compressive stresses on the conductor, and substantial engineering challenges. We therefore consider it prudent to investigate alternative coil designs. The short-coil design shown in Fig. 4 with an iron calorimeter is similar in cross-section to the Type-S coil, and differs from it only by having a ferromagnetic endcap. Only a minimum amount of iron has been added to the calorimeter. It is possible to build the entire calorimeter out of iron, but more material would still have to be added to suppress the muon flux both in the barrel and endcap regions. Hence, for this example we have retained an explicit return yoke.

The iron in the endcap makes the field in the tracking volume more uniform. Because the superconducting coil is now close to magnetized iron, the coil structure must withstand larger decentering forces. The use of steel in the endcaps may limit the maximum axial field in the tracking volume to about 1.7 T. The endcap calorimeter must also now sustain an electromagnetic force of the same magnitude as the gravitational force. A detailed risk/benefit analysis is needed to weigh the various tradeoffs.

3.5.3. Long coil: Type-L

The Type-L design represents the most conservative approach, and is based on the success of such coils in many existing detectors. A quadrant plan view is shown in Fig. 5.

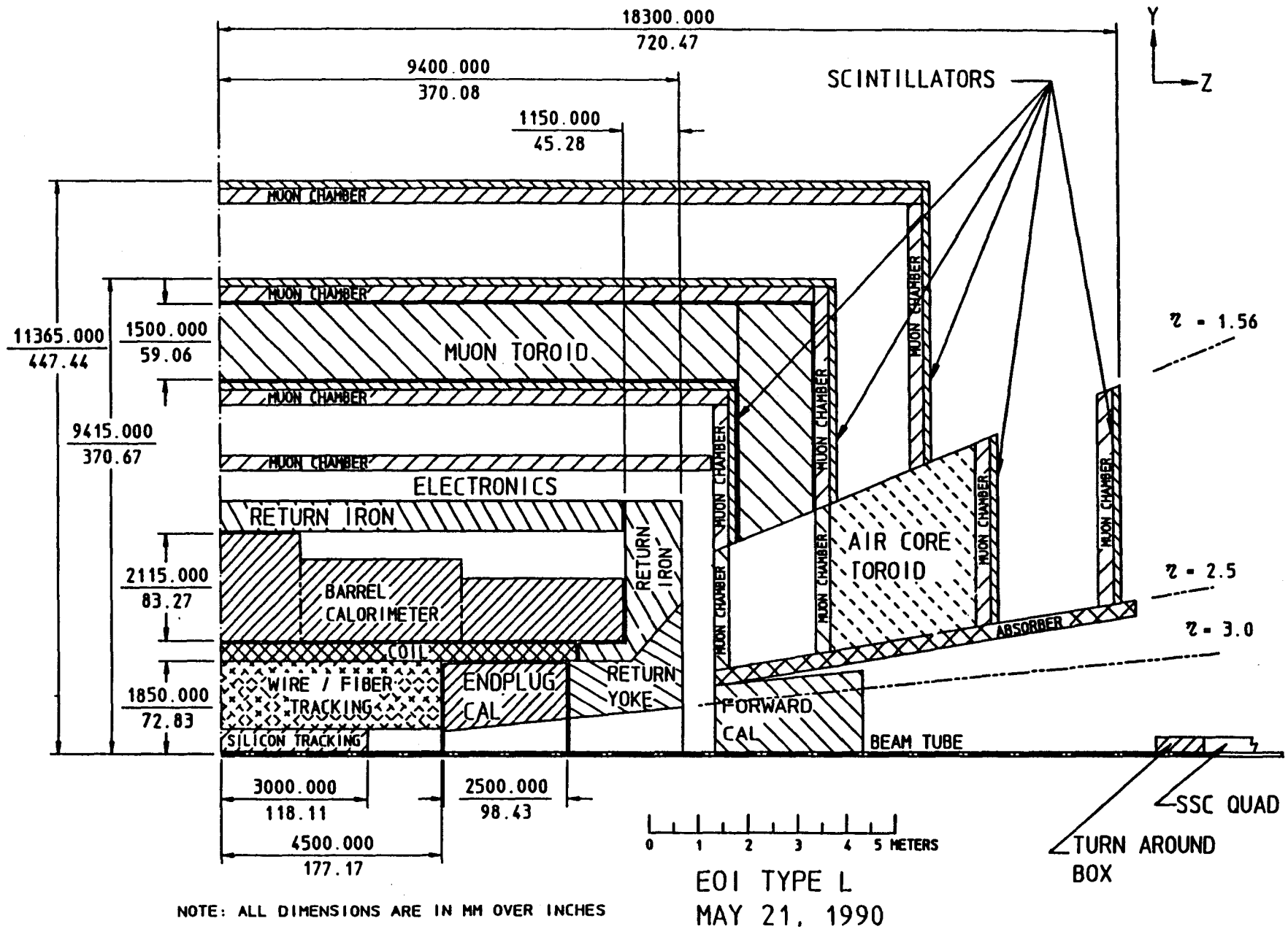

FIG. 5. Quadrant plan view of long-coil, or Type-L, solenoidal detector with explicit iron flux return.

interface. Because this interface is non-projective it has minimal impact on the hermeticity of the calorimeter.

The tracking system inside the coil is divided into three sections—a vertex tracking system, a large-radius barrel tracking system, and an intermediate tracking system covering the endcap. Closest to the beam line is an extensive (33 m^2) silicon tracking system covering the pseudorapidity interval $-2.5 < \eta < 2.5$. This detector incorporates two or three layers of pixel detectors next to the beam line in conjunction with several superlayers of conventional silicon strip detectors inside a cylindrical volume 1 m in diameter and 6 m long. Outside the silicon system is the large-radius tracking volume. The technology for the barrel and intermediate tracking systems has not been chosen, but the performance goals of the system have been defined in the previous section. It is probable that the large-radius tracking system will employ either wire and/or fiber tracking technologies.

Since there is no iron near the end of the coil, the magnetic field has a substantial radial component near the ends of the tracking region. A concern is the effect of the non-uniform magnetic field on the trigger from the tracking system for high p_t particles. Trigger studies for the tracking system in a non-uniform magnetic field are being made. Initial results indicate that the non-uniform field does not present a problem for pattern recognition in the silicon tracking system over its full acceptance. Studies of pattern recognition in the larger-radius wire or fiber tracking systems in the barrel and intermediate regions are also encouraging[3].

A secondary concern is the degraded momentum resolution of the Type-S solenoid for $|\eta| > 1.5$. In this region the path length in the magnetic field is already reduced . Because the Type-S solenoid lacks a conventional return yoke, the useful magnetic field perpendicular to the trajectories of high momentum particles is further reduced in the intermediate regions by about 20% if the coil is wound with a uniform current density. A more uniform axial field component can be achieved by changing the current density in the coil as a function of z, as, for example, is done in the ZEUS magnet. At present this is the primary engineering research direction for the Type-S solenoid. To improve the momentum resolution for muons at intermediate angles, which are not well-measured in a solenoidal field, we are considering the use of air-core toroids between $|\eta| = 1.5$ and $|\eta| = 2.5$.

The central calorimeter system consists of a barrel calorimeter closed by two endcap calorimeters. The calorimeter does not penetrate the volume outlined by the coil cryostat, as contrasted with an "endplug" or Type-L design where the calorimeter in the pseudorapidity interval $1.6 < |\eta| < 3$ is inside the volume of the coil (see Fig. 5). In these examples, the calorimeter thickness grows to 11 interaction lengths in the endcap region. Calorimeters for all solenoid options share the goals given in Table 1: The calorimeter is a hermetic, fine-grained device with projective towers, covering the range $-5 < \eta < 5$ and having excellent electron identification capabilities in the cental region ($|\eta| < 2.5$). Outside the calorimeter and the return yoke about 60 cm are allowed (radially and in the axial direction) for electronics and mechanical structures.

This coil has a conventional iron return yoke, and thereby reduced compressive forces on the superconductor. It can be engineered to have a uniform magnetic field over the tracking volume. The major disadvantages are the complete penetration of the calorimeter volume by the cryostat, the difficult geometry of the endplug calorimeters, and the long endplug "stroke" necessary for access to the tracking volume. Simulation work is in progress to assess the impact of the dead coil material on calorimeter performance.

3.6. Radiation environment

The radiation environment in SSC detectors was addressed by an SSC task force in late 1987[5, 6]. While more detailed studies will eventually be necessary for any given detector, the main results scale with angle and dimensions in a simple way that can be applied directly to the SDC detector. Several topics, such as radioactivation in the forward direction, were not addressed and remain important design issues.

The central tracker is mainly sensitive to a direct particle flux which is a function only of the perpendicular distance to the beam line. Particles "looping" in the magnetic field make multiple passes through the tracker, approximately doubling the dose rate reported in Ref. 5. An albedo flux of charged particles and photons from large-η parts of the detector contributes additional minor increases to the dose rate. If there are not "holes" in the central detector for $|\eta| \gtrsim 3$, albedo contributions will be substantial.

The tracking volume is also filled with a "gas" of neutrons that arise from hadronic cascades in the calorimeter, again mostly from the small-angle regions. The neutron spectrum in this or any other SSC situation can be roughly described by a log-gaussian distribution peaking at just under 1 MeV, as would be expected from nuclear boiloff following excitation. In most situations there is an equal flux of thermal neutrons, which do not seem to present any problem for the detector except for activation of the forward calorimeters. The neutron flux scales with the inverse square of characteristic dimensions of the volume inside the calorimeter, and is dependent upon the material used in the calorimeter. The dimensional scaling results in a reduction to 0.34 of the flux obtained in Ref. 5 for a sphere with a 2 m radius. The scaling with material is less certain. The SSC study normalized its results to a uranium/scintillator calorimeter; with our favored technologies (lead plus either liquid argon or a hydrogenous material) a further reduction by about 0.60 is expected. The result is an average fluence of 0.5×10^{12} cm^{-2} in one year at the design luminosity, with the calorimeter extending down to $|\eta| = 3$. Flux near the ends will be perhaps four times greater than at the center.

The neutron flux in the central volume will be substantially greater if the forward calorimetry is moved closer or, equivalently, if the minimum angle of the central detector is further decreased[7]. For example, if the pseudorapidity coverage of the central detector is extended from $|\eta| = 3$ to $|\eta| = 5$, the average flux inside the volume will increase by a factor of three. On the other hand, it can be reduced by the introduction of a hydrogenous "liner" inside the calorimeter; such a liner is especially effective in the large-$|\eta|$ regions[8]. The importance of the neutron flux in the tracking volume cannot be overestimated,

since it is the primary source of radiation damage to the silicon. The decision process in choosing the geometry and materials for the calorimeters will have to take account of this problem.

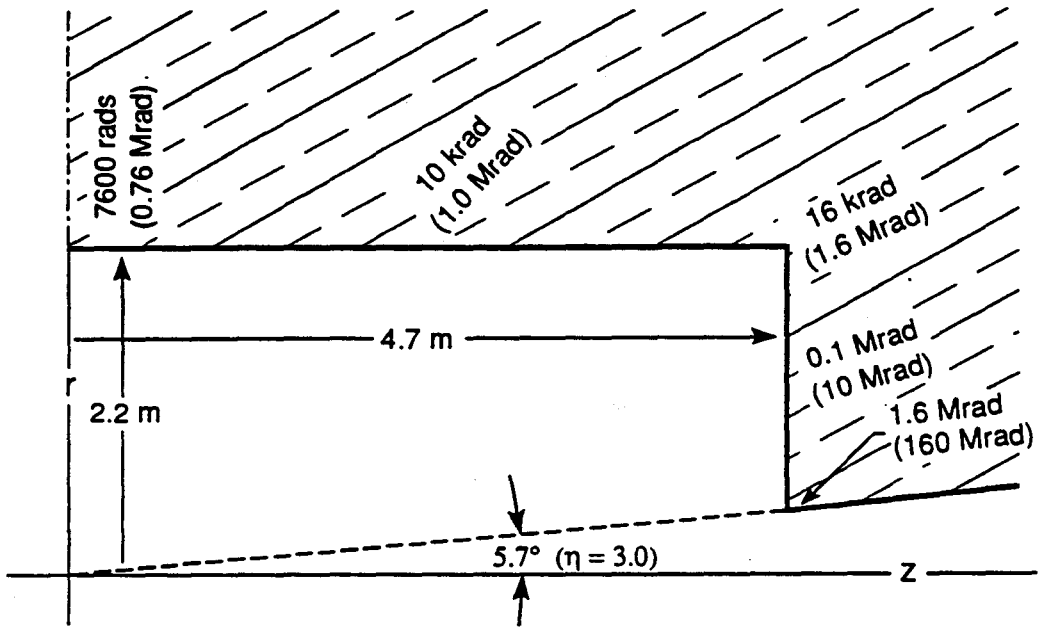

FIG. 6. The maximum ionizing dose in the SDC detector, at SSC design luminosity for one year and (in parenthesis) at $\mathcal{L} = 10^{34}\,\mathrm{cm}^{-2}\mathrm{s}^{-1}$ for 10 years. The maximum dose occurs at electromagnetic shower maximum.

The ionizing dose in the calorimeter reaches a maximum at electromagnetic shower maximum. It varies with angle as $(\sin\theta)^{-2.9}$, and as the inverse square of the distance from the interaction point (IP). Representative values for the SDC detector are shown in Fig. 6. The maximum ionizing dose from hadronic interactions in the calorimeter is smaller by a factor of 30.

The neutron fluence in the calorimeter may be obtained from Ref. 5; it is of serious concern for the readout electronics, particular at small angles.

The outer muon tracking layers are particularly sensitive to soft radiation of several kinds, notably soft gamma rays. Problems are more likely to arise because of various cracks and "hot spots" than from predictable sources. The edges of the holes in the central detector and the front face of the forward calorimeter are obvious potential radiation sources for the intermediate-angle muon drift system.

3.7. HIGH-LUMINOSITY POTENTIAL

The SSC is expected to have the potential for achieving a peak luminosity in excess of the design value of 10^{33} cm^{-2}s^{-1}. The peak luminosity may reach a value about 20 times greater than the design value, although the integrated luminosity may only increase by about a factor of ten[9].

The increase in "physics reach" that will be possible by increasing the luminosity as described above is substantial. In addition to the obvious enhancement of data samples by a factor of ten per unit time, the upper mass limit for the discovery of new, heavy particles would be increased by about 50%[10]. Given the very low event rate, detection of gauge boson pairs with invariant masses above about 1 TeV will require substantial integrated luminosity, beyond that achieved in a standard SSC year, and thus would benefit from the ability to operate at increased luminosity.

The experimental problems in realizing these substantial improvements are also clear: detector technologies must survive in a much-increased radiation field, and the system must be able to cope with an average of, for example, sixteen rather than 1.6 interactions per beam crossing. Some appreciation of the radiation damage issue may be gained by examining Fig. 6. Operation of calorimetry for years at luminosities near 10^{34} cm^{-2}s^{-1} results in peak doses approaching the Mrad level at electromagnetic shower maximum in all parts of the calorimeter, reaching even 100 Mrad near a pseudorapidity of three. Doses from the passage of charged particles scale like the inverse square of the perpendicular distance from the beam. Hence tracking detectors that can survive at about 50–60 cm from the beam at 10^{33} cm^{-2}s^{-1} could be expected to survive at about 1.6 m at 10^{34} cm^{-2}s^{-1} without modification.

The impact of many events occurring during the same bunch crossing is more difficult to quantify. In general terms, the mass or p_t scale of interest is likely to increase with the maturity of the SSC collider and hence with the accumulated luminosity. Although a number of studies have been done on the effects of operation at luminosities near 10^{34} cm^{-2}s^{-1}, the results depend upon the specific physics of interest[11]. We prefer to examine the high-luminosity issue from the perspective of overall detector capability, rather than from the needs of a specific physics process.

In this context, the most critical design choice for the SDC detector is the calorimetry. The calorimeter system is a major investment and is unlikely to be changed quickly to adapt to high luminosity. Although upgrades are always possible, the calorimeter technology chosen initially will need to serve for many years into the SSC experimental program, possibly including at least the initial phase of operation at upgraded luminosity. As discussed in more detail in later sections, the primary calorimetry for the SDC detector will either be based upon plastic scintillator or liquid ionization devices, although a hybrid system may be considered for some regions. The primary difficulty with scintillator calorimetry is the potential for radiation damage, in principle making it less attractive at high luminosity. However, much work has been done recently to improve the radiation resistance of plastic scintillators and we intend to exploit and expand on this work in

preparation of the proposal. At the present time it is not possible to state with confidence that scintillation calorimetry will survive and perform as needed for long operation at high luminosity; more work, including irradiation of electromagnetic modules in a test beam, is required. The possibility of replacing the scintillator modules in high-dose regions (near $|\eta| = 3$) is another option. We expect to take advantage of future scintillator developments. The impediments to using liquid ionization calorimetry are speed of response and the related problem of irradiation of local electronics located within the volume of the calorimeter to optimize the speed of response. We are actively studying these issues as part of calorimeter R&D and expect answers next year.

The viability of full tracking systems at luminosity near $10^{34}\,\mathrm{cm}^{-2}\mathrm{s}^{-1}$ is somewhat problematic at present. By a "full tracking system" we mean one that performs as we expect for a system designed for $10^{33}\,\mathrm{cm}^{-2}\mathrm{s}^{-1}$ luminosity. As has already been noted, tracking near the outer radius of the tracking volume will survive at $10^{34}\,\mathrm{cm}^{-2}\mathrm{s}^{-1}$, but the issue of pattern recognition in an environment with many events occurring from the same crossing needs much more study. Tracking at smaller radii will require either completely new ideas or new application of existing concepts, such as scintillating fibers or very finely divided silicon systems with very hardened electronics. We anticipate that R&D on these systems may well lead to a new tracking detector in a phased-upgrade approach.

The muon system for the SDC detector will have some "stand-alone" capability, but the resolution in the region $-1.5 < \eta < 1.5$ will be somewhat degraded in the absence of a full central tracker.

To summarize, our choice of technologies and our design of the SDC detector will take account of the impact of running for some years at luminosities near $10^{34}\,\mathrm{cm}^{-2}\mathrm{s}^{-1}$. The SDC intends that its detector, with suitable upgrades, be able to handle usefully the highest luminosities available at the SSC.

4. Detector subsystems

4.1. Tracking

The need for charged particle tracking was discussed in section 3. It is our goal to build a tracking system that provides momentum measurements of all charged particles with p_t above a few GeV/c for $|\eta| \lesssim 2.5$. The tracking system also provides a fast trigger for such particles.

These goals can best be realized through the use of several different types of tracking technology. We are exploring the capabilities of a combination of silicon devices, wire chambers, and scintillating fibers. The selection of technologies has not been made, and much research and development remain to be done prior to that selection. We have made provisional decisions on the parameters of the tracking volume, but these are still subject to adjustment based on our evaluation of the technologies, required physics performance, and cost.

In the sections below we present a preliminary conceptual design for the tracking system. In order of increasing radius, the system consists of:

(*a*) Two-dimensional pixel silicon detectors to aid pattern recognition and to detect separated vertices from heavy quark decays and multiple *p*-*p* interactions.

(*b*) A large array of segmented, double-sided silicon strip detectors to provide a powerful pattern recognition tool even in the cores of jets.

(*c*) A wire chamber and/or scintillating fiber system, to provide the high-precision momentum measurements and trigger information for "stiff" particles.

Except for the pixels, each system has both a central and intermediate angle section.

Two possible tracking systems are shown in Figs. 7 and 8. Figure 7 shows the system with wire chambers, and Fig. 8 shows the scintillating fiber tracker. A system based upon a combination of these is also under consideration, but is not shown.

4.1.1. Pixel vertex detector

The detector closest to the interaction point is a high-resolution pixel vertex detector (PVD) producing true three-dimensional position measurements[12, 13]. The PVD covers the rapidity range $|\eta| \lesssim 2.5$. It consists of two concentric cylindrical layers within a radius of 10 cm, extending to $|z| = 40$ cm. Pixel sizes are expected to be 30 μm $\times$ 300 μm in the ϕ and z directions, respectively, and the detectors will be about 300 μm thick. The position resolutions are expected to be better than 10 μm in ϕ and 100 μm in z.

The individual pixel arrays are about 1 cm^2 in area, and are shingled in both z and ϕ to provide complete coverage and to ensure that the average track has a nearly normal angle of incidence. Such a normal angle particle will encounter about 2% of a radiation length in the pixel system. The pixels will be supported by a structure attached to the silicon strip support system.

Because high particle rates are expected, a new electronic system architecture is being developed to buffer information and read out events efficiently. This system architecture is based on the "smart pixel" concept. This is a distributed data-driven system where all circuit functions prior to read-out are on chip. A smart pixel signals when it is struck, stores the analog signal, and is only read out if it is associated with a valid trigger event. Time stamping and sparse read-out circuitry are on chip to minimize external bus activity[14].

The pixel arrays are presently under development, and will either have electronics fabricated directly on the detector silicon or consist of a hybrid detector/readout system using the indium bump-bonding technology developed by Hughes Aircraft Company[15]. The latter readout IC is implemented in a radiation-hard SOI Hughes process. The pixel detector diodes utilize the gettered detector fabrication process developed at LBL[16]. An integrated AC coupling network increases radiation resistance by blocking the flow of detector leakage current to the preamplifier.

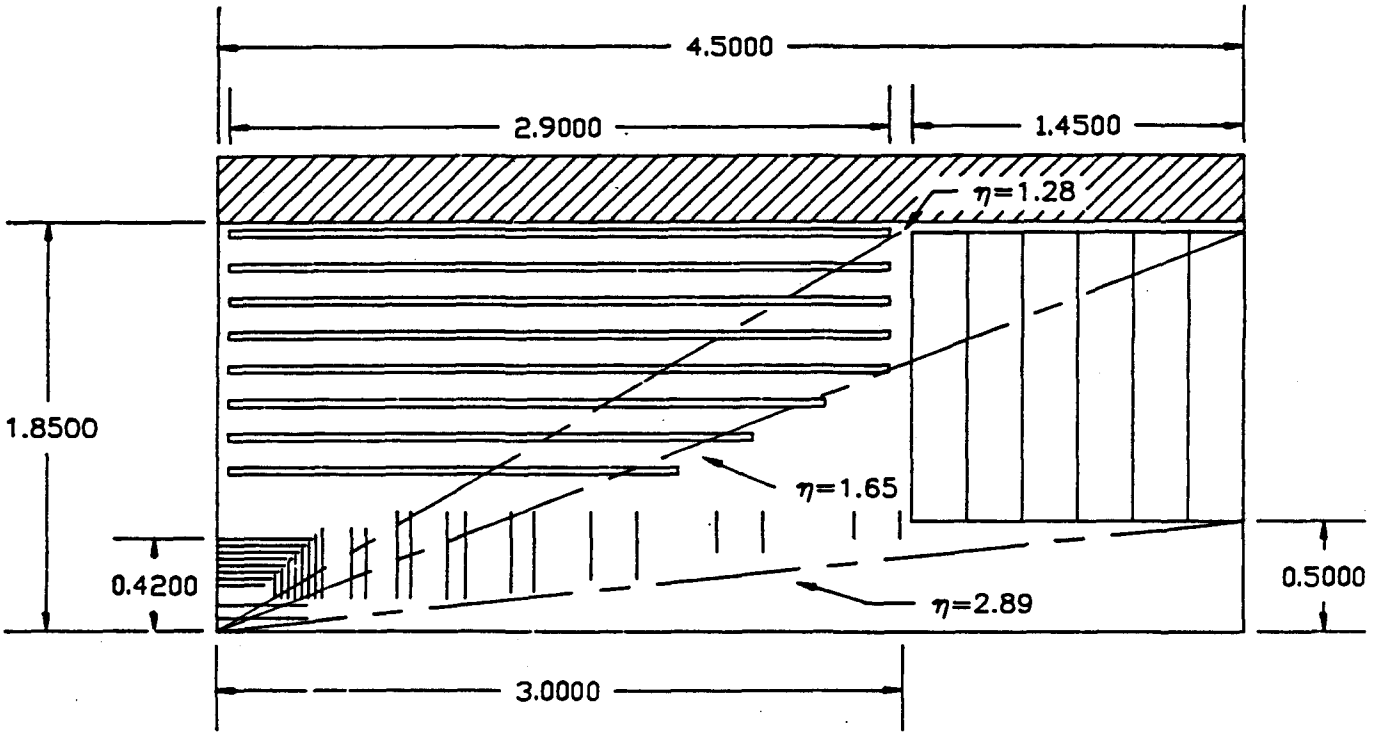

FIG. 7. A pixel, silicon strip, and wire chamber tracking system for the SDC detector.

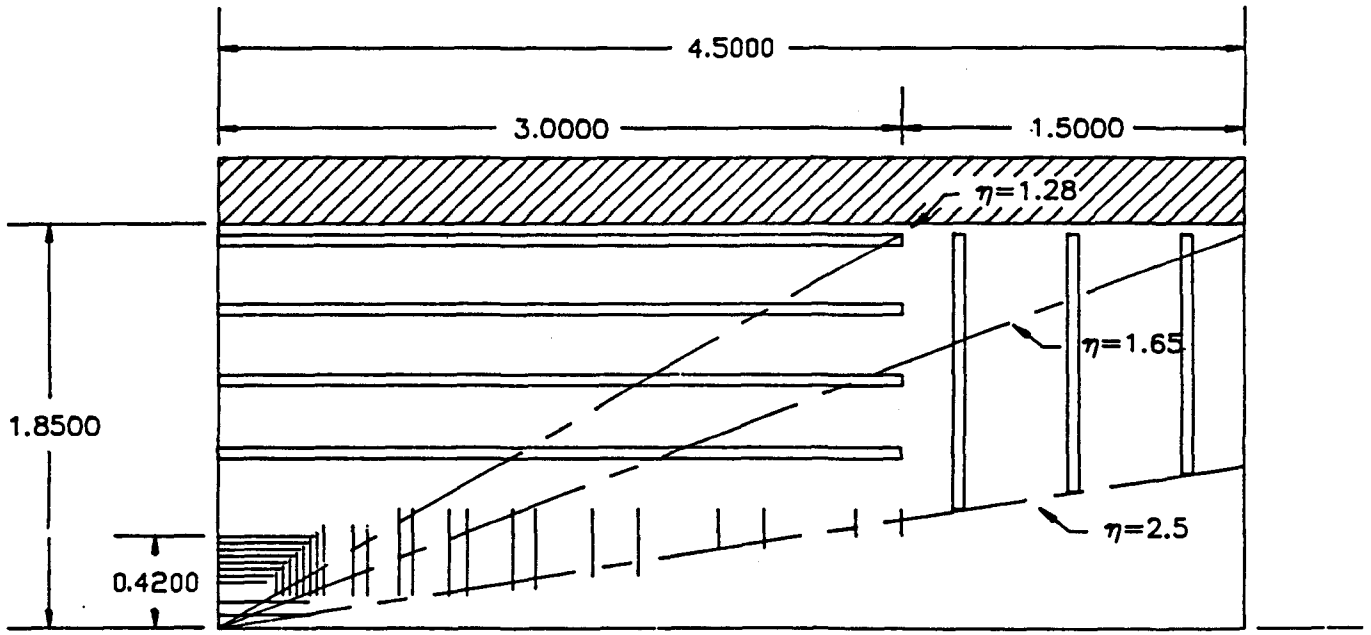

FIG. 8. A pixel, silicon strip, and scintillating fiber tracking system for the SDC detector.

4.1.2. Silicon strip tracker

The silicon strip tracker, which covers the radial region from about 15 cm to 60 cm, represents a significant step beyond the vertex detectors now used in collider experiments. About 32 m^2 of silicon are needed, and the system will contain about 10 million channels. The tracker consists of 300 μm thick double-sided detectors, with axial strips on one side and stereo strips on the other side. Pairs of such detectors with opposite stereo pitch are arranged in superlayers in a cylindrical barrel section and also in planar endcaps. The superlayers allow local hit association into segments that are then further associated into tracks. The transition from barrel to intermediate angle geometry is near 45^0 to minimize the thickness of material traversed by particles. The intermediate angle detectors are spaced along the beam to a distance of nearly 3 m from the IP to allow good momentum measurement at large rapidities. Supports must withstand both thermal and radiation effects, and are expected to be made of either a graphite-based composite or beryllium. Our goal is to have less than 5% of a radiation length at 90° in the silicon strip system.

Individual detectors with sizes up to 3 cm $\times$ 8 cm may be wire-bonded together to make larger units for electronic readout. In the barrel detectors the pitch is 50 μm, whereas in the intermediate angle detectors it varies with radius. The heat load is about 1 mW/channel. Cooling of the detector system is a major concern; studies of evaporation-wick techniques are underway at Los Alamos National Laboratory.

An attractive alternative to double-sided detectors would be detectors made with many short strips aligned on a common substrate[17]. As shown in Ref. 17, short strips allow several front-end optimizations, which reduce total power consumption substantially. Furthermore, these devices could provide adequate z resolution with single-sided strip detectors.

Because of both its high spatial resolution and its excellent two-particle separation, the silicon strip tracker is expected to provide superior pattern recognition even within the cores of jets with transverse momenta up to about 1 TeV/c.

4.1.3. Wire chamber tracking

One option for the tracking technology at radii beyond 60 cm is the use of small-cell chambers with continuous cathodes, either straw tubes or hexagonal arrays. These can provide a fast trigger for particles above some minimum p_t by the simple requirement that the reconstructed track segment near the outer radius point back to the IP within some appropriate uncertainty. They also provide significant pattern recognition and momentum measurement capability[18].

To meet the constraints imposed by radiation damage, current draw, chamber lifetime, gain reduction from large particle flux, hit rate, loss of data because of high occupancy, and pattern recognition in the complex environment, the cylindrical drift cells are made as small as practical[19]. Acceptable current draw and lifetime can be obtained with a 4 mm diameter straw about 50 cm from the beam line; the other operating limits are somewhat less restrictive. This is also the practical lower limit on the diameter from considerations

of track ionization length and electrostatic stability. Occupancy is minimized by use of a fast gas, such as a mixture containing CF_4.

Eight layers of cells are close-packed to form a superlayer, as shown in Fig. 9. A half-cell stagger between layers permits resolution of right-left and crossing time ambiguities. Track segments found within the superlayers are linked to form tracks. The on-chamber electronics (discussed in section 4.6) also constructs segments for use in the trigger. The z coordinate is measured by means of stereo layers. With a spatial resolution of 100–150 μm per wire in the r-ϕ projection, the expected resolution in z is 2–3 mm. The superlayers are ordered axial, $+3°$, axial, $-3°$, etc., for a total of eight equally-spaced superlayers spanning 0.70 m $< r <$ 1.8 m. The arrangement is shown in Fig. 7. Straws up to 3.5 m long with intermediate sense wire supports every 80 cm have been made that operate at the required voltage. The maximum possible straw length is limited by signal attenuation, and is a critical design issue. At present we make the conservative assumption that straw lengths are about 3 m, and hence there needs to be an electrical break near the middle of the barrel chambers.

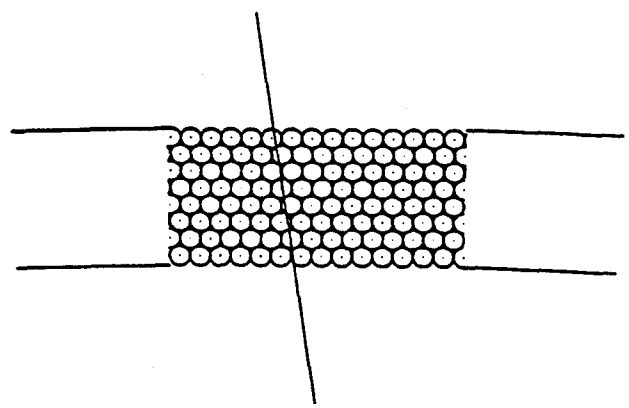

FIG. 9. Cross-sectional view of the 8 layers of a superlayer of straws.

A design with hexagonal cells constructed with a carbon-fiber composite is being considered as an alternative to the cylindrical array of straws. These cells have the advantage of providing excellent structural support, so that the tracking system can contain less material.

For the intermediate angle tracking region ($1.3 \leq |\eta| \leq 2.5$) two approaches involving wires perpendicular to the beam direction are being considered. The first employs crossed planar superlayers of straw tubes. The second involves the use of arrays of transverse drift cells which are optimized for fast track finding and reconstruction, much like the intermediate angle track detector in the H1 experiment at HERA[20]. In the latter case this is efficiently achieved by means of radial sense wires, but the requirements of both a fast gas with large Lorentz angle and a high rate capability at SSC mean that further consideration of the wire orientation is necessary; this work is under way. Such a detector would contain about 300 azimuthal wedges to meet the constraints on current draw and occupancy over the full radial range. The coordinate along the wire would be measured with planes of wires tilted at small angles to the nominal wire direction.

We are considering readout of the charge for some fraction of the wires in the system. Indeed, in the intermediate angle region, charge readout opens up the possibility of enhancing electron identification by detecting transition radiation x-rays[21].

4.1.4. Scintillating fiber tracking

Scintillating fibers provide another option for particle tracking because of their intrinsically fast response and fine granularity[22]. In addition to providing pattern recognition and momentum analysis, they allow a first-level trigger with p_t sensitivity. Simple hit-bit combinatorial logic can be used to determine the sagitta of stiff tracks. Furthermore, fiber trackers have the following desirable features: (*a*) they are insensitive to magnetic fields and RF noise, (*b*) no heat is dissipated within the tracking volume, (*c*) there is no gas, (*d*) they are mechanically simple, and (*e*) the material is of low density. The readout electronics for such a structure just requires one latch per fiber.

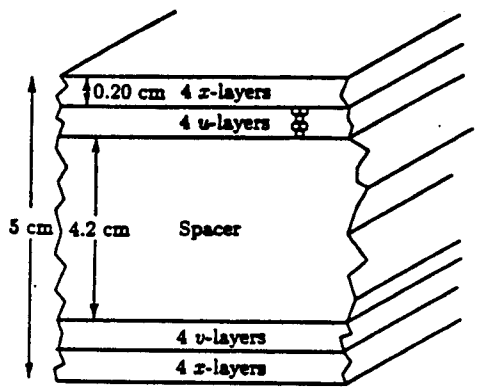

FIG. 10. Cross-sectional view of the 16 layers of the outer scintillating fiber superlayer.

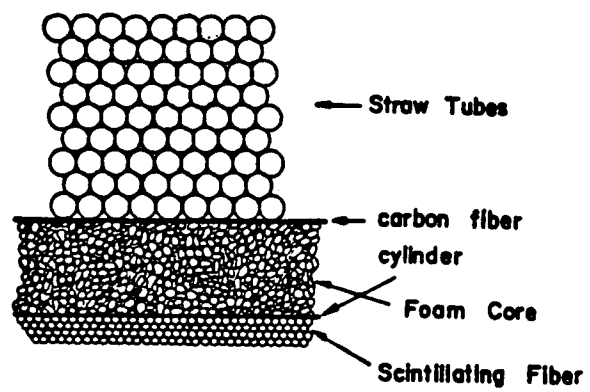

FIG. 11. Cross-sectional view of a straw/fiber hybrid superlayer.

In the silicon/fiber scenario the central tracker contains about 1.8×10^6 fibers of 500 μm diameter and 3 m length, deployed in four superlayers as shown in Fig. 8. Each superlayer contains two sets of axial fiber layers separated by 4 cm to measure ϕ. The outer two superlayers also include narrow angle stereo layers to determine the longitudinal coordinate. One of these superlayers is shown in Fig. 10. The flexibility of fibers allows us to choose the stereo angle of the superlayers (for example 4.5° and 3°) to avoid ghosts in coordinate reconstruction and pattern recognition. With this particular arrangement of superlayers, a local track vector can be formed in r-ϕ whose angular uncertainty is 2 mrad. This feature should provide good layer-to-layer pattern recognition as well as the rapid identification of high p_t tracks. The effective two-track resolution is 1 mm, and the occupancy will be $< 1\%$ ($< 10\%$) per fiber per beam crossing for luminosities $\mathcal{L} = 10^{33}$ $(10^{34})\,\mathrm{cm}^{-2}\mathrm{s}^{-1}$.

Several intermediate-angle tracker designs are being considered. One of these has three planar superlayers and is comprised of a total of 2×10^5 fibers, 1 mm in diameter and 2 m long. The flexibility and field immunity of fibers allows for novel topologies in the superlayers.

The standard central detector element consists of a scintillating fiber 500 μm in diameter, smoothly coupled to a non-scintillating fiber that transmits the light outside the detector volume to a solid-state photodetector[23]. To provide for adequate radiation resistance, new scintillation dyes with emission between 500 nm and 700 nm are utilized. This wavelength range is particularly well matched to the solid-state photodetectors which are now available, such as the solid-state photomultiplier (SSPM). These are being used by several groups within the collaboration and have a quantum efficiency of 60% in this wavelength region. They have to operate at about 7°K. Optimization of SSPMs for speed and quantum efficiency is taking place in collaboration with the Rockwell International Science Center[24].

4.1.5. Variants on wire-chamber/fiber tracking systems

There are variants on the above systems that are under study in R&D programs within the collaboration. One possibility is the use of scintillating strips instead of scintillating fibers. Scintillating strips, 200 μm wide and 2 mm along the radial direction, are formed into a laminated structure. Waveshifter fibers 200 μm $\times$ 200 μm are bonded to the upper and lower surfaces of each of the strips to transport the scintillation light out of the active volume. The advantage of such a system, if used at the outer radii, is to provide rapid identification of stiff, hence radial, tracks from pulse height information.

Another variant, being studied for use in the central tracker, is a hybrid of straw tube and scintillating fiber detectors. In a preliminary design, longitudinal straw tubes are used to measure ϕ and helical layers of scintillating fibers measure z. Such a hybrid detector takes advantage of the lower cost of straw tubes to fill large volumes for improved pattern recognition capabilities and the flexibility of scintillating fibers in making helical windings for the stereo measurement. The mechanical support structure would utilize carbon-fiber composite cylinders with the option of embedding the scintillating fibers in the support structure. The cross section of a hybrid superlayer is shown in Fig. 11.

4.1.6. System performance characteristics

The performance of the proposed tracking system is summarized in Figs. 12 and 13 and Tables 2 and 3. Fig. 12 shows the momentum resolution versus η for the pixel/silicon strip/wire chamber and pixel/silicon strip/scintillating fiber systems. These resolutions, based on the single-measurement resolutions given in Tables 2 and 3 with an assumed 100% measurement efficiency, are better than our stated goal of $\lesssim 0.2p_t$ (TeV/c), but are optimistic in their neglect of inefficiencies and systematic errors. Fig. 13 shows the impact parameter resolution at the IP determined by the pixels and silicon strip system, again assuming 100% efficiency and the point resolutions given in the tables. These resolutions are comfortably below the impact parameter values expected from B decay (typically 100 μm).

4.1.7. Technical issues

The final design of the SDC tracking detector will be guided by R&D work being done in several SSC subsystem and generic programs. Funding at an enhanced level will

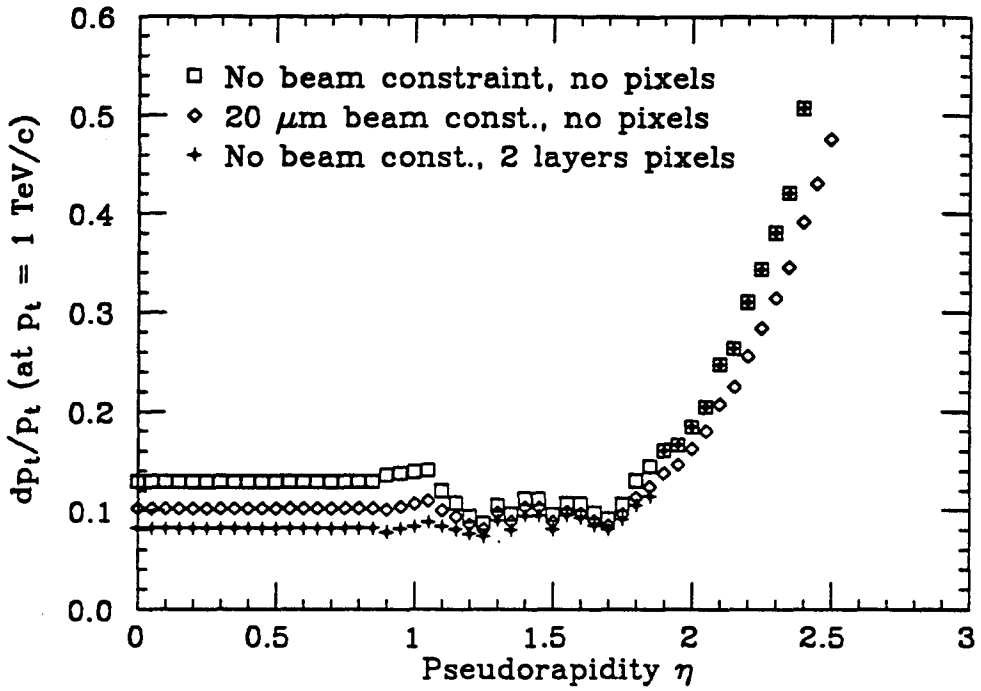

FIG. 12. Momentum resolution *vs.* η for either the pixel/silicon strip/wire chamber outer tracking system or the pixel/silicon strip/scintillating fiber outer tracking system, based upon 100% measurement efficiency and resolutions given in Tables 2 and 3. Systematic errors are not included.

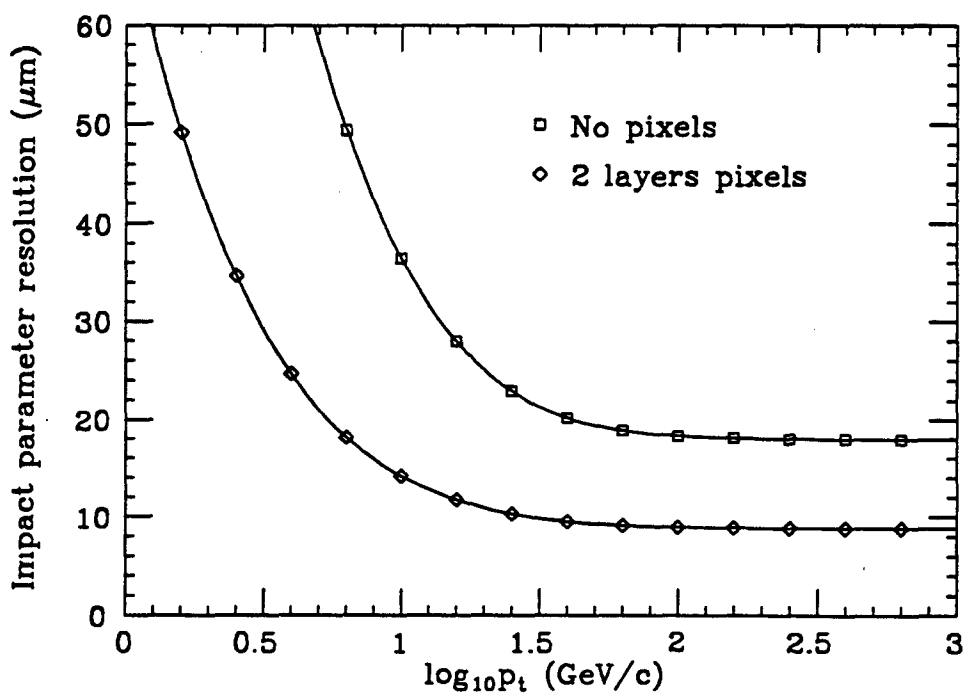

FIG. 13. Impact parameter resolution at the interaction point as a function of momentum for the pixel/silicon strip vertex detector system for a 90° track. The resolutions given in Tables 2 and 3 are assumed, along with 100% detection efficiency.

Table 2

Central tracking: $|\eta| \leq 1.5$.

	Pixels	Silicon	Wire Chamber	Scifi
Total number of elements	15×10^6	2×10^6	2.5×10^5	1.7×10^6
Number of superlayers	2	4	8	4
Measuring layers/superlayer	1	4	8	8, 8, 16, 16
Occupancy per element (In 2 T field at $\mathcal{L} = 10^{33}$ cm^{-2}s^{-1})	10^{-4}	10^{-3}	$< 10^{-1}$	$< 10^{-2}$
Total radiation lengths at normal incidence	1.5%	5%	6%	6%
Resolution/measurement	10 μm $\times$100 μm	15 μm	150 μm	120 μm
Two-track resolution	100 μm $\times$500 μm	150 μm	2 mm	1 mm

Table 3

Intermediate angle tracking: $1.5 < |\eta| \leq 2.5$

	Pixels	Silicon	Wire Chamber	Scifi
Total number of elements (both ends)	7×10^6	8×10^6	6×10^4	2×10^5
Number of superlayers per end	2	5	6	3
Measuring layers/superlayer	1	4	12	12
Occupancy per element (In 2 T field at $\mathcal{L} = 10^{-33}$ cm^{-2}s^{-1})	10^{-4}	10^{-3}	$< 10^{-1}$	10^{-2}
Total radiation lengths at normal incidence	1.5%	6%	6%	8%
Average radiation lengths contributed by end of central tracker ($1.3 < |\eta| < 1.8$)	—	—	15%	3%
Resolution/measurement	10 μm $\times$100 μm	15 μm	150 μm	250 μm
Two-track resolution	100 μm $\times$500 μm	150 μm	2 mm	1 mm

be needed for this R&D in FY91. The relevance of this research to our tracking detector design is summarized briefly below.

The viability of the pixel and silicon strip system that occupies the inner part of the tracking volume depends on the resolution of such issues as fabrication technology, circuit design, radiation hardness, mechanical and thermal stability, precision alignment, adequate heat removal and ease of assembly. Studies under both generic and subsystems R&D programs are addressing these fundamental questions[13, 17, 25].

For the outer part of the tracking volume, wire chamber technology is mature, al-

though its application in the SSC environment poses unprecedented challenges. Development of a wire chamber tracking system design, including minimizing material in the supports and end regions, incorporation of electronics, gas manifolds and high voltage distribution, precision alignment, thermal management, and computer simulation studies of track finding is being supported under major subsystem R&D programs[26, 27]. The subsystem R&D includes investigation of the hexagonal cell option and the R&D specific to the intermediate angle tracking system. The option of a hybrid straw tube/ scintillating fiber outer tracker is also being evaluated. This research will determine the feasibility of constructing long straw tubes in a modular shell structure or on a cylindrical base composed of a laminate of carbon-fiber and scintillating fibers.

The use of scintillating fiber technology for tracking layers would eliminate the need for gas and high voltage distribution and heat removal but presents new challenges in photodetection. Central to this program are the development of radiation hard scintillators and solid state photodetectors and associated cryogenics. Subsystem R&D efforts are underway addressing each of these issues[28].

Extensive simulation and design efforts incorporating the above R&D results will be the inputs into the final technological choices and cost optimization.

In addition to the subsystem research described above, we are requesting additional support for engineering design leading to the integration and assembly of the tracking subsystems into the overall SDC detector tracking system. These issues include an evaluation of the mechanical support structures, integration of the tracking system components, cabling and power distribution, and development of the SDC detector assembly, maintenance and repair procedures. This system engineering and design will be a cooperative effort among LANL, LBL, ORNL and Westinghouse Science and Technology Center.

4.2. Solenoidal magnet

A solenoidal superconducting magnet will provide the magnetic field required for charged particle momentum determination in the central detector. Significant progress has been made in understanding the engineering details of such a magnet. We have chosen a design with the calorimetry outside the coil. This geometry provides the required field in the tracking volume with a coil of minimum physical size and stored electromagnetic energy. It also allows good access to calorimetry for cabling and maintenance. However, the material of the coil, support cylinder, and vacuum shells are in front of the electromagnetic calorimetry, and must be made "thin," in terms of radiation and absorption lengths, to be sure that their effects on electromagnetic energy resolution for physics processes of interest at SSC energies are small[29]. A coil with a thickness of $2X_0$ in front of the calorimeter has been shown to have negligible effects on the missing p_t spectrum [30]. Furthermore, although studies are still in progress, we believe that careful attention to the calorimeter geometry near the ends of the coil can result in small or negligible degradation of missing E_t resolution and calorimetry coverage. Finally, since eight solenoids of approximately the size required for an SSC detector have been built in the past 8 years

(see Table 4), we have confidence that a satisfactory "thin" coil magnet can be in place when SSC experiments begin.

Table 4

Summary of existing solenoids for colliding beam experiments, where B = central field, L = thickness, E = stored energy, M = cold mass and $R = E/M$.

Experiment	B(T)	$L(X_0)$	E(MJ)	M(tons)	R(kJ/kg)
CDF	1.5	0.86	30	5.6	5.4
TOPAZ	1.2	0.70	19.5	4.5	4.3
VENUS	0.75	0.52	11.7	4.3	2.7
CLEO-II	1.5	2.5	25	7.0	3.6
ALEPH	1.5	~1.7	130	25	5.5
DELPHI	1.2	4.0	109	25	4.3
H1	1.2	1.2	120	25	4.8
ZEUS	1.8	0.90	10.5	1.9	5.5
SDC Type-L	2.0	1.14	317	48	6.6
SDC Type-I	2.0	1.00	190	24	7.9
SDC Type-S	2.0	1.23	205	33	6.2

The magnet dimensions will be determined by an optimization procedure that balances conflicting requirements on the magnet parameters. The desire for the best momentum measurement over the largest solid angle with plausible extrapolations of existing tracking technology argues for a large coil with high field integral. On the other hand, the desire to minimize coil material in front of the electromagnetic calorimetry and minimize the cost of calorimetry argues for small radius and length. This optimization process is still in progress. However, its seems likely that a coil with a useful inner radius of 2.0 m $\pm$ 0.3 m, a tracking length of 8–9 m and a field integral of 4.0 $\pm$ 0.5 T-m will be chosen. Our design studies[31, 32] have focused on the engineering problems of a "thin" superconducting coil of approximately these dimensions. The results of these studies support the assertion that a magnet with these dimensions and field integral can be built with a material budget that corresponds to 1.2 ± 0.2 radiation lengths for a particle traversing the coil at 90° to the solenoid axis. Three design options have been explored. We call these Type-L, Type-I, and Type-S. Each has advantages and disadvantages, but there are many common design features. Differences in the basic geometries of the three types are illustrated in Fig. 14.

In the Type-L magnet design, the coil is located as close as possible to a ferromagnetic flux return yoke. This results in a very uniform magnetic field in the bore and negligible fringe fields. The radial field components are small, as is the resulting compressive force on the coil. However, the proximity of the coil to the iron yoke results in axial and radial decentering forces that must be resisted by supports from the 4.5 K coil to the room

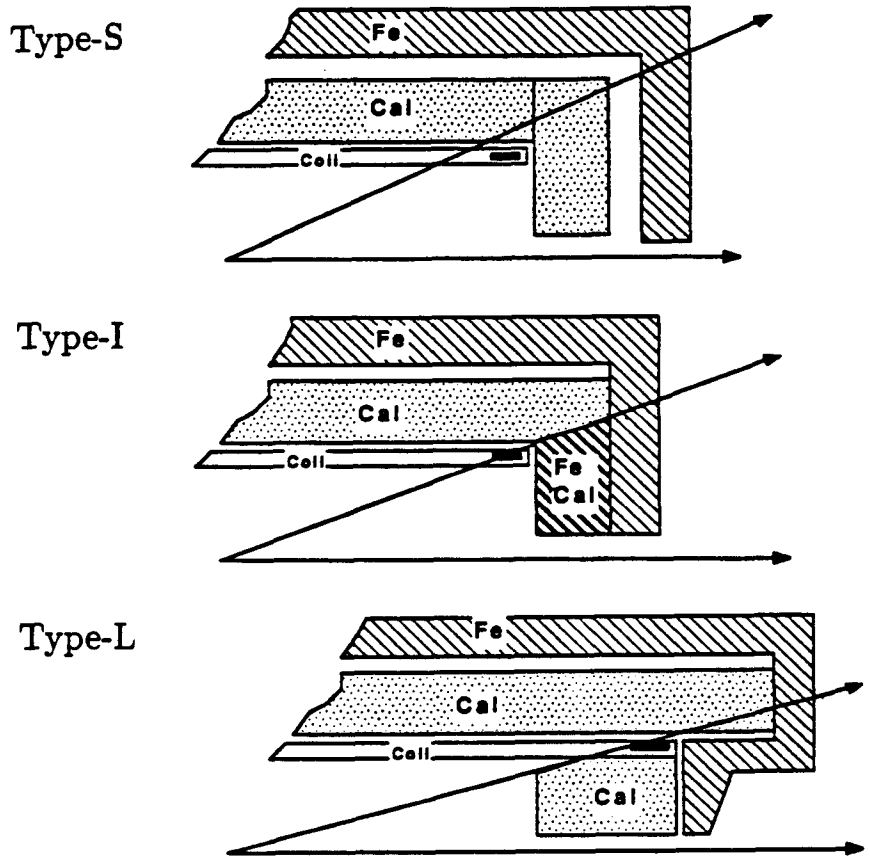

FIG. 14. Coil-iron-calorimeter geometries for the solenoid types under consideration for the SDC detector.

temperature yoke. In addition, since the coil penetrates the calorimetry, care must be taken ensure that the calorimetry performance in the coil end region is not compromised.

The Type-I magnet is very similar to Type-L except that ferromagnetic calorimetry replaces the flux return yoke near the ends of the coil. This type also has a uniform internal field, a negligible fringe field, and compressive and decentering forces on the coil similar to that of Type-L. However, since the coil does not penetrate the calorimetry, the detector hermiticity is potentially better than Type-L provided that the thickness of material in the coil ends remains sufficiently small and that suitable ferromagnetic calorimetry can be developed.

The Type-S magnet does not have an iron flux return near the end of the coil. This allows the calorimetry to wrap around the end of the coil in a more hermetic way than the Type-L design, without the requirement of carrying flux as in Type-I. However, the magnetic field in this coil is much less uniform than in the Type-L or Type-I designs, especially near the ends of the winding, and large fringe fields extend into the volume occupied by calorimetry and other external detectors. The large radial component of the magnetic field that penetrates the coil produces a very large magnetic compressive force on the winding (Fig. 15) that must be resisted with a structure adequate to prevent quenches induced by coil motion. Because of the large distance to the ferromagnetic return yoke, the axial and radial decentering forces are negligible and supports must carry essentially

only the coil cold mass. One additional worthwhile feature of such a coil is that it could be tested to full current at a vendors factory since a return yoke is not required.

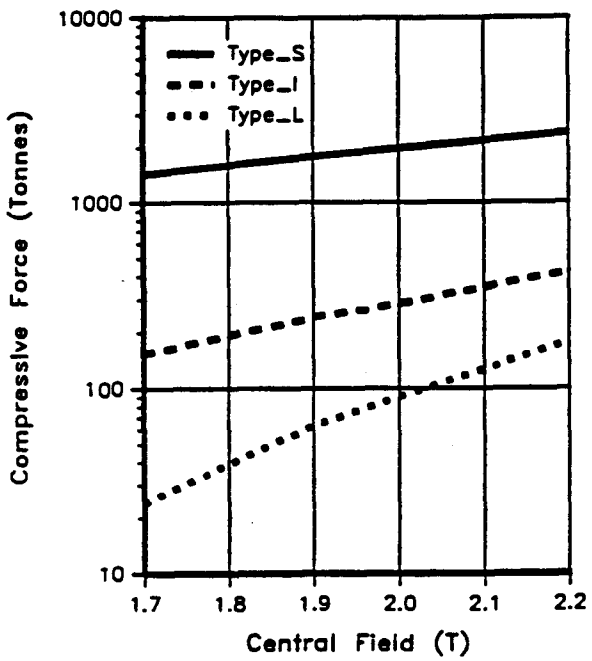

FIG. 15. Axial compression of coil as a function of field for the three solenoid types.

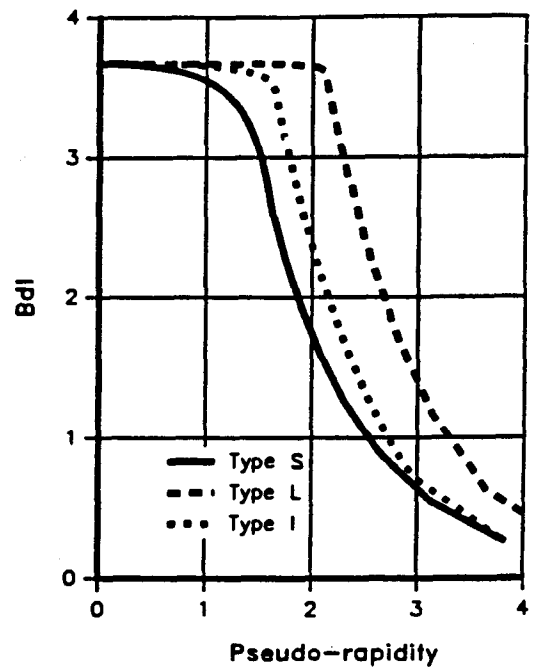

FIG. 16. Bending power versus pseudorapidity for three solenoid geometries in the tracking volume $r < 1.8$ m, $|z| \leq 4.5$ m.

A summary of qualitative advantages and disadvantages of each configuration appears in Table 5. Quantitative comparisons are more difficult and are crucial to making such an important design decision.

Tentative design parameters for the three magnet types are given in Table 6. Although we currently believe that all are technically feasible, substantial magnet design and detector simulation studies are required to determine which is the best choice.

4.2.1. Thin solenoid design criteria

General. Solenoidal coils that are thin in both radiation and absorption lengths have two common design features: (1) the coil, outer support cylinder, radiation shields and vacuum vessel shells are aluminum and (2) the coil is indirectly cooled by liquid helium flowing through aluminum tubing attached to a support cylinder. These features result in a magnet which is intrinsically less stable and potentially less reliable than one with a liquid helium bath-cooled coil and stainless steel vessels. Reliability is difficult to quantify but refers to the short and long term availability of the magnet for use as part of the detector. Five of the eight solenoids found in Table 4 are thin and satisfy the above requirements. All have eventually proved to be reasonably reliable components of collider detectors. The stored energy in the SDC detector solenoid is larger by a factor of 3 than

Table 5

Qualitative comparison of magnet types.

	Type-L	Type-I	Type-S
B in tracking region (Fig. 16)	uniform	uniform	non-uniform
Fringe field (Fig. 17)	negligible	negligible	large
Calorimetry hermiticity	worse?	better?	better?
Calorimetry volume	larger	minimal	minimal
Axial force on coil (Fig. 15)	small	medium	very large
Decentering forces	large	medium	small
Test without yoke?	partial	partial	full

Table 6

Coil Parameters (T_{max}=100 K, V_{max}=500 V).

	Type-L	Type-I	Type-S
Inner radius of cryostat (mm)	1850	1850	1850
Outer radius of cryostat (mm)	2200	2200	2200
Total length of cryostat (mm)	15000	9000	9000
Total weight (tonnes)	60	31	40
Coil cold mass (tonnes)	48	24	33
Central Field B at $z = 0$ (T)	2.0	2.0	2.0
Nominal operating current (A)	8,000	8,000	8,000
Stored energy E_0 (MJ)	317	190	205
Winding scheme	single layer	single layer	single layer
Self inductance (H)	9.9	5.9	6.4
Superconductor (NbTi/Cu)	0.5/0.5	0.5/0.5	0.5/0.5
Aluminum stabilizer (RRR)	1200	1200	750
Conductor cross section (mm^{-2})	4.83×54	4.83×42	4.4×50
Overall current density J_0 (A/mm^2)	30.6	39.4	36.4
Thickness of support cylinder (mm)	15	21	24
Axial compressive force (tonf)	91	285	2200
Axial de-centering force (tonf/cm)	64	37	3.8
Estimated total thickness (X_0)	1.34	1.27	1.39
Est. with honeycomb vac. shell (X_0)	1.14	1.07	1.19
Est. with honeycomb vac. shell (λ_0)	0.24	0.23	0.26

the largest of these. Nevertheless, we believe that with careful engineering it can be as or more reliable than the thin superconducting coils now in operation.

Conductor thickness. Indirectly cooled superconducting coils are more liable to quench than bath-cooled coils, and therefore a reliable thin solenoid must be designed to survive

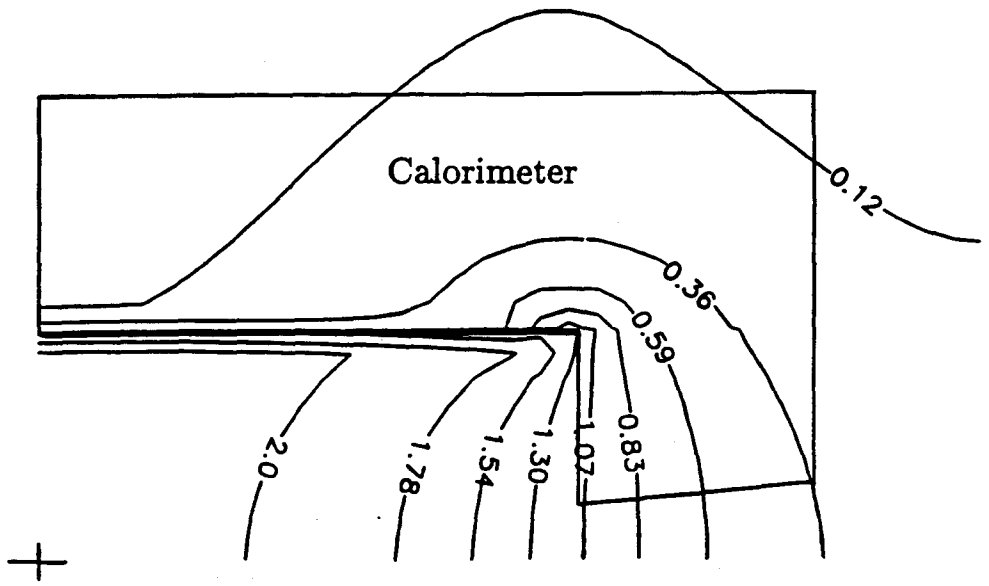

FIG. 17. Field for a Type-S solenoid

numerous quenches without degradation of its performance. It was recognized by the designers of the thin solenoids listed in Table 4 that if the maximum temperature in the coil following a quench did not exceed about 100 K the performance of the coil would be unaffected by repeated quenching. We have chosen this temperature as a design criterion for the SDC detector solenoid. Given this maximum temperature and the coil diameter and field, the radial thickness of the conductor varies approximately linearly with the electrical resistivity of the aluminum used in the conductor. This resistivity is characterized by the residual resistivity ratio (RRR) which is defined as the ratio of the room temperature resistivity to that at 4.5 K. The average RRR for the eight existing solenoids in Table 4 is 1600. It is reasonable to expect the RRR of the completed SDC coil to be above 1500, but we use RRR = 1200 for design purposes.* The resistivity of the conductor aluminum is determined by its purity and strain state, increasing as the strain and the number of strain cycles increases. The coil outer support cylinder package is designed so that the conductor strain does not exceed 0.001 (0.1%). Having chosen the maximum hot spot temperature and the aluminum RRR, the operating current is a free variable, with the stabilizer thickness varying inversely with the square root of the current.† However, because Joule heating in the superconducting splices and current leads increase with current squared, and because of the room-temperature switch-gear and bus requirements, 8–10 kA is chosen as a practical operating current range. The eight earlier solenoids all operate at about 5 kA. Similar practical considerations have led to a choice of 500 V as the maximum discharge terminal voltage. Finally, R, the ratio of the stored energy of the magnet to its effective cold mass is a measure of how "aggressive" a given

* A lower value (*e.g.* RRR = 750) might be more appropriate for a Type-S magnet, to provide higher mechanical strength.

† The stored energy can be extracted faster from a magnet with a higher-current lower-inductance coil, providing better quench protection. The aspect ratio of a higher-current conductor also makes coil winding easier.

design is at minimizing material. Values are listed in Table 4 and may be compared with 9.4 kJ/kg that is required to raise all the aluminum in the cold mass uniformly to 80 K.

Vacuum vessel shells. We will follow the standard of the Compressed Gas Association for cryogenic tanks and design the cylindrical outer vacuum shell for a collapse pressure differential of 2 atm. The cylindrical inner shell is susceptible to collapse only if the insulating vacuum space goes above atmospheric pressure. We believe that this shell may be designed for a collapsing pressure differential of 0.2 atm (3 psid). The use of honeycomb vacuum vessels rather than solid aluminum shells results in a 20% savings in thickness, as measured in radiation or interaction lengths.

4.2.2. Research and development plans

A great deal of further computational work must be done to provide input to the process of choosing which solenoid option is the best for the SDC detector. Considerable R&D effort will be required to complete the design report of the magnet chosen by the collaboration. This section considers some of the R&D work required, independent of solenoid type.

Magnetostatic, structural and thermal calculations. Further finite-element calculations must be done to optimize the coil-iron-calorimeter geometry from both detector physics and magnet engineering points of view, to minimize the thickness and to provide adequate cooling of the coil. Graded current distributions will be studied as a means of improving the field uniformity.

Conductor studies. The stress-strain behavior of conductors with RRR = 1200 must be measured so that the conductor strain may be kept below 0.1%. The resistivity of the conductor as a function of temperature and magnetic field should also be measured. The technique of making low-resistance splices between conductors must be developed, especially if an operating current near 10 kA is chosen. Some length of conductor of near final dimensions will be purchased for these tests. Manufacturing techniques for obtaining long lengths of a high aspect ratio conductor consisting of high-purity aluminum extruded around a multifilament superconducting cable must be developed.

Quench behavior. Further, more detailed quench analysis is needed to give confidence that the performance of the magnet will be unaffected by a quench, even one accompanied by a failure of the quench detection and fast dump circuit.

Honeycomb vacuum vessel. The use of aluminum honeycomb rather than plate for the outer vacuum shell to reduce the radiation thickness is desirable and should be investigated. A suitably scaled model of a honeycomb vacuum shell should be procured to investigate fabrication and vacuum issues.

Reliability analysis. A thorough reliability analysis must be made of all components and subsystems that comprise the solenoid magnet. The goal of this analysis is to essentially guarantee that the solenoid magnet will be available for the detector or can be made available shortly (two or three months) after any credible incident takes it out of service.

4.3. CALORIMETRY

In any SSC detector the calorimeter is the only component able to measure jet energies. It is also essential for the detection of neutrinos and other unseen particles by energy imbalance. In the SDC detector the calorimeter will also be essential to distinguish electrons from charged hadrons. As a consequence, the calorimeter will make a large contribution to the achievement of the SDC physics goals. Because of its size and complexity it will also have a major impact on the budget.

In the following we describe the environment in which the calorimeter must function; the key goals and requirements that the design must meet; the candidate technologies for the main calorimeter ($|\eta| < 3$); the forward calorimeter; and the R&D that must be accomplished to provide a basis for the final choice of calorimeter design.

4.3.1. Environment

The significant features of the environment in which the calorimeter must function are:

(*a*) The calorimeter must provide a free volume about 4.5 m in diameter by about 9 m long that contains the solenoid magnet and the central tracking devices.

(*b*) For the short coil option, significant magnetic fields ($\lesssim 0.5$ T) will permeate parts of the calorimeter. For the long coil option, although the barrel calorimeter is in a field free region, the calorimeter endcaps must endure the full field and carry it to the return yoke. For the "Type-I" coil, the magnetic field is returned at least in part by the calorimeter itself. For each option a portion of the calorimeter must have a readout that is either immune to the field or removed to a field-free region.

(*c*) The maximum ionizing dose rate occurs at electromagnetic shower maximum in the calorimeter. It is modest in the barrel part of the calorimeter, but reaches extreme values (1.6 Mrad/yr at the SSC design luminosity) at $\eta = 3$ (see section 3.7). The calorimeter composition also influences the neutron flux seen by central tracking devices.

(*d*) The event rate is 10^8 interactions s^{-1} at the SSC design luminosity; it may rise by one order of magnitude with further luminosity increases over the life of the experiment. This rate sets the natural scale for the combination of detector time resolution and granularity needed to suppress pileup. The 60 MHz beam crossing rate imposes a limit beyond which further improvements in time resolution do not help.

(*e*) Near $\eta = 0$, approximately $0.07X_0$ of material is crossed before particles enter tracking detectors able to contribute to the Level 1 trigger. An additional 1.3–1.6 X_0 of track detector and coil material is traversed before the calorimeter is reached.

4.3.2. Design goals and practical requirements

The performance goals enumerated below are defined by consideration of the physics goals of the experiment:

(*a*) The stochastic resolution terms are $\sim (0.2 \pm 0.05)/\sqrt{E_{em}}$, and $\sim (0.5 \pm 0.2)/\sqrt{E_{had}}$. These numbers refer to FWHM/2.3; tails on the resolution are extremely important and must also be specified and controlled.

(*b*) The constant term in the calorimeter resolution (asymptotic resolution) should be 0.01–0.02 (EM) and 0.02–0.04 (hadronic). The design features that affect this requirement are e/h,* spatial non-uniformity over the "good" fiducial region, cracks or dead regions, containment (depth of calorimeter), crosstalk between readout channels, time stability, coherent noise in the electronics, and the dynamic range of the readout system. Quick, easy and accurate calibration is needed, including *in situ* calibration if required to track long term drifts.

(*c*) Both the EM and hadronic response(jets) should be linear to $\sim 2\%$ after correction up to about 5 TeV.†

(*d*) The contribution to E_t resolution induced by integrated event pileup and electronic noise should be less than 1 GeV in a cone $\sqrt{\Delta\eta^2 + \Delta\phi^2} < 0.15$ at $\mathcal{L} = 10^{33}\ \mathrm{cm}^{-2}\mathrm{s}^{-1}$.

(*e*) The segmentation of the hadronic section of the calorimeter in η and ϕ should be $\Delta\eta = \Delta\phi \simeq 0.05$–$0.07$. The segmentation for $|\eta| > 1.5$ maintains this value until the physical tower width falls to a value approximately equal to the FWHM hadronic shower width at shower maximum (about 10 cm), after which the tower width remains constant.

(*f*) As will be emphasized in section 4.4, electron identification is extremely important and relies on both calorimeter and charged track analysis.

(*g*) Missing E_t ($\not{E}_t$) is an important signature of new physics. The calorimeter should cover the region $|\eta| \lesssim 5$ hermetically enough that the missing E_t signal is dominated by neutrinos for $\not{E}_t \gtrsim 50$ GeV.

(*h*) It must be possible to change the calorimeter triggering strategy as needed to match an evolving physics emphasis as the SDC detector explores a new energy regime.

Of at least as great importance are the following practical requirements:

(*i*) The calorimeter must survive and perform within tolerances in the intense radiation environment.

---

* For a uniform calorimeter, noncompensation produces a nearly energy-independent contribution $14\%|1 - e/h|$ to the resolution, where e is the detector response to electromagnetic energy deposition and h is the response to low-energy hadronic activity.

† The linearity depends on the "e/π" ratio, which is affected by gate time as well as calorimeter composition and saturation.

(*j*) The calorimeter must be reliable. Rates of failure should be predictable and expected to be negligibly small. Modes of failure should be non-catastrophic, *i.e.* not result in loss of a significant fraction of the calorimeter information for a long time.

(*k*) The calorimeter must be affordable within the overall scope of the detector. Thus the choice of technology must reflect simplicity, ease of construction, and predictability of cost.

(*l*) The operating cost of the calorimeter must be acceptable. This includes the cost of maintenance, recalibration, consumables, reconditioning and replacement of components, and associated technical salaries.

(*m*) The design must satisfy safety requirements as defined by the SSC Laboratory.

(*n*) The chosen technology must allow a realistic construction schedule. This should include successful beam test of a model calorimeter large enough to contain high energy hadronic showers before a calorimeter technology is selected for the final design; and successful beam tests of prototype modules before large-scale module production begins.

(*o*) The plan for prototype R&D and testing and calibration of production modules must be compatible with the availability of existing and projected test beams.

4.3.3. Candidate technologies

For reasons of economy of construction and simplicity in the analysis we strongly favor a calorimeter with a composition that does not vary significantly with η, at least for $|\eta| < 3$. We also favor use of a single calorimeter technology within that region. Several features of the design are invariant to choice of technology. The barrel calorimeter will be installed and fixed within the magnetized iron used for muon identification, and it will provide the support for the solenoid coil and the tracking detectors. The endcap calorimeters will be moveable longitudinally to provide access to the tracking detectors and electronics. Access to the back of the barrel calorimeter will be incorporated into the design of the muon detectors.

We describe below five different technologies for sampling calorimeters that possess the above features: scintillating tiles with waveshifting bar readout; scintillating tiles with waveshifting fiber readout; scintillating fibers ("spaghetti") embedded in the absorber; liquid argon ionization calorimetry; and warm liquid ionization calorimetry. All five include absorber plates for which lead is a possible candidate. The order in which these choices are described is chosen only to facilitate the discussion.

Considering the stringency and importance of the practical requirements listed above, it is natural to consider whether the list of technologies might be shortened at this point. Indeed this question has been discussed intensively within the collaboration. Other factors being equal, it seems evident that the better established technologies would be more likely to be able to satisfy the practical requirements. However, this judgment is clouded by the fact that even the relatively well established calorimeter technologies, *i.e.* liquid argon

calorimetry or scintillating tiles with waveshifting bar readout, have never been used in 4π geometries with particle fluxes approaching those expected at the SSC. To clarify this issue we give highest priority in the calorimeter R&D program (section 4.3.5) to two problems that relate directly to the high particle flux: demonstration of the survivability of plastic scintillator calorimetry in the radiation field, and demonstration of a reliable, triggerable, and economical electronic readout for liquid ionization calorimetry with the necessary speed and low noise to satisfy performance requirement *(d)*.

We turn now to brief descriptions of the candidate technologies.

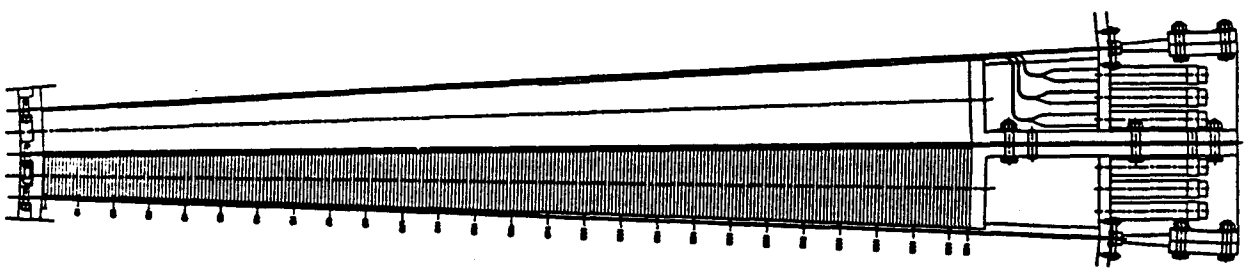

FIG. 18. Scintillating tile calorimeter tower with waveshifting bar readout.

Scintillating tile calorimeter with waveshifting bar readout

This calorimeter design is based on the conventional technology of interspersed scintillator and absorber plates with wavelength shifting bars used to transport the light to the rear for photomultiplier tube (PMT) readout. A preliminary design (Fig. 18) envisages a barrel calorimeter consisting of 128 wedges evenly distributed in azimuth with absorber plates normal to the particle direction. The modules are supported by an iron structure that also returns part of the solenoid flux, thereby shielding the PMT's. The endcaps are composed of similar wedges. Each wedge contains two rows of towers supported by the back beam, a center plate, thin side skins and the front plate of the calorimeter. The towers in both regions are of constant size (11×11 cm^2 at the inner surface) and are pseudo-projective, *i.e.* the electromagnetic calorimeter is tilted at a small angle in ϕ to avoid channeling effects in the waveshifting plates. The current design calls for photomultiplier readout on one side of a module in three depth segments. Uniformity as a function of depth and impact point is improved by using graded reflectors covering the scintillator and waveshifting plates. The absorber could be a Pb/Fe mixture or depleted uranium.

The combined system has a volume of approximately 600 m^3 and contains approximately 40,000 high precision PMT channels for the calorimeter measurement. This is a well known technology with fast readout and excellent energy resolution (albeit depending on the choice of absorber material).

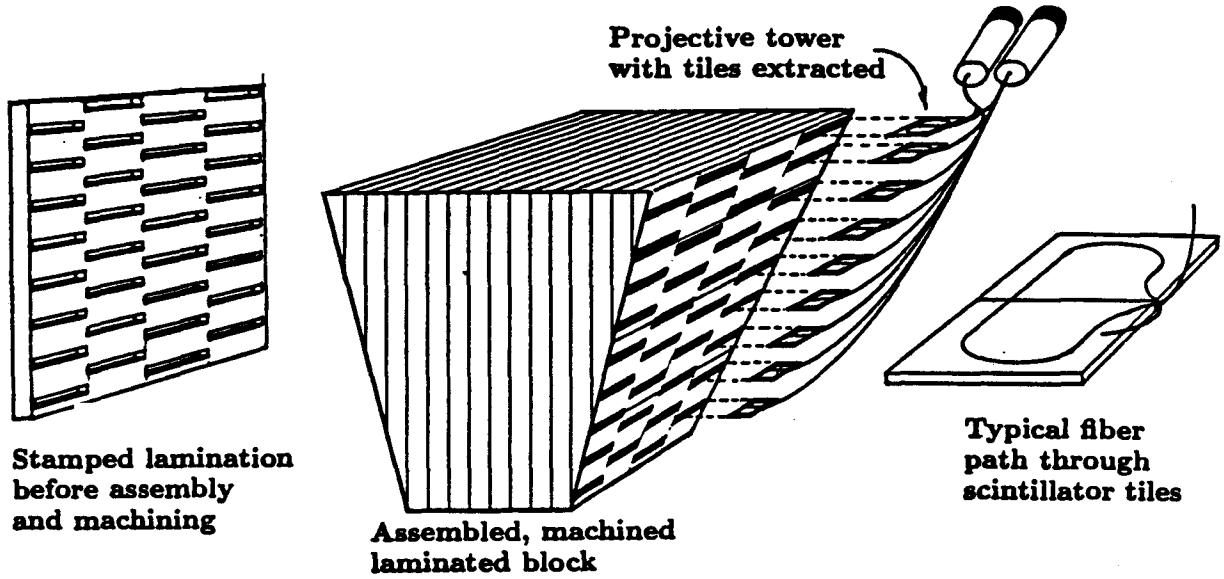

FIG. 19. Scintillating tile calorimeter with waveshifting fiber readout. The basic unit, which contains several towers, is assembled from stamped laminations, then machined. The slits accomodate lead sheets and scintillator plates.

Scintillating tile calorimeter with waveshifting fiber readout

A related calorimeter design shown in Fig. 19 uses waveshifting fibers rather than bars to carry the scintillation light to PMT's at the rear. Clad optical fibers containing wavelength shifter are embedded into the scintillating plastic plates ("tiles"). The pattern with which the fibers are embedded can allow a high degree of spatial uniformity. Near the tiles the waveshifting fibers are bonded to clear optical readout fibers that are led along narrow non-projective cracks to the PMT's. The flexibility and small size of the readout fibers permit small cracks and simplify the PMT shielding.

Despite its logical similarity to waveshifting bar readout, this technique can be implemented with a mechanical structure that is quite different. The mechanical modularity may be independent of the optical segmentation, so that a single mechanical module can include many towers with arbitrary longitudinal segmentation. The intimate coupling of fibers and plates yields more light, thereby allowing thinner tiles than would otherwise be practical. In turn this permits the design of a calorimeter with iron or a combined Pb/Fe absorber that should exhibit a level of compensation similar to that which could be obtained with lead using thicker tiles. Use of iron absorber lends additional mechanical strength to the modules, allows naturally for PMT shielding, and reduces system cost. Performance advantages of iron hadron calorimetry include low neutron dose in the central tracking region, fast approach to the asymptotic e/π ratio, and increased flexibility in configuring the magnetized iron used for muon analysis.

Members of both of the scintillating tile option R&D efforts described above are collaborating on prototype work, radiation damage studies, and engineering design being performed by the Westinghouse Science and Technology Center.

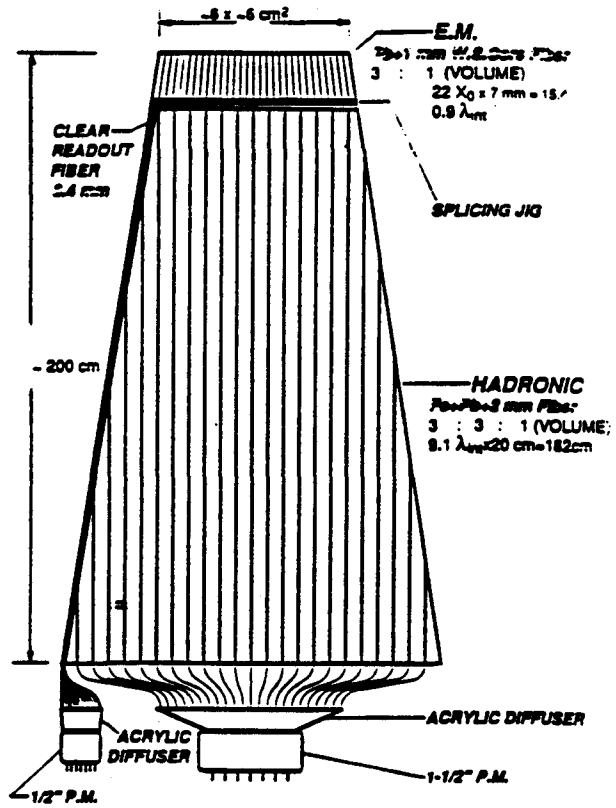

FIG. 20. Calorimeter tower with scintillating fibers ("spaghetti") embedded in the absorber.

Calorimeter with scintillating fibers ("spaghetti") embedded in the absorber

The fiber calorimeter consists of scintillating fibers embedded in an absorber matrix. Fibers, typically 1 mm diameter, run along the axis of the tower. The absorber can consist of lead, iron, or a lead-iron lamination chosen to ensure the required performance (excellent energy resolution, compensation), and mechanical and magnetic properties (magnetic flux return, shielding of the photomultiplier tubes). Self-supporting projective towers, 2 m deep, may be cantilevered with no structural members penetrating the electromagnetic section of the calorimeter. The longitudinal fiber geometry minimizes the path of light through the electromagnetic shower maximum region, thereby reducing potential problems arising from the radiation damage of plastic scintillators. Depth segmentation, important for the electron identification, can be achieved by exploiting the projective nature of the towers and separate read-out of fibers starting in the hadronic volume of the calorimeter. Other possible schemes may involve different color fibers in the electromagnetic and hadronic sections or an explicit depth segmentation with light transported to the back of the detector in a greatly reduced volume using wave-length shifter core fibers, for example as shown in Fig. 20. At the back of the calorimeter, fibers are bundled onto the photomultiplier tubes. This technique has no intrinsic limitations on the transverse granularity of the detector. If needed, a precise measurement of the electromagnetic shower position can be accomplished by bundling fibers from small "pixels," typically 2 cm × 2 cm, onto the separate fields of a multianode PMT.

Initial proof-of-principle for spaghetti calorimetry has been established by the SPACAL collaboration at CERN. For lead-scintillator in the ratio 4:1, an EM resolution of $13\%/\sqrt{E\,(\mathrm{GeV})}$ was achieved with a constant term of 1%. Pion rejection of 1:100 was achieved within an 80 ns gate using only the transverse segmentation of the calorimeter.

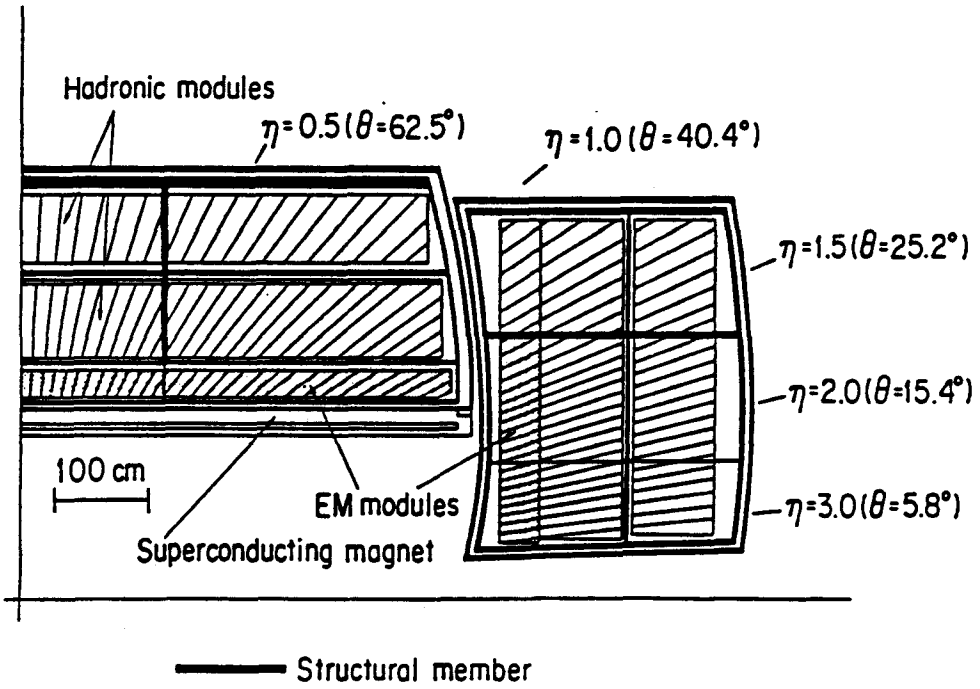

FIG. 21. Preliminary design for a liquid argon calorimeter.

Liquid argon ionization calorimetry

The present conceptual design using this well established technology is composed of modules contained in three cryostats. (This concept is directed toward the short rather than long coil option.) The layout is shown in Fig. 21. Either lead, a Pb/Fe mixture, or depleted uranium could be used as the absorber plate material. The volume is segmented into quasi-projective towers using absorber plates, connected by resistive bridges, as readout pads.

The choice of both calorimeter segmentation and preamplifier location depend strongly on detailed optimization of noise performance and readout speed. For fixed source capacitance, the signal to noise ratio is proportional to $\tau^{3/2}$ where τ is the charge integration time. The match between source and preamplifier capacitance can be improved by increasing the total preamplifier power and/or by transforming the source impedance. This transformation can be accomplished with ferrite cores or by connecting the plates in series ("electrostatic transformer"). If ferrite transformers are used within the stray field of the coil they must be magnetically shielded. Also critical is the cable length between readout pads and preamplifiers, as it controls the charge transfer time. Minimizing this length raises the possibility of locating the preamplifiers within the cold volume, with attendant issues of reliability and radiation flux.

As emphasized earlier in this section, demonstration of a reliable, triggerable, and economical electronic readout for liquid ionization calorimetry is one of our two highest priority calorimeter R&D problems. Particular emphasis is needed on solutions that are magnetic field tolerant.

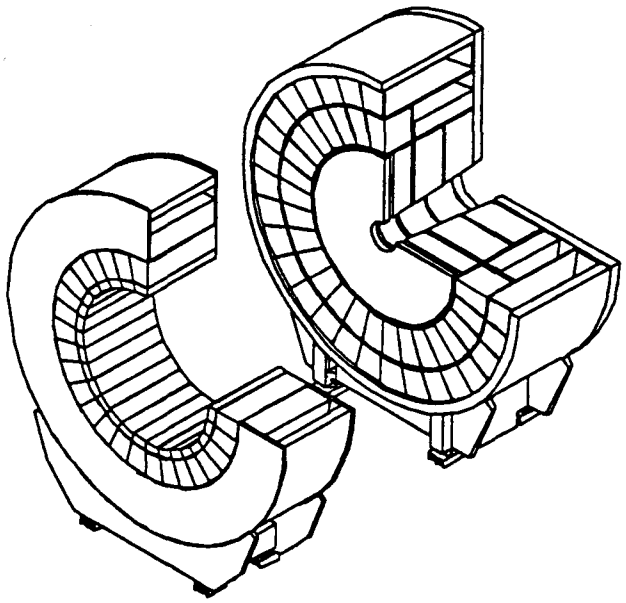

FIG. 22. An endcap and one central bay of the warm liquid calorimeter

Warm liquid ionization calorimetry

The use of liquids that have excellent electron mobility near room temperatures is an attractive variation of the ionization chamber calorimeter concept embodied in the liquid argon device. Positive features of the warm liquid approach are the possibility of compensation, the likely stability of calibration, and the promise of good hermeticity using pre-assembled modules of manageable size. The major challenges of this technology are in the choice of materials and the development of purification systems to establish low contamination levels ($\lesssim 10^{-7}$ oxygen equivalent) in the liquid. In addition, by appropriate choice of liquid and/or increase of drift field, adequate speed of response must be demonstrated. This is a very new technology and there has been almost no experience with large systems. Therefore "proof-of-principle" must be demonstrated by testing a model that includes the essential features of a realistic prototype and is large enough to contain a hadron shower.

A possible layout of a warm liquid calorimeter is shown in Fig. 22. "Swimming-pool" modules of $\lesssim$ 20 tons each are arranged in three "bays" in the barrel calorimeter and one bay in each endcap. An engineering study indicates that the mechanical stresses are within limits and the calculated hermeticity is good. This design uses an electrostatic transformer configuration in the hadronic section to reduce the source capacitance.

Pre-shower and EM shower-maximum detectors

Should it be required in any of these calorimeter designs, additional electron identification capability could be provided by a preradiator and detector ("pre-shower detector") mounted on the inside of the calorimeter barrel. This is a particularly attractive option for the "spaghetti" calorimeter if it is not longitudinally segmented. In the two scintillating tile calorimeters it would also be possible to mount a fine-grained position detector near EM shower maximum. Reading out a fine-grained scintillating detector would be particularly straightforward in the waveshifting fiber design. For the spaghetti calorimeter with red/blue light, it would be possible to use a multicathode (red) PMT for resolving the EM shower position. In the liquid ionization calorimeters, fine segmentation near EM shower maximum could be achieved at the expense of increasing the electronics channel count.

4.3.4. Forward ($|\eta| > 3$) system

Because of the limit imposed by transverse shower size the segmentation in the far forward region is quite coarse compared to the central region, remaining about 10×10 cm^2 in physical size. The primary requirements of the device located in this position are that it survive the radiation exposure and that it provide hermetic coverage to $|\eta| = 5$.

Several technologies are possible for the far forward calorimeter. Among them are liquid scintillator with conventional or fiber readout, and liquid ionization. Of these technologies liquid argon appears to be most radiation hard but may require a relatively thick wall at $|\eta| = 5$. In this region, signals corresponding to significant $\not{E}_t$ are large enough that issues of scintillation light output or preamplifier noise are much less important than in the central region.

A straightforward location for the far forward calorimeter would be as far as possible from the interaction point. There its radiation resistance would be optimized and the effect of its inert walls (if any) would be minimized. However, in that location albedo from its front face and from the exposed hole in the endcap calorimeter would be present. That albedo could interfere with the intermediate muon chambers and, if it crossed the beam line, bias the measurement of $\not{E}_t$. These problems would be reduced if the far forward calorimeter were placed inside the hole in the endcap calorimeter. However, albedo from its front face in that location would have a much larger effect on the tracking detectors. The issue of its location obviously depends to some extent on the choice of central calorimeter technology and remains under study.

4.3.5. Configuration of the present R&D program

Members of the collaboration are major participants in the relevant subsystem R&D proposals. To obtain the necessary information within the overall schedule, some of these R&D projects will need to be further strengthened and accelerated. As noted in the introduction to the discussion of candidate technologies, we assign highest priority to the two problems that relate directly to the high particle flux: demonstration of the survivability of plastic scintillator calorimetry in the radiation field, and demonstration of

a reliable, triggerable, and economical electronic readout for liquid ionization calorimetry with the required speed and low noise.

Turning to the R&D that is critical to each calorimeter technology, in the following we distinguish between the "critical" issues on which the viability of the technology depends, and those "engineering" issues that are also important but (it is hoped) can be addressed satisfactorily within the scope of a detailed design.

Critical issue for all scintillator technologies

The paramount concern is the radiation resistance of the scintillators, wavelength shifters, and other optical elements. Even small degradations will affect the constant term in the resolution, although this may be tracked to some degree with appropriate calibration techniques. If it is necessary (and possible) to replace damaged material periodically, operating costs may become unacceptable.

The vigorous R&D program being pursued to develop radiation resistant plastic is typified by that done by Bicron Co., Fermilab, Kyowa Gas Co., Tsukuba U., Florida State U., and U. of Illinois. Preliminary results indicate that with currently available scintillating materials, calorimeters can be constructed that would survive a total dose up to 10 Mrad without major degradation of performance[33]. However, these results are based on tests of samples of new scintillators, and beam tests are required to verify these results.

Critical issue for all liquid ionization detectors

Of utmost importance is the development of a fast electronic readout. The requirements of the readout are challenging to reconcile: it must be fast and quiet enough that neither noise nor pileup unacceptably impair the isolation criterion for electron triggering; it must be insensitive to magnetic fields; it must have the required dynamic range; and it must be reliable and/or accessible. The warm liquid and liquid argon SSC R&D collaborations are both addressing these problems, and there will be significant results from prototypes by spring 1991.

Engineering issues for all scintillator technologies

(*a*) Provision in the mechanical design for adequate magnetic shielding of photomultiplier tubes (or other readout devices). In general this problem becomes less difficult as the cross-sectional area of the optical path decreases, *i.e.* for waveshifting fiber readout. Other important factors are the choice of solenoid geometry and the location of the flux return iron.

(*b*) Achieving adequate uniformity of response across the tower cross-section, in the regions between towers, longitudinally along the towers, and across the junctions between modules and other dead regions. For various scintillator technologies this problem takes different forms. The problem of cracks should be most important for the waveshifting bar case.

(*c*) Understanding the method, effectiveness, and cost of calibration, particularly for scintillating fiber calorimetry.

Engineering issues for all liquid ionization technologies

(*a*) Meeting SSCL safety requirements and understanding the associated costs. These are major concerns both for liquid argon (oxygen deficiency hazard) and warm liquid (flammability for TMP and TMS). In particular, the effects of safety engineering on the geometry and thickness of vessel walls must be understood for both technologies.

(*b*) Achieving adequate uniformity of response at the interfaces between vessels. This is a particular worry for liquid argon with its double-walled cryostats. A related problem is the effect of vessel walls on the total material upstream of the active region, particularly near the barrel-endcap interface. Excessive material impairs the quality of electron identification.

Critical issues for newer technologies

(*a*) Demonstrating "proof-of-principle". This is imperative for warm liquid calorimetry, is required to a lesser extent (in light of test beam progress) for scintillating fiber calorimetry, and also is needed for waveshifting fiber calorimetry to the extent that the joined-fiber-readout technique has not been used on a large scale. Conceptual engineering designs of a 4π calorimeter, including necessary supports and services, are required for the scintillating fiber and waveshifting fiber options. Much better understanding of costs is needed particularly for warm liquid and scintillating fiber.

(*b*) For warm liquid, achieving and maintaining the liquid purity. This is an issue of cost and of avoidance of catastrophic failure.

Some other issues

(*a*) Electron identification for the scintillating fiber calorimeter without longitudinal segmentation. Another question concerns possible "oversampling" of leakage particles by the bundle of fiber scintillators at the rear of the tower.

(*b*) For liquid argon, the effect on the constant resolution term from the deviation of e/h from unity.

Engineering issues in common to all technologies

Issues shared by all technologies are: access to the tracker, calorimeter, calorimeter electronics, etc.; penetrations for cables and services to the tracker, calorimeter, and coil; coil and tracking detector supports; and requirements imposed by the trigger on signal pathways. It is essential to formulate a realistic construction and installation schedule.The engineering issues will be addressed by work at KEK, LBL, ANL, FNAL and the Westinghouse Science and Technology Center.

4.4. Electron identification

To obtain a good overall acceptance for processes in which particles decay to leptons, both electrons and muons must be identified and measured with good efficiency. Many techniques for identifying electrons exist (Čerenkov counters,transition radiation detectors, pre-shower detectors, and electromagnetic calorimeters). These have been exploited in UA1, UA2, CDF, D0, and other modern detectors. UA2 and CDF have been very successful in exploiting the unique signature of an electromagnetic shower in a calorimeter for the identification of electrons, and this approach, by virtue of its proven effectiveness and compactness, has been chosen for the SDC detector.

Parametrizing the needed calorimeter performance is complex: one must specify what is to be rejected (pions or jets); the degree of isolation; the level of tracking information available (minimal for the Level 1 trigger, extensive offline); and the backgrounds to the physics processes being studied. Some requirements are clear now. For example, in the Level 1 trigger the rate of isolated $\pi^{\pm}$'s misidentified as $e^{\pm}$'s by the calorimeter should be less than the rate of photon conversions in material upstream of track detectors that can contribute to that trigger.

Our detector system for electron identification and measurement will include some or all of the following:

(*a*) A high precision central tracking system embedded in a magnetic field providing measurement of the track momentum and event vertex;

(*b*) A pre-shower detector located after the coil and in front of the calorimeter providing shower position and pulseheight information;

(*c*) A finely-segmented shower detector after approximately six radiation lengths providing the shower position to within a few mm, a measurement of the lateral shape of the shower and relatively coarse shower pulseheight;

(*d*) A transversely and longitudinally segmented calorimeter providing at least two depth measurements and a relatively coarse shower position. Alternatively, the shower detector in (*c*) may be replaced by at least one layer in the calorimeter that is finely segmented in depth;

(*e*) Transition radiation detection in part of the wire chamber outer tracking system.

Information from these systems is combined to identify electrons and measure their energies. The different systems provide redundancy and efficiency. Electrons and positrons from photon conversions in the material in the inner tracking volume are a background for the prompt electron signal. It is essential, therefore, that the tracking system also be capable of reconstructing these with high efficiency. This background, however, provides a useful *in situ* calibration for electron identification. The system parameters (precision, granularity and resolution) must be optimised for the SSC environment and are not finalized. Current studies (based on the UA2 experience and CDF test beam studies) indicate that the pre-shower detector should come after approximately two radiation lengths. The detector near shower maximum is anticipated to be similar in effectiveness

to the one used in CDF. However, the type of detector used near shower maximum depends upon the type of calorimetry and has not been finally identified. For scintillator plate calorimetry, a number of options exist (silicon, or additional scintillator) for shower width measurements. Radiation resistance will be an important design criterion. For liquid ionization calorimetry, finer segmentation is possible but obviously requires additional electronics. The tradeoff between longitudinal segmentation and detector granularity near shower maximum needs more study. Similarly the nature of the preradiator has not been specified. Options include wire chambers and scintillating fibers.

4.5. MUON SYSTEM

The identification and measurement of muons is a critical goal for the SDC detector. Since muons can penetrate large amounts of material without significant energy loss, they are identified in the relatively low-rate environment exterior to the detector. For the SDC detector, the nature of the muon system is different in the central and intermediate-angle regions. In the central region ($|\eta| < 1.5$), precision measurement of muon momentum is provided primarily by the central tracker. The central muon system, outside the calorimetry, provides muon identification, a simple trigger, and a link to the central tracker. It also augments the central tracker in determining the momenta of muons with $p_t > 500$ GeV/c. At intermediate angles ($|\eta| > 1.5$), the performance of the central tracker degrades, and the intermediate-angle muon system must provide a precise momentum measurement as well as muon identification and a trigger.

The physics to be addressed by the SDC requires determination of muon transverse momenta at the trigger level. For $p_t \gtrsim 100$ GeV/c and $\mathcal{L} = 10^{33}$ cm^{-2}s^{-1}, the single muon trigger rate is less than 1 Hz. For lower muon p_t, single muon triggers would occur at a higher rate, reaching several kHz at 10 GeV/c. These lower p_t muons are used to form triggers involving information from other parts of the detector. Hence, a fast estimate of the p_t is required at the trigger level to tag muon candidates.

4.5.1. Central muon system

The central muon system covers the region $|\eta| \leq 1.5$. Muon identification and triggering are achieved by detecting charged particles deflected by a 1.5 m thick magnetized iron toroid ($B \approx 1.8$ T) located outside of the calorimeter. The central muon system is shown in Figs. 3–4. Scintillators and wire drift modules are used to find candidate muon tracks and estimate their p_t to a precision of about 20% for $p_t \lesssim 200$ GeV/c. Later in the triggering sequence, the muon system information is combined with information from the central tracker to give a refined p_t trigger.

The first level trigger uses both the scintillators and the wire drift modules. A coincidence matrix formed from two layers of scintillators outside of the iron toroid and one layer inside the toroid requires that a candidate muon track project back to near the interaction point in the z direction. Even at a luminosity of 10^{34} cm^{-2}s^{-1}, the charged particle rate in the outer region of the central muon system is less than 100 kHz. The

geometry of the scintillation counters is such that a muon from the interaction region with p_t greater than a fixed threshold, at this time taken to be 10 GeV/c, and originating from the interaction region, produces a trigger. These scintillators vary in width, with the smallest being 10 cm wide at 90°. The maximum length of each counter is 4 m and each has a phototube at each end. The scintillator trigger distinguishes between bunch crossings and reduces the muon candidate rate to about 1 kHz.

There are four vector drift modules, each module having eight layers of wires, four measuring in the bend direction and four in the orthogonal direction. The overall resolution for each module is expected to be about 250 μm in the bend direction, dominated by the alignment accuracy of the module. Two separated modules are located inside the iron toroid, and two outside. Employing the bunch crossing determined by the scintillator trigger, the first level muon trigger uses the four modules to measure the muon momentum. Occupancies are low enough that the segmentation of these modules is determined by the desired maximum drift time which, in turn, depends on the length of the electronic pipeline for the detector. At present, we assume that a maximum 5 cm (1μs) drift will be sufficient. The wires will be no longer than 9 m and will be supported at intervals to maintain alignment.

The second and third level triggers combine information from the scintillator and drift modules with information from the central tracking and calorimetry to find and measure muon track candidates in three dimensions and determine their degree of isolation.

4.5.2. Intermediate-angle muon system

There are two possible designs for the intermediate-angle muon system. One uses superconducting air-core toroids, and the other uses conventional iron toroids, as have been used by CDF and D0. Air-core superconducting toroids would be a better match to the momentum resolution of the central muon system because of lower multiple-Coulomb scattering. They also would allow more readily the precision alignment of the detector elements using charged particle tracks. Preliminary engineering studies of the air-core toroids required for the SDC detector are encouraging but more studies are needed. In the remainder of this section we describe the system with superconducting toroids.

The intermediate-angle muon detector covers the region $1.5 < |\eta| < 2.5$. It provides not only a muon trigger, but also an off-line muon momentum measurement comparable to that of the central region, as shown in Fig. 23. This system consists of a large air-core superconducting toroid sandwiched between two sets of drift modules arranged in octagonal geometry (see Fig. 3). Two planes of trigger counters are located outside the outer drift plane.

As in the central system, the first stage of the trigger is an appropriate coincidence between the two planes of trigger counters, which are segmented radially to give an approximately constant acceptance in pseudorapidity. For a p_t threshold of 10 GeV/c the upstream counter width at the inner radius is 2 cm and increases to 16 cm at the outer radius. A coincidence reduces the single muon trigger rate to 10 kHz (at $\mathcal{L} = 10^{33}$ cm^{-2}s^{-1}).

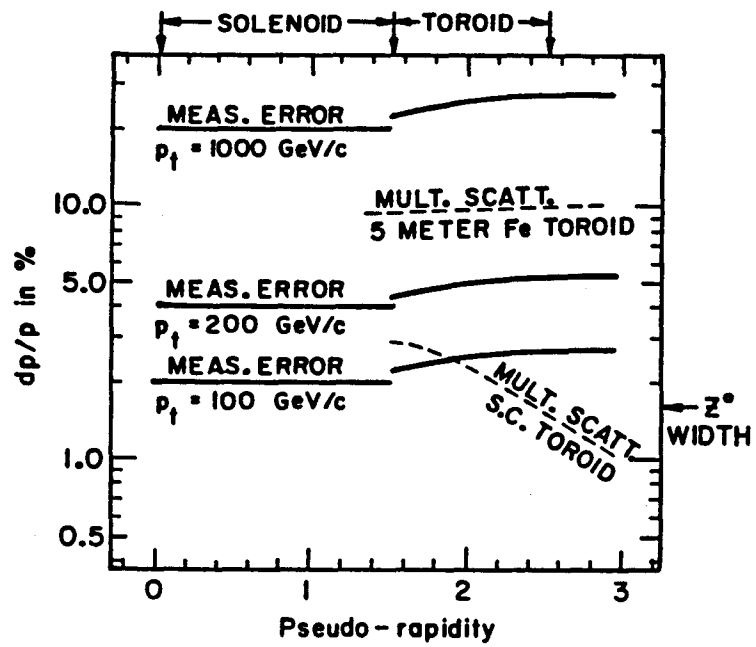

FIG. 23. Comparison of the muon momentum resolution from the central tracker with that of the intermediate-angle superconducting air-core toroid system. The solid lines show the resolutions $\delta p_t/p_t^2 = 0.2\ (\mathrm{TeV}/c)^{-1}$ for the central tracker and $0.25\ (\mathrm{TeV}/c)^{-1}\ \cos\theta$ for the air-core toroids. The dashed lines show multiple-scattering contributions to the resolution of an air-core toroid and an intermediate-angle toroid of magnetized iron. Also shown is the resolution required to reconstruct the $Z(\rightarrow \mu\mu)$ mass with an error equal to the natural width of the Z.

We are currently studying, both by beam tests and simulations, the environment in which these counters must function. Čerenkov counters are an alternative that might be used if the combined rate of low energy charged particles and neutron-induced hits is too high.

The design of the drift modules of the intermediate-angle muon system is driven by considerations of both triggering and momentum resolution. The offline reconstruction will need better resolution than does the trigger. Conversely, the need for a simple, fast trigger drives the design to an occupancy that is lower than necessary for offline analysis. To achieve an overall 100 μm resolution per module with an acceptable occupancy, six measurements with a 2.5 cm drift per measuring layer are made. There are two modules before and two after the toroid magnet. In order to resolve ambiguity for multi-track events, two 4-wire stereo modules have been incorporated. The overall channel count for the muon system is given in Table 7.

4.5.3. Superconducting toroids

We have investigated the design of superconducting air-core toroids with an inner radius of about 2.3 m and an outer radius of about 6 m. The magnetic field integral $\int Bdz$ is 8 T-m at the inner radius ($\eta = 2.5$) and decreases as $1/r$. Each toroid has a stored energy of about 280 MJ.

Two possible geometries are being considered for the superconducting coil. In the first, the winding is continuous in ϕ, forming a figure of revolution, as shown in Fig. 24. In the

Table 7

Muon system channel count.

	Central	Intermediate[a]
Drift wires	60k[b]	40k[c]
Scintillators	12k	2k

[a] Both ends.
[b] 4 wires/view, 2 views/module, 4 modules, 10 cm cells.
[c] 4 bend-plane modules with 6 wires/module, 2 stereo modules with 4 wires/module, 5 cm cells.

second, discrete coils are evenly spaced in ϕ (Fig. 25). In this case the coils would probably be modular, with little scattering material except near the coil planes and perhaps easier to fabricate and assemble into the toroidal configuration. A continuous coil would contain the toroidal magnetic flux better, resulting in a more uniform field in ϕ and less stringent magnetic shielding requirements for nearby detector elements.

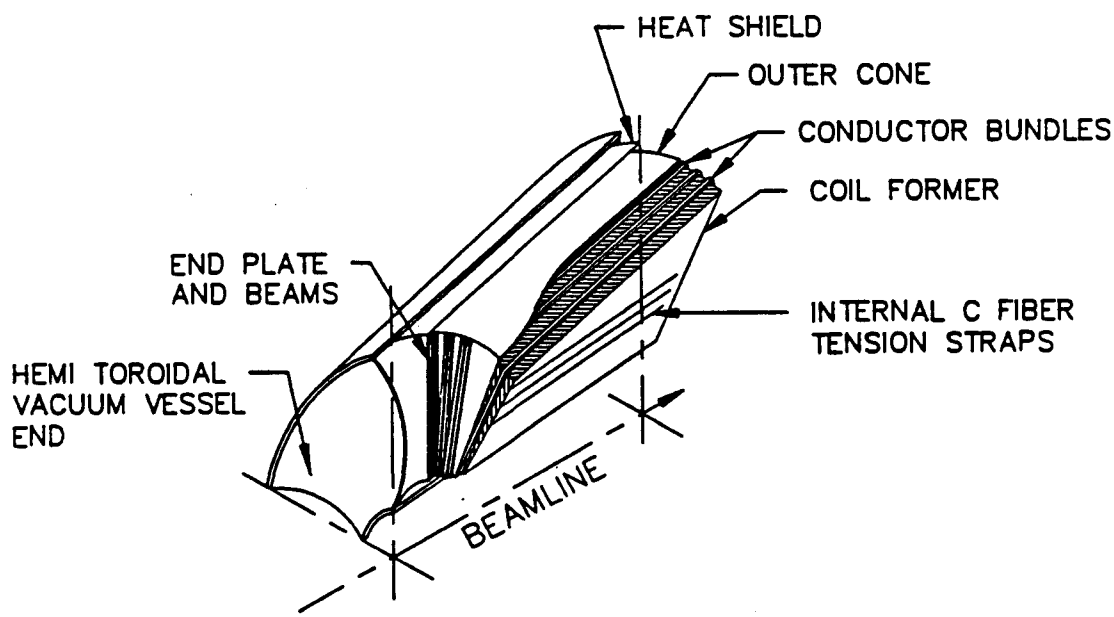

FIG. 24. Continuous winding air-core toroid, from a preliminary design (April 1990) by Advanced CryoMagnetics, Inc.

The design of these toroids has just begun. The engineering required to evaluate their feasibility is much greater than for the solenoid. This is because eight thin superconducting solenoids have been designed and built in the last few years, whereas toroids of the style desired for the intermediate-angle muon system do not exist. A very preliminary design for a superconducting toroid with a continuous coil has been made with the assistance of Advanced Cryomagnetics, Inc., and has been used as a basis for our preliminary cost estimate. We are requesting funds for a detailed exploration of toroid designs in preparation for the proposal next year.

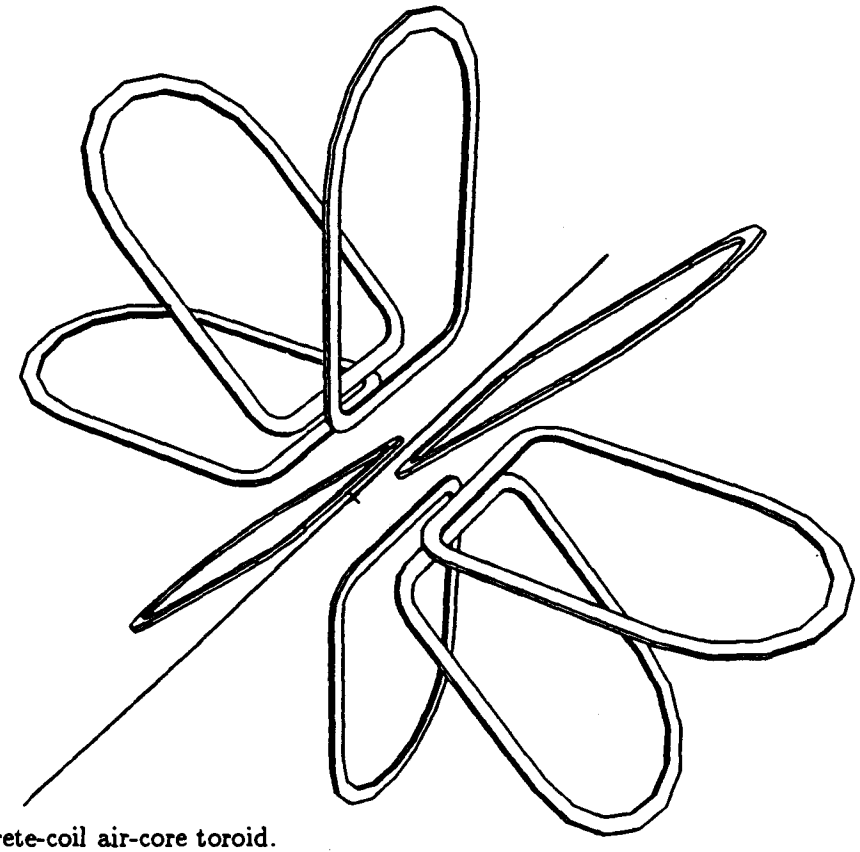

FIG. 25. Discrete-coil air-core toroid.

4.6. Electronics, trigger and data acquisition

The dataflow diagram for the SDC detector is shown in Fig. 26. The trigger and data acquisition systems have three levels. At the first level, all information about the event is preserved and a decision is made using a subset of the total information. The deadtime at the first level is negligible. The first level decision is made every 16 ns at a fixed time ($\leq 1.5\mu$s) after the interaction occurs. If a first level trigger decision is to accept the event, the data are moved or assigned to a buffer for the second level decision.

The second level decision is based on a larger subset of the event data than the first level. A substantial part of the data may still be stored in analog form at this point. The total processing time of the second level for an individual event may vary between 10 and 50 μs, and a decision is made every 10 μs. The combined rejection factor of the first and second levels is expected to be 10^5.

After an event is accepted at the second level, all information is digitized and read out. Full event data are required for the third level decision. The event rate into the third level trigger will be between 100 and 1000 Hz. The Level 3 trigger will be implemented as a processing farm that is designed to achieve a rejection factor of 100, with 10 to 100 event/s written to mass storage. The bandwidth of the data path to the third level farm is designed to accept up to 10k event/s.

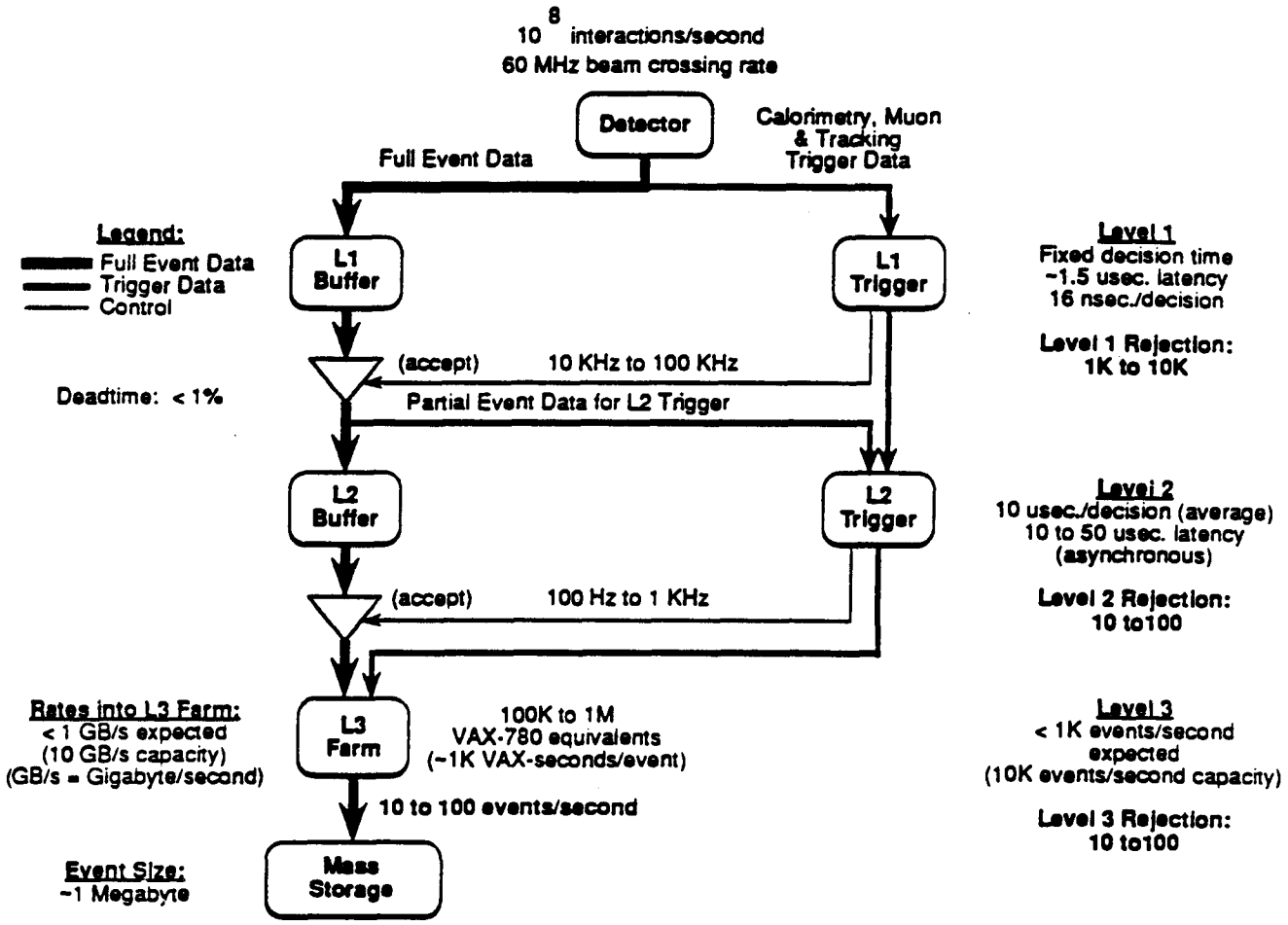

FIG. 26. Trigger and data acquisition dataflow for the SDC detector.

4.6.1. Electronics

For most of the proposed detector subsystems, including liquid ionization and scintillator calorimeters, wire chambers, silicon strip detectors, and muon chambers, the performance and basic characteristics of an individual channel of electronics are similar to those obtained in existing systems. However, the very large number of detector elements, the high interaction rate, and the environment pose a number of severe challenges. Foremost among these are: (*a*) reductions by factors of 10–100 in power dissipation; (*b*) adequate radiation hardness; (*c*) implementation of Level 1 (1–2 μs) and Level 2 (10–50 μs) buffering; (*d*) simultaneous signal processing and data readout; (*e*) greatly improved fault analysis capability; and (*f*) high reliability. Based on the broad program of electronics R&D currently underway, we are confident that the basic goals can be met if the most advanced integrated circuit, interconnect, and packaging technologies are utilized[34]. A large amount of R&D is still required to determine the optimal designs, to secure access to the best technologies, and to reduce the cost to an acceptable level.

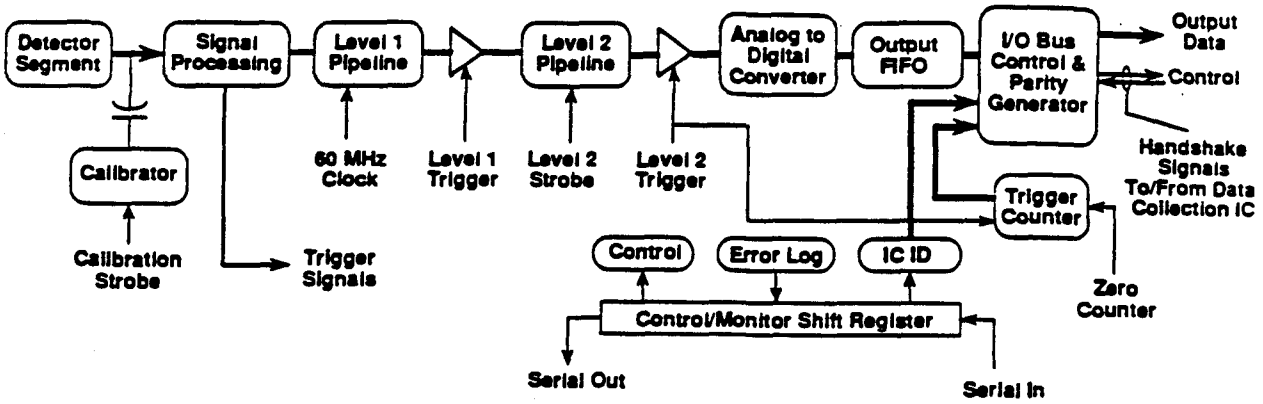

FIG. 27. Front-end electronics architecture.

A schematic outline of a possible architecture for the front-end signal processing and data acquisition system is shown in Fig. 27. We comment briefly on each of the elements.

(*a*) Signal processing: Preamplifiers are required for almost all systems. For liquid ionization calorimeters, for drift time and pad chamber readout of wire chambers, and for silicon strip, silicon drift, or silicon pixel detectors, the preamplifiers are optimized to either minimize noise or obtain minimum power dissipation at an acceptable noise level. For these systems some shaping or bandwidth limitation is required. For scintillator calorimeters using photomultipliers, for scintillating fibers in which only hit information is used, and for muon chambers in which higher gas gains are employed, the signal processing requirements are considerably less stringent.

(*b*) Level 1 storage: The data for each channel are stored for approximately 1.5 μs while the first level trigger is formed. Leading candidates for this storage are switched-capacitor analog memories and flash ADC's with digital storage. Acoustic charge transport delay lines are also being evaluated.

(*c*) Level 2 storage: To minimize the rate at which data must be moved off the detector, data associated with an event passing the Level 1 trigger are stored on front-end chips for an additional 10–50 μs while the Level 2 trigger decision is being formulated. This approach reduces the bandwidth required for the readout by approximately a factor of 100 compared to that required if no Level 2 storage were implemented.

(*d*) Interaction of front-end circuits with the trigger system: Given the assumptions that (1) the Level 1 trigger system is synchronous (62.5 MHz), and (2) the Level 2 trigger is asynchronous but monotonic (event number always increases), initial studies indicate that the interaction between the trigger system and the front-end circuits (Level 1 and Level 2 storage) can be accomplished with a small number of fast control signals.

(e) Interaction with Data Acquisition System: After the Level 2 trigger decision, analog to digital conversion is performed on-chip for many of the channels. Data collection chips assemble data locally from a number of the front-end chips and prepare it for transmission over fiber optics.

We comment briefly on the nature of the specific electronics for a number of the most important systems.

Silicon strip and pixel detectors:

There are three different efforts underway to develop circuits for the readout of silicon strip detectors of more or less conventional design, *i.e.* strips of length 8–10 cm with doubled sided detectors. In two of these, the preamplifier, shaping amplifier (or simple post-amplifier), and comparator are implemented in a bipolar process while a CMOS circuit records which strips are hit for each crossing (no analog information being recorded). The third effort is the development of an all CMOS circuit which records the charge on each strip so that improved position resolution can be obtained for a given strip spacing.

The use of very short strips, *e.g.* about 1 cm in length, is being considered. Since the preamplifier power required to obtain a given signal/noise ratio decreases with the detector capacitance faster than linearly, a system with such strips may have the lowest total power dissipation even though the number of channels is much larger than with long strips.

The ultimate in position resolution and resistance to radiation damage is obtained with pixel detectors. The very small capacitance of the pixels, and the corresponding low occupancy, make possible readout circuitry consuming only tens of μW per pixel. Prototype circuits are under development for the options of (1) inclusion of the circuit directly on the high resistivity silicon of the detector and (2) manufacture of detector and electronics on separate silicon wafers.

Wire drift chambers:

The electronics for each channel in this system consist of a preamplifier, a fast shaping amplifier (with a shaping time of $\sim$ 5–10 ns), a pulse tail cancellation circuit, a discriminator, and a time-measurement system. It is anticipated that the first four elements will be implemented in a bipolar technology. Two independent R&D efforts have demonstrated that the required performance can be obtained with power dissipations of 5–15 mW/channel. Implementation of the circuits in processes that are truly "radiation hard" will be carried out in the next eighteen months.

Two independent versions of the time measurement system, including Level 1 and Level 2 storage and control logic for readout, are also under development. Both systems have demonstrated a time resolution of less than 1 ns with 0.5 ns very likely being obtainable.

Scintillating fiber tracking:

The two leading candidates for the readout of scintillating fiber tracking detectors are avalanche photodiodes and the "solid state photomultipliers" developed by Rockwell.

The former have the advantage that gains of order 10^4 have already been demonstrated. Their primary challenge is that they must be operated at 7 °K. Work is underway with Rockwell to obtain devices with risetimes of less than 10 ns (a few tens of ns having already been achieved). Readout of avalanche photodiodes can be performed at or above liquid nitrogen temperature. Commercial modules exist which meet the quantum efficiency and time resolution required but need to be reduced in cost.

A general advantage of scintillating fibers is that the electronics can be located away from the tracking volume. The output of each fiber is a single bit per crossing.

Calorimeters:

Systems of electronics are being designed for scintillator and liquid ionization calorimeters. Radiation-hard JFET preamplifiers allow location of the preamplifier inside the liquid ionization calorimeter volume for optimal speed and noise performance. Bipolar preamplifiers are also being developed and might be used either for scintillator calorimeters or for liquid ionization calorimeters in locations where the magnetic field prevents the use of transformer coupling. Following the preamplifier, a shaping amplifier is used for bandwidth limitation. The shaping time can easily be adjusted to be consistent with the fastest scintillator or to be somewhat slower to allow improved signal to noise for liquid ionization detectors. The output of the shaping amplifier is sampled at 16 ns intervals. Currently it appears that analog sampling can economically provide sufficient dynamic range. It is an open question at this point whether the Level 2 storage should be analog or digital.

Research is also underway on pipelined phototube digitization circuits, which are being built for testing with scintillator calorimeter prototypes in the 1990-91 test beam runs at Fermilab. The circuits use a multi-range gated integrator application-specific integrated circuit (ASIC) in conjunction with a commercial FADC to digitize the charge from the phototube each crossing, with 8-9 bit accuracy and 20-bit dynamic range. The output will drive an all-digital pipelined DAQ/trigger ASIC.

Muon detectors:

It is anticipated that the electronics for readout of the muon chambers can be adapted in a reasonably straightforward fashion from that developed for the other wire tracking systems. The major difference is the longer drift time. However, in even the largest cells, the drift time is to be no longer than the Level 1 decision time (1–2 μs).

4.6.2. Trigger

The selection of interesting events is performed by the trigger system. The trigger system must identify with high efficiency the signatures of known and expected processes, and be sufficiently flexible to capture events with new signatures. It must also reject almost all of the enormous number of background events. The rejection factors are 1000 to 10000 for Level 1, 10 to 100 for Level 2, and 10 to 100 for Level 3, as shown in Fig. 35. The output to the permanent recording medium is 10 to 100 Hz.

Table 8[35] lists the Level 1 transverse energy thresholds for various processes corresponding to cross sections for these processes of 1 μb and 10 μb. These thresholds include the effect of pileup. A detector which is fast enough to resolve beam crossings (every 16 ns) sees an average pileup of 1.6 events, whereas a slower detector is subjected to correspondingly more pileup. Since there is a significant difference for the E_t threshold between a detector that can resolve individual crossings and a detector that integrates, for example, over three crossings, both of these thresholds are listed.

Table 8

Level 1 transverse energy thresholds for selected calorimeter and muon triggers, including effects of pileup, for both 1 μb and 10 μb cross sections (which yield individual rates of 1 and 10 kHz, respectively).

Trigger	Threshold (1 μb)	Threshold (10 μb)
Jet	190 GeV	100 GeV
Muon	15 GeV	10 GeV[a]
E_t (16 ns res.)	700 GeV	550 GeV
E_t (48 ns res.)	1100 GeV	900 GeV
Photon/electron	34 GeV	19 GeV
Two electrons	14 GeV	10 GeV
Two muons	10 GeV	10 GeV[a]
1 electron/1 muon	14 GeV/10 GeV	10 GeV/10 GeV[a]
$\not{E}_t$	140 GeV	75 GeV

[a]The muon system will not trigger below 10 GeV.

The Level 1 thresholds are low enough to accept events of interest using calorimeter and muon information only. The next step is to examine in detail the thresholds needed for Level 2 and Level 3. Preliminary results indicate that triggers using electrons and muons must incorporate p_t information from the tracking system in Level 2 and Level 3. While there are indications at this time that tracking information in Level 1 is not crucial, it is possible that a detailed design of the system may suggest the need for some tracking information in the first level trigger. It is intended that complete tracking information will be available at Level 3 to provide, for example, the full power of lepton-hadron separation.

In this context, the basic assumptions about the trigger are as follows:

(*a*) The trigger uses all the salient features of the detector.

(*b*) The signals from the calorimeter are sufficiently fast to permit the identification of energy deposition above a certain threshold with a specific bunch crossing, *i.e.* the timing resolution is better than 16 ns.

(*c*) The tracking and muon systems provide trigger information in a time less than the length of the Level 1 pipeline.

(*d*) The trigger functions comfortably at 10^{33} cm^{-2}s^{-1}. Since increases in luminosity do not shorten the time between crossings, the basic architecture of the trigger will not change.

(*e*) The output event rate is not more than 50% greater than the yield for an ideal trigger.

(*f*) The trigger associates stiff tracks with muons and calorimeter clusters.

(*g*) The trigger uses calorimeter tower thresholds to reduce the effects of minimum bias event pileup.

There are many trigger design issues that must be resolved on the time scale of the proposal submission. Many of these issues affect the design of other systems. The most obvious problems needing resolution are:

(*a*) Upon what quantities are the final trigger decisions based? Total E_t, missing E_t ($\not{E}_t$), electron and muon p_t are important. Isolation and invariant mass reconstruction need to be studied.

(*b*) Which subsystems supply information to the trigger? Information from tracking, muons, and calorimetry systems is needed. The case is less clear for preradiators or vertex systems. This is an important decision since the cables for the trigger will most likely dominate the cable plant.

(*c*) What degree of transverse and depth segmentation is required in the calorimeter trigger?

(*d*) What degree of precision is needed in the trigger? Crude momentum cuts from the tracking system are sufficient, but $\not{E}_t$ requires high precision energy sums over all of the calorimetry.

(*e*) How is the information from the detector stored while a trigger decision is being made?

(*f*) At what stage is the trigger information digitized? For example, while UA1 and ZEUS have large digital trigger systems, CDF and UA2 have large analog trigger systems. Both can be made to work.

(*g*) What kinds of pattern recognition are needed?

(*h*) How much dedicated circuitry in the form of custom chips can be placed on the detector? How much has to be accessible during collisions?

4.6.3. Data Acquisition

The detector requires a robust data acquisition system capable of handling data rates 2-3 orders of magnitude higher than the current generation of collider detectors. We list below some of the capabilities required of the data acquisition system.

(*a*) An average data rate of 1 Gbyte s^{-1} is expected for a combined Level 1 and 2 trigger rejection of 10^5. A data acquisition capacity of 10 Gbyte s^{-1} is required to provide

minimal deadtime and a substantial margin for increased luminosity and Level 1 and 2 trigger rates.

(*b*) Sophisticated event processing provided by a 10^5–10^6 VAX 780 equivalent processing farm and special purpose processors must achieve an additional factor of 10–100 reduction in trigger rate.

(*c*) The data acquisition architecture should be scalable from small-scale test beam and electronic systems tests to the full experiment. We anticipate installation of a large number of data acquisition systems for use in developing and testing detector systems and their associated electronics.

(*d*) An open architecture is required to provide easy upgrade paths and allow the incorporation of new technology to meet the evolving physics demands.

(*e*) Much of the data acquisition system is integrated with the detector systems and located in relatively inaccessible areas. The data acquisition system must have built-in redundancy, provision for fault detection, and a high degree of fault tolerance to allow continued operation under a wide variety of failure modes.

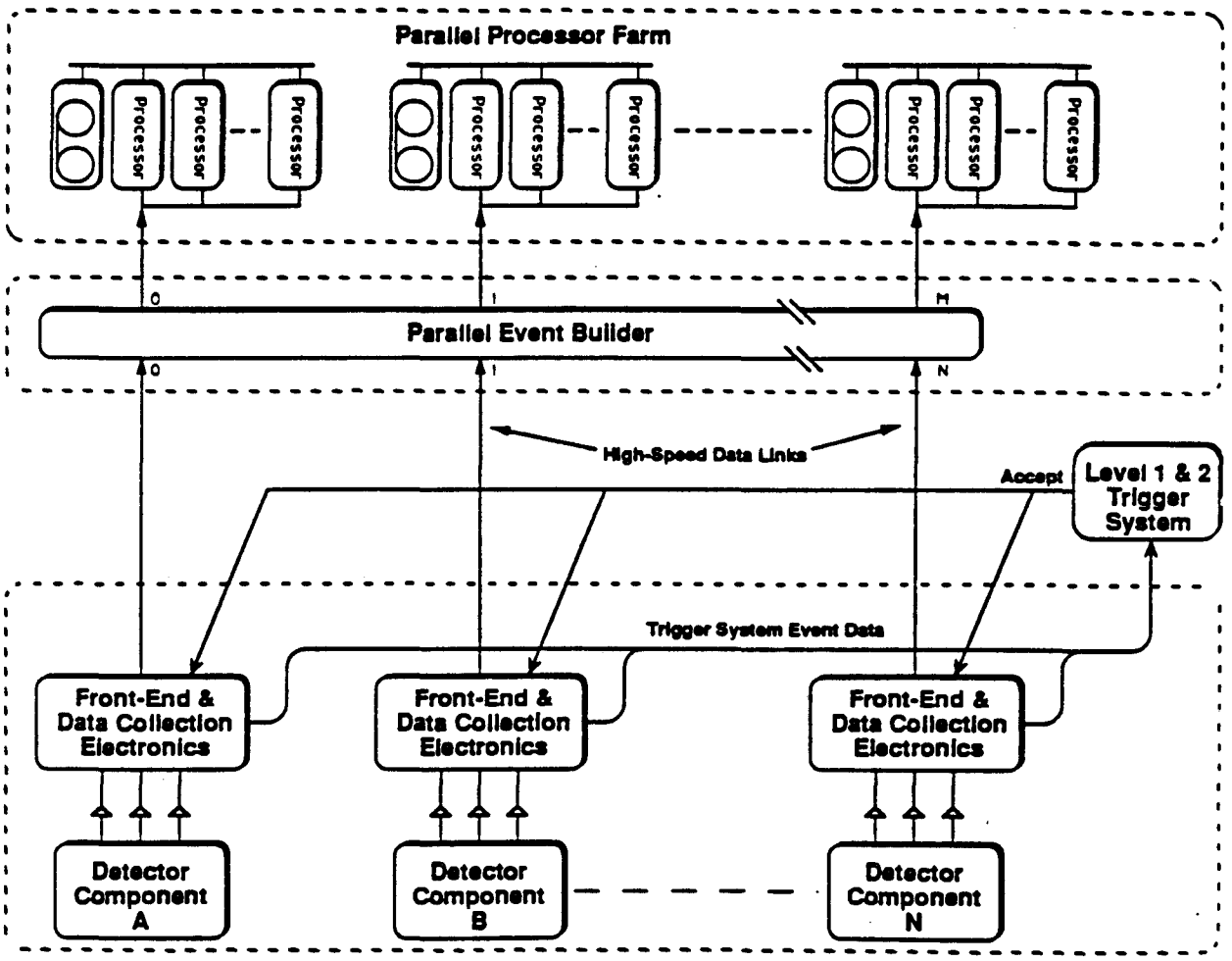

FIG. 28. Data acquisition architecture for the solenoidal detector.

The data acquisition architecture is shown in Fig. 28. Its essential features are:

(*a*) Data collection electronics to funnel data from front-end electronics into a moderate number of high speed data streams.

(*b*) High speed data links operating at bandwidths of at least 100 Mbyte s^{-1} to move data from the detector to the parallel event builder.

(*c*) A parallel event builder to assemble data from various detector elements into complete event records containing all data associated with a particular event. A moderate number of paths transmit the event records to the processor farm.

(*d*) Special function processing elements at various points along the data path to speed highly repetitive and/or parallel processing functions. These processing elements complement the general-purpose processing farm by using specialized processing elements such as neural network and digital signal processing chips.

(*e*) A parallel processor farm to apply sophisticated trigger filter algorithms, compress data, and perform final event selection.

(*f*) Industry-supported communication links to provide the data paths between the event builder, processor farm, and host computing facility.

(*g*) Computing facilities for permanently recording accepted events, for the user interface, and for monitoring detector operation.

(*h*) Simple control mechanisms to keep events flowing from the detector at high rates with little dead time.

(*i*) Networks for system initialization, downloading, calibration, and monitoring functions.

More complete descriptions of the data acquisition architecture are given in Refs. 36, 37, and 38.

4.6.4. Electronics, Trigger, and Data Acquisition R&D

A comprehensive research and development effort in the areas of electronics, trigger, and data acquisition is crucial to a timely completion of the detector. Trigger and data acquisition development have not been sufficiently funded by the subsystem R&D program, although they have a significant impact on the cost and design of the experiment. For example, the time needed to make a first level trigger decision is critical in determining the number of Level 1 buffers and has a significant impact on the cost and design of the electronics. The development of new methods for pattern recognition, such as neural networks, may offer the possibility of substantial cost savings over conventional methods. A variety of test beam and electronic system tests requires data acquisition systems at an early stage of the experiment.

The time scale for this effort is short. Design of the trigger must be concurrent with design of detector and electronics systems to ensure that the detector is capable of meeting the stringent requirements imposed by the trigger. Conceptual design of the

data acquisition system is to be completed in time for the proposal, with preproduction prototypes available for tests in 1994. Installation of large scale data acquisition and electronics systems into test beams will follow.

The list below includes R&D projects of high priority which have not been adequately supported under the subsystems R&D program. It is not a complete list of all R&D and conceptual design work that must be done by the time of the proposal. Other important projects will be identified as the investigations progress. Additional engineering support will be needed to complete conceptual designs for the proposal. This R&D effort is also essential to the understanding of electronics costs.

(*a*) Development of trigger algorithms and testing with simulations of signals and backgrounds. These studies impact the design of the detector components and define the requirements for the data acquisition and trigger systems.

(*b*) Studies of the problems of and techniques for triggering on muons, particularly for $|\eta| \gtrsim 1.5$.

(*c*) Studies of the importance of central tracking information in electron triggers. For instance, how accurately must tracks match showers in position and in momentum, and is z information needed? Is this information needed for Level 1?

(*d*) Development of custom IC's for track segment recognition for straw-tube and scintillating fiber tracking systems.

(*e*) Functional modelling of possible architectures for the overall trigger and data acquisition system. These studies are needed to assess the performance achievable with different architectures, including the interplay of trigger rejections and data bandwidths, and to understand the control mechanisms and reliability issues.

(*f*) Definition and modelling of the interface between front-end amplifier and buffer IC's, and the data acquisition and trigger systems. This first step in data collection is crucial to overall data acquisition performance. Timely study is necessary for the full specification of the custom front-end IC's and provides the opportunity to share technical solutions across detector subsystems.

(*g*) Development of a representative complete front-end system, including all the circuit infrastructure for control and readout and for detector mounting. This involves development of some custom IC's and much detailed design work. This prototype system is necessary to demonstrate the feasibility of the front-end architecture, including the operation of sensitive analog inputs in close proximity to digital readout circuits. It also identifies the complete functionality required of the family of custom front-end chips and will assist in accurate cost estimation.

(*h*) Development of specialized circuits for calorimetric triggers, including pattern recognition by neural nets or by other techniques and integrated circuits for sampling, summing, applying thresholds, and recognizing patterns among calorimeter trigger inputs.

(*i*) Studies of event building techniques, including functional modelling. The parallel event builder defines the manner in which the system scales. Studies are needed to understand the differences in performance and in functionality among the several possible solutions.

(*j*) Development of techniques for triggering on the basis of inner-layer tracking information and for triggering on secondary vertices. If feasible, such triggers may provide powerful tools for the efficient selection of important classes of events.

(*k*) Studies of the requirements for distributed processing placed upon the data acquisition and trigger systems by the detector components, and of the need for specialized processors in this role. Processing may be required to correct and reduce data, calibrate detector components, and extract local features of the events, such as jets or tracks. These studies relate closely to the details of detector component design and front-end electronics design. They must be carried out in conjunction with the modelling of global system architectures.

(*l*) Definition of the location of electronics on the detector, near the detector, and in counting houses, to understand cable plant and IR hall requirements, as well as power dissipation and radiation hardness needs for the electronics.

(*m*) Construction of a prototype data acquisition system. This project tests the novel features of an open scalable architecture which can exploit commercial developments and technological advances. It will be used for tests of prototype detector components, and serve as the basis for the eventual smooth integration of all detector subsystems.

4.7. Computing, software, and networking

The extremely fast pace of advances in computing hardware capabilities creates challenges for the design of the SDC's computing hardware, whose requirements must be specified during the initial detector design without freezing the implementation earlier than necessary. More powerful computing hardware allows more capable and complex software, compounding the difficulties that high-energy physics experiments have usually had in this area—extreme decentralization of code writing without the professional engineering accorded to the detector hardware. This lack of systematic design arises both because of the lack of mature standards and techniques for software engineering, and also because the easily modifiable nature of software leads to the belief that it can be rewritten if need be. However, with the large amount of software needed for a major detector (CDF has written over 10^6 lines of code), the effort required for major modifications becomes comparable to that needed to rebuild major hardware devices.

Software for the SDC detector will need to be engineered. Although the techniques of software engineering are still developing, the software industry already benefits extensively from their use. Within high-energy physics, the ALEPH and D0 detectors have made the most extensive (though still decidedly partial) use of software engineering techniques. We

plan to start with extensive interactions with industry and the academic side of computer science to survey the available techniques and make at least initial choices for the SDC.

The next section addresses the short-term computing needs of the collaboration. We will then outline our preliminary plans for long-term software development and management and present a preliminary summary of computing needs in the final section. We feel strongly that an emphasis should be placed on centralizing computing for the SDC at the SSCL, in order to promote coherent computer/software efforts in a timely manner.

4.7.1. Short-term needs

Substantial amounts of computing will be needed by the collaboration during the preparation of the proposal. Since the required resources do not exist at present at the collaborating institutions they will need to be provided by the SSC Laboratory, centrally at the SSCL and/or through funding to the collaboration. The resources required include computing cycles, mass storage for code and data, software support, workstations, and network access to computers and data. We include the requirements for other high speed communications such as videoconferencing here because some of the physical equipment is shared with data networking. By far the greatest need for computing for the proposal preparation comes from the extensive simulations of physics processes and detector responses that are needed for optimization of the detector design and documentation of its capabilities. The simulation work needed and the approach taken by the collaboration are discussed in section 5.4.

By October 1990, we estimate that our collaboration will be devoting 20 FTE physicists to the simulation effort for the design of the detector. We estimate that each FTE physicist on average will be producing samples of 10^4 signal events and 10^5 background events with a need for turnaround of the event sample within 6 weeks. The event sample will need to be buffered on disk and written to tertiary storage media, from which it will be analyzed several times. From current experience with existing GEANT simulations, we estimate a total generation and (repeated) analysis time of 5 MIPS minutes per event and a storage requirement of 250 kbytes per event. (We use MIPS as shorthand for the computing power of a VAX 11/780 computer, including both integer and floating point performance.) Thus, within a very short time this collaboration will need cpu cycles equivalent to 200 MIPS, 50 Gbytes of disk storage (one week's event generation) and 300 Gbytes of tertiary storage that is readily accessible for reanalysis.

During the year prior to the submission of the proposal, the simulation activity will grow substantially. By October 1991, we estimate that the computing needs will have grown by a factor of 3–4 (in all resources), both because of an increased number of workers devoted to the problem, but also because the sophistication and detail of the detector models will have grown. Further, there will be a need to verify the expected performance of the detector with an increasing fraction of data samples using full simulation of the calorimetry instead of parametrized models. Given the desirability of centralizing computing efforts, we request that the SSCL commit such resources to the SDC needs.

Effective use of the computer hardware requires corresponding software support. We estimate that at least four FTEs will be required (*e.g.* 2 physicists and 2 programmers or some equivalent combination) to maintain the library of software used by the collaboration and the geometry database of the evolving detector design. If the computing is largely supplied as a central facility at the SSCL, we request that the Laboratory assign personnel to work on the SDC software.

This simulation effort cannot be centralized without adequate access to the computing resource. We expect that the users doing the bulk of the computing will increasingly use workstations running some version of the UNIX operating system and perhaps an "X Windows-type" graphical and client/server standard across a network from their home institutions. We estimate the initial network bandwidth requirements to be ≈ 100 kbits/user/s for satisfactory performance, or initially ≈ 2 Mbit s^{-1} *actually available* during working hours for 20 users and we expect this to approximately double by October 1991. We expect that the bulk of the access will be by DECnet protocols at first, but that use of TCP/IP will grow quickly as users increasingly acquire UNIX-based workstations. We request the SSCL assist in providing the necessary network paths at the needed bandwidth. Good network connectivity to collaborators outside the U.S. is also extremely important also. We expect that significant computing resources and effort will also be provided in non-U.S. countries.

An additional high priority use for the network connections (and an additional bandwidth requirement) comes from videoconferencing. We must reach for new technology to provide effective communication between collaborators in different locations and between collaborators and the SSCL. Videoconferencing has been used to good effect for many years over the relatively short distance between SLAC and LBL. A trial installation has allowed videoconferencing between LBL and FNAL since January and its success is such that users are already unable to imagine doing without. New technology has allowed pictures of speakers and transparencies to be transmitted with adequate motion over a fraction (25%) of the ESNET line between the two labs. The SSCL has recently added video capability on its connection to FNAL. It is planned that ANL will soon become the fourth lab with this capability.

The SDC feels that videoconferencing needs to become a standard method of communication within the collaboration. Video capability needs to be enhance at existing locations in the U.S. and new sites need to be added. Video connections to Europe and Japan are in the process of being added. A connection between Pisa and Fermilab for CDF is imminent and we hope to have connection between Japan and the U.S. later this year.

4.7.2. Software Development

The SDC will need to establish and maintain a core of expertise to allow it to identify appropriate computing technologies (both software and hardware) in order to make knowledgeable choices. Software development has already begun for simulation, but these efforts now need to be fully integrated. We need to begin to establish a framework that

will permit ongoing work to continue unimpeded while imposing enough coordination and structure that the software is useful for the whole group and can be maintained for an extended time. To this end, we plan to establish an ongoing planning group with the following charge:

(*a*) Define a model of computing for the experiment. This model will necessarily evolve so that it can incorporate ways for the collaboration to take advantage of new technologies and approaches, where appropriate;

(*b*) Learn about software management techniques, software engineering approaches, and other developments taking place outside of high-energy physics that may be simply and directly applicable to the needs of our collaboration;

(*c*) Develop rules of programming and tools for applying them that allow disciplined approaches to programming within the grasp (and patience) of high energy physicists.

This group will interact closely with the computing efforts of the collaboration, initially by applying new techniques that it identifies to ongoing projects and requirements. For example, the software bus approach can be applied to making the components of simulation packages readily exchangeable. Graphical programming combined with statistical visualization packages can also be applied to the simulation problem in a way that allows very fast iteration between making algorithm changes and viewing simulation results.

We will create a software design group that will design a high-level architecture for the detector software. It will develop a detailed plan for the software that will include a system framework (user interfaces, data management, communications) and detector applications (simulation, calibration, tracking). It will specify the formal plan for software development and the methods by which individual software components can be assigned to individuals or groups within the collaboration. Important steps in the plan will include requirements specifications before code writing and independent review of requirements and of design and implementation of the software.

We must begin the software analysis and design now so that the software design can be included in the proposal. Since the methodology we propose to use is not in wide use within the high-energy physics community, we need to add computing professionals to plan and implement the analysis and design. To accomplish this, we request funding for four computing professionals to work with an estimated 10 physicists initially (4 FTEs) in carrying out the program outlined above. We will investigate the possibility of working with industry and/or university computer science departments to leverage our resources in this area.

4.7.3. Summary of SDC Computing Needs

The design of a large software system for the SDC should be viewed with the same seriousness as is that for hardware. It is essential that such design begin immediately, and be carried out by physicists working in conjunction with computer professionals. The SDC requests for computing are summarized in Table 9.

Table 9

SDC requests for computing-related resources.

Request	Comment	Funding Source
200 MIPS, 50/300 Gbytes (short/long term)	SDC Simulation	SSCL
4 FTEs at the SSCL	Simulation software support	SSCL
> 2 Mbit s^{-1} networking bandwidth	Simulation using SSCL resources	SSCL
Enhanced videoconferencing	SDC coordination	EoI, SSCL
4 FTE software professionals	SDC software system design/prototyping	EoI

5. Detector performance

5.1. Methodology and overview

In this section we present some examples of detector response based on simple parametrizations of subsystem performance. We consider a variety of processes, including some that can be measured in the early stages of the experiment, when the yearly integrated luminosity is small ($\lesssim 10^{38}$ cm^{-2}), as well as others that will require high integrated luminosity ($\gtrsim 10^{40}$ cm^{-2}). Measurements involving known particles such as the Z boson are included, as well as searches for esoteric particles motivated by theoretical models.

The physics processes that will be discussed are:

(*a*) The detection of a Higgs boson via its decay to ZZ or ZZ^* (Z^* denotes a virtual Z) which results in the final state of four charged leptons or two charged leptons and missing transverse momentum.

(*b*) The detection of pairs of gauge bosons of large invariant mass as a signal for new physics in the electroweak sector.

(*c*) The detection of a top quark pair from events with one or two isolated leptons and jets.

(*d*) The detection and determination of the properties of a new neutral gauge boson.

(*e*) The detection of quark compositeness from jet events at very large transverse momentum.

(*f*) The detection of a supersymmetric particle (gluino) decaying to jets and non-interacting particles that give rise to missing transverse momentum.

2. Definition of detector parameters for simulation

In order to evaluate detector performance in a uniform manner, we have used a simple parametrization of the detector[39]. Although much more detailed studies will be done in the future, this simple parametrization is sufficient to demonstrate the power of the solenoidal detector. The following detector parameters and resolutions are employed in these studies (momenta are in GeV/c and energies in GeV, and the symbol $\oplus$ means that the terms are added in quadrature).

The calorimeter is segmented into projective towers of size $\Delta\eta \times \Delta\phi = 0.05 \times 0.05$ for $|\eta| < 3$ and 0.10×0.10 for $|\eta| > 3$. The hadron calorimeter energy resolution in these studies is

$$\frac{\Delta E}{E} = \frac{0.50}{\sqrt{E}} \oplus 0.03 \qquad (|\eta| < 3)$$
$$\frac{\Delta E}{E} = \frac{0.80}{\sqrt{E}} \oplus 0.03 \qquad (3 < |\eta| < 5)$$

while the electromagnetic calorimeter resolution is chosen to be

$$\frac{\Delta E}{E} = \frac{0.20}{\sqrt{E}} \oplus 0.01 \ .$$

Electrons and muons are identified in the region $|\eta| < 2.5$, where we assume an η-dependent momentum resolution for the tracking system given by

$$\frac{\Delta p_t}{p_t} = a \oplus b p_t \ ,$$

$$\begin{aligned} \text{with } a = \ & 0.005 \text{ for } |\eta| < 1.0 \\ & 0.005|\eta| \text{ for } |\eta| > 1.0, \\ \text{and with } b = \ & 0.0002 \text{ for } |\eta| < 1.6 \\ & 0.0002 + 0.00074(|\eta| - 1.6) \text{ for } 1.6 < |\eta| < 2.5 \ . \end{aligned}$$

For electrons, the tracking or calorimetric energy measurement is used, whichever is better. For hadronic energy measurements, the effect of non-gaussian tails is included, using a parametrization developed by the CDF collaboration[40]. The degradation of resolution associated with coil support structures ($1.25 \leq |\eta| \leq 1.5$) is incorporated in the parametrization; at the worst point the resolution is degraded by a factor of 1.7 [39].

The momentum resolution of the muon system is given by

$$\frac{\Delta p_t}{p_t} = a \oplus b p_t \ ,$$

$$\text{with } a = \ 0.160\sqrt{\sin\theta} \text{ for } |\eta| < 1.5,$$

$$0.035 \tan\theta \sqrt{(7.08 - 10.8 \tan\theta)\cos\theta} \text{ for } 1.5 < |\eta| < 2.5,$$

and with $b = 0.0004 \sin^2\theta$ for $|\eta| < 1.5$,

$$0.00025 \cos^2\theta \text{ for } 1.5 < |\eta| < 2.5.$$

The momentum measurement of a muon uses information from both the muon and tracking systems.

We take the electron and muon identification efficiency to be 85% for analyses requiring isolated leptons. In the cases where the analysis requires two leptons reconstructing to an on-shell Z boson, lepton identification cuts are relaxed for the second lepton, and the efficiency is taken as 95%.

Unless otherwise noted, all figures in this section include the effects of these resolutions and efficiencies, and all event rates correspond to an integrated luminosity of 10^{40} cm^{-2}. Where relevant, a simulation including the effects of clustering and shower spreading has been used.

3. Examples of detector performance

3.1. Higgs

We consider the decay of a Higgs to ZZ and hence to either $\ell^+\ell^-\ell^+\ell^-$ or $\ell^+\ell^-\nu\overline{\nu}$. Here ℓ indicates either e or μ. If the Higgs has a mass larger than $2M_Z$ then the Z's are real; otherwise one Z is real and the other virtual. In the latter case the branching ratio to $\ell^+\ell^-\ell^+\ell^-$ falls rapidly as the mass is reduced, and Higgs masses below 130 GeV are not accessible unless the integrated luminosity exceeds 10^{40} cm^{-2}[41].

For a Higgs mass of 140 GeV, there are approximately 130 events in final states with e's or μ's for a top mass of either 150 or 250 GeV. Acceptance (0.6), isolation cuts (0.4), and reconstruction efficiencies (0.58) reduce this number to 18. If we are able to detect and measure leptons for $|\eta| < 3$, our acceptance would increase by 30%. In this lower mass region, the background arises from $q\overline{q} \to ZZ^*$ or $\gamma\gamma^*$ (where $*$ indicates a virtual particle), and is very small (< 5 events, before acceptance, isolation and resolution effects)[42]. There is a possible additional background from final states of $Zb\overline{b}$ or $Zt\overline{t}$. The latter background is not large. The former overwhelms the signal unless we require that all four leptons be isolated. These observations are illustrated in Fig. 29 which shows the reconstruction of a 140 GeV Higgs boson. It can be seen from this figure that the assumed resolution of our detector is more than adequate for a signal to be extracted. At a mass of 160 GeV, the signal is approximately 3 times larger. The accessible range of masses could be pushed substantially below 140 GeV only if the experiment is able to accumulate an integrated luminosity in excess of 10^{40} cm^{-2}.

If the Higgs is heavier than $2M_Z$ it will decay to WW or ZZ with a relative branching ratio of about 2:1. The decay rate to $t\overline{t}$ is never sufficient to seriously deplete the WW or ZZ rates. The signal in WW is compromised by the large background of W pairs arising from $t\overline{t}$ production. This background could be reduced by either vetoing on the

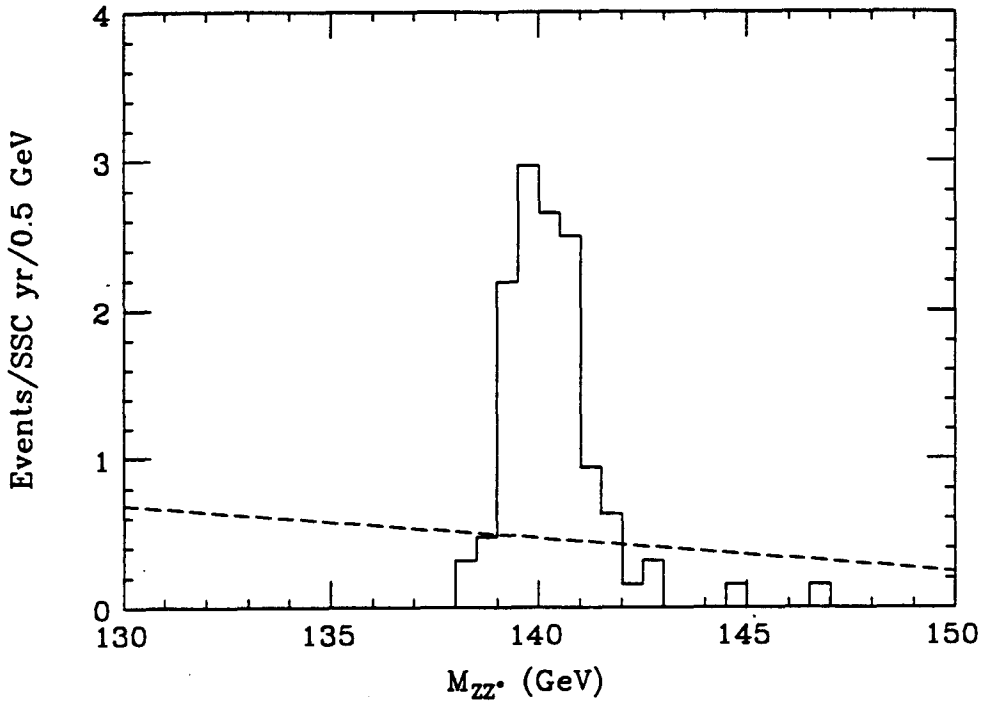

FIG. 29. Reconstructed Higgs mass for $H \to 4e$, 4μ and $2e2\mu$, with $M_H = 140$ GeV. The signals have been combined since resolutions in the different channels for $p_t < 100$ GeV/c are comparable. The background (dashed curve) arises from the $Z + b\bar{b}$ final states. The leptons are all required to have $p_t > 5$ GeV and be isolated. In this case "isolated" means that there is less than 5 GeV of energy in a cone of radius ΔR $(= \sqrt{\Delta\eta^2 + \Delta\phi^2}) = 0.7$ around the lepton direction. In addition, one pair of leptons is required to have $M_{\ell\ell} = M_Z \pm 10$ GeV, the other to have 20 GeV$< M_{\ell\ell} <$ 80 GeV.

presence of b quarks in the event (from $t \to Wb$) or by requiring that there not be much jet activity apart from the Ws. Further work is needed to determine if either of these ideas is practicable, and the WW mode will not be considered further here.

There are two ways that the ZZ final state may be detected. First both Z's can decay to e's or μ's. In this case one is looking for a final state with four isolated leptons that reconstruct to form two Z bosons. Potential backgrounds are: (a) continuum production of Z pairs and (b) other final states that result in four charged leptons. If we select events with four isolated leptons, choose the $\ell^+\ell^-$ pair with invariant mass closest to the Z mass, and plot the invariant mass of the other pair, we get the distribution shown in Fig. 30. Included in this figure are contributions from the Higgs and from $Z + t\bar{t}$ and $Z + b\bar{b}$ final states. This figure shows that the resolutions of our detector are such that a cut requiring the invariant mass of both dilepton pairs to be close to the Z mass is sufficient to reduce these backgrounds below the signal. The $t\bar{t}$ final state results in less than 0.1 fb of effective rate if we require that the four isolated leptons reconstruct to two pairs, each with an invariant mass within 20 GeV of the Z mass. These backgrounds can be eliminated completely by requiring that the p_t of the dilepton pairs be large (> 100 GeV). Thus, the only remaining background to the Higgs search is continuum ZZ production from $q\bar{q}$ [43] and gg [44], the latter being approximately 20% of the former. The reconstructed Higgs peak as well as this background are shown in Fig. 31. The width of the reconstructed

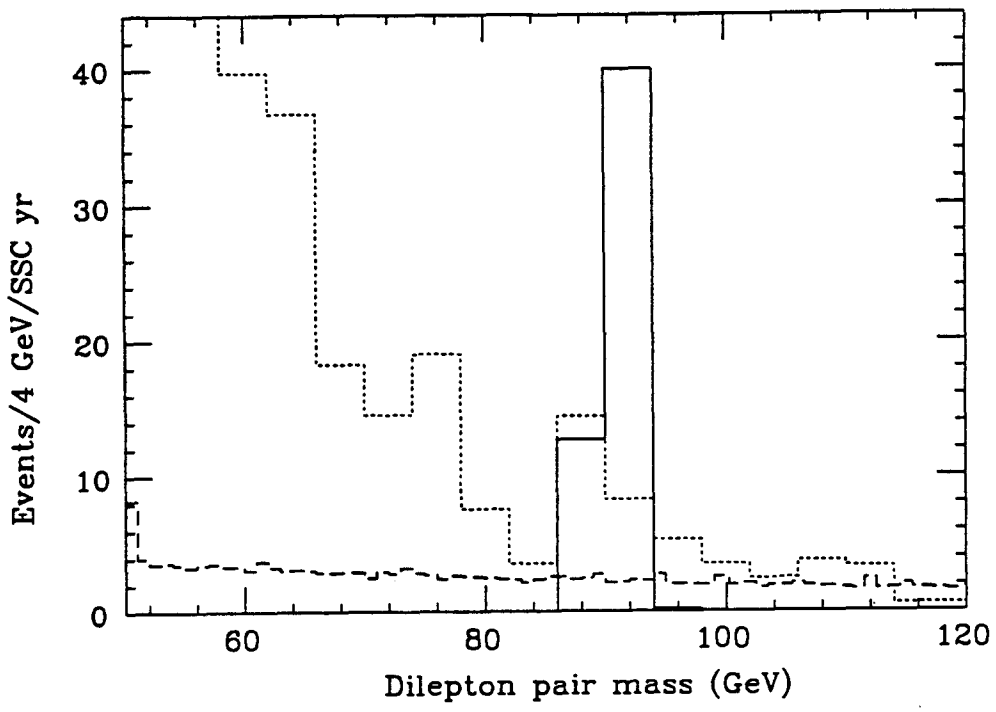

FIG. 30. The invariant mass distribution of isolated electrons (*i.e.* there is less than 2 GeV in a cone of radius $\Delta R(=\sqrt{\Delta\eta^2+\Delta\phi^2}) = 0.2$ around the lepton direction) with $p_t > 10$ GeV. The resolution in the muon final states is comparable for the leptons contributing to this plot. The events arise from a Higgs boson of mass 400 GeV (solid) and from QCD events with $Z + t\bar{t}$ (dashed) and $Z + b\bar{b}$ (dotted) final states. The lepton pair with invariant mass closest to M_Z is selected and the invariant mass of the other pair is shown.

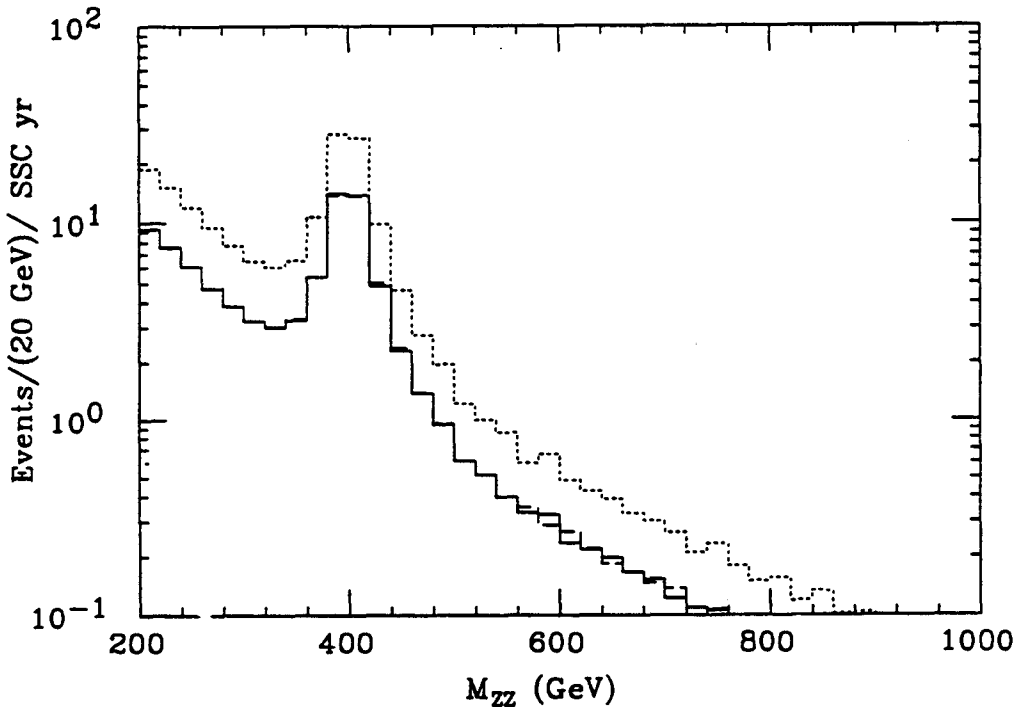

FIG. 31. The reconstructed mass of a ZZ system for the final states $4e$ (solid), $H \to 4\mu$ (dashes) (these curves are almost indistinguishable) and $2e2\mu$ (dots) showing the peak due to a Higgs of mass 400 GeV. The leptons are all required to be isolated. The background arises from $q\bar{q} \to ZZ$.

Higgs is determined by the intrinsic width of the particle and not by resolution effects. Hence the electron and muon final states appear the same. The background is small relative to the signal and a discovery in this final state is limited by rate only. It ceases to be effective at a luminosity of 10^{40} cm^{-2} if the Higgs mass exceeds about 600 GeV.

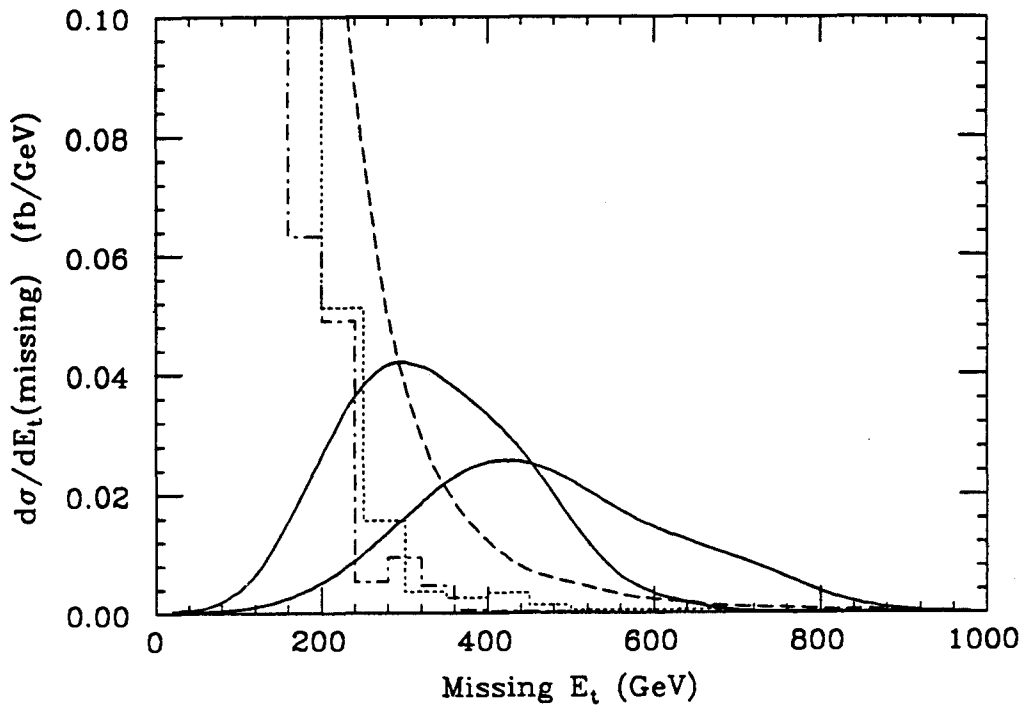

FIG. 32. The distribution in missing E_t from the process $H \to ZZ \to e^+e^-$(or $\mu^+\mu^-$)$\nu\bar{\nu}$ (dark (light) solid curve has $M_H = 700$ (900) GeV). The reconstructed Z is required to have $p_t > 200$ GeV and the charged leptons to have $|y| < 2.5$. The background (dashed curve) arises from $q\bar{q} \to ZZ$. The background (dot-dashed) arises from the final state $Z + jets$ where the missing E_t is generated by calorimeter resolution or by losing energy out of the end of the detector. The background (dotted) arises from the final state $t\bar{t}$ where there is an e^+e^- (or $\mu^+\mu^-$) pair of mass $M_Z \pm 20$ GeV and the missing E_t is due to neutrinos. The events are rejected if they contain a jet with $E_t > 300$ GeV.

Secondly, in the channel $H \to ZZ \to \nu\bar{\nu}e^+e^-$ (or $\mu^+\mu^-$) where the combined branching ratio is larger, the signal shows up as a peak in the missing transverse energy or in the transverse mass of the observed Z and the missing E_t. In this case we assume 700 GeV and 900 GeV for the Higgs mass. The missing E_t distribution is shown in Fig. 32. Here the background is not only from ZZ final states, but also from the $Z + jets$ final state where the jets are mismeasured or lost down the beam hole and from $t\bar{t}$ events where two isolated leptons are produced with an invariant mass close to that of the Z. The background due to mismeasured jets is comparable to the signal unless we impose a cut requiring that there be no jets with $E_t > 300$ GeV. This happens because the non-gaussian tails that we have assumed in the jet energy resolution result in a small number of jets having their energy substantially mismeasured. Once this cut has been made, it is clear that our resolutions are sufficient to reduce the backgrounds below the irreducible background

from the ZZ final state (see Fig. 32). Here again, the search for the Higgs is therefore limited by the production rate and not the background [45].

3.2. Other signals of weak interaction symmetry breaking

In the case where the Higgs boson is very heavy, interactions between the Higgs and longitudinally polarized W and Z bosons become strong[46]. In this case and in many models where the Higgs is not elementary, but rather is a bound state of fermions (technicolor theories[47]), one must look for an excess of gauge boson pairs with large invariant mass over that expected in the Standard Model. In technicolor models resonances may appear in the ZZ, WW, WZ or $Z\gamma$ channels. These resonances are analogous to the ρ and ω mesons of QCD. The final state $Z\gamma$ can be fully reconstructed to detect a techniomega[48]. Figure 33 shows the invariant mass distribution of $Z\gamma$ where the Z is detected via its decay to lepton pairs. The small natural width of the techniomega (of order 10 GeV) enables a peak to be clearly seen over the background which arises from $q\bar{q} \rightarrow Z\gamma$; the resonance is clearly visible at a mass of 1.46 TeV. There is an additional background from the final state $Z + jets$ where a jet fragments so that a single π^0 carries most of its energy. This background is difficult to estimate reliably but is below that of $Z\gamma$ provided the ratio of isolated π^0's to jets at the same p_t (> 200 GeV in this case) is less than 0.01[49].

In some technicolor models there can exist exotic particles some of which carry both lepton number and color and hence are produced with large rates and decay to leptons plus jets[50]. The ability of our detector to reconstruct these final states will be crucial to their observability.

More difficult to detect than the techniomega is the case where the manifestation of new physics is an excess of events in the final states of two gauge bosons with large invariant mass [52]. Here rates are low. For example, in the W^+W^+ and W^-W^- final states one expects 38 events where both W's decay leptonically to either $e\nu$ or $\mu\nu$ over a background of 25 [53]. Here the WW invariant mass is required to be more than 1 TeV* and the leptons are required to have $|\eta| < 2$. The ability to extract a signal relies critically on the ability to calculate/measure the background (presently uncertain to 30%). This experiment is probably only practicable at luminosities greater than 10^{33} cm^{-2}s^{-1}.

3.3. Top quark

It is possible that the top quark will not be discovered before SSC turn-on. We now know its mass lies in the range 89 [1] to 250 GeV[2] if it couples and decays according to the Standard Model. The total cross section for production of $t\bar{t}$ pairs at SSC is 92 nb (1.5 nb) for $M_t = 89(250)$ GeV. Hence experiments are feasible at low luminosity and very stringent cuts can be applied to the signal if they would assist in, for example, determining the mass.

* These event rates include our efficiencies. A more detailed study, which would have to replacement of the invariant mass cut by experimentally accessible cuts cannot yet be made since the background calculation[54] is not available in the appropriate form.

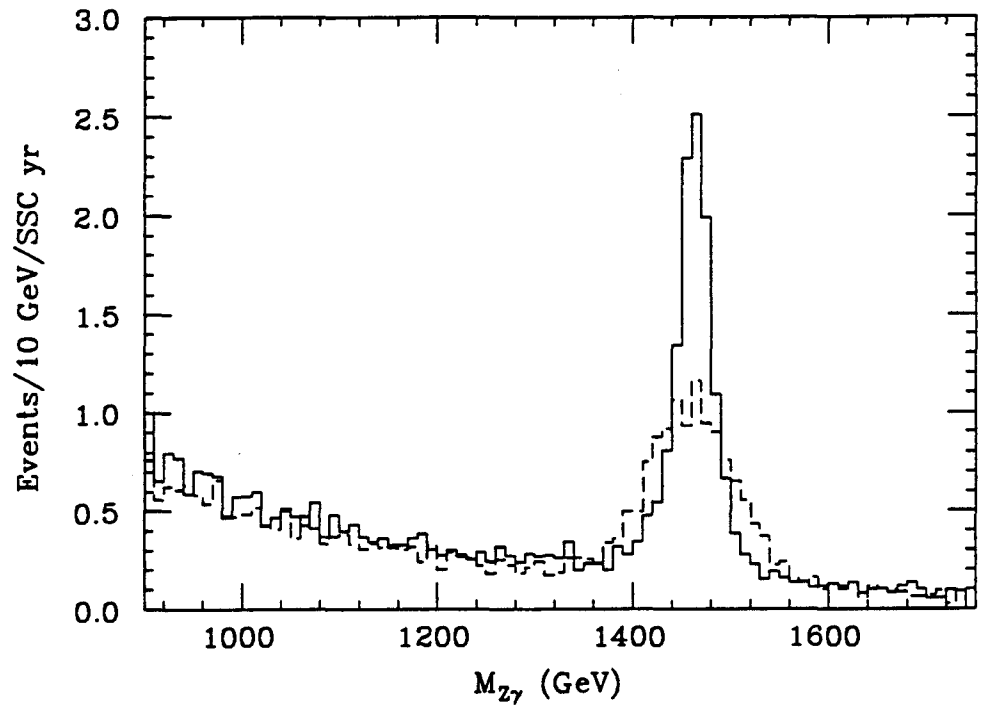

FIG. 33. The invariant mass of the final state system of a photon and an e^+e^- (solid histogram) or $\mu^+\mu^-$ pair (dashed histogram). The lepton pair is required to have mass $M_Z \pm 10$ GeV. The leptons have $|\eta| < 2.5$ and the photon has $|\eta| < 3.0$. The peak corresponds to the production and decay of the techniomega particle of mass 1.46 TeV[51].

The mode in which both the t and $\bar{t}$ decay to leptons, $t\bar{t} \rightarrow e\nu\mu\nu b\bar{b}$, has the least background. There is a very small background from the W^+W^- final state and from the Drell-Yan production of τ pairs as shown in Fig. 34. To make this plot the e and μ with the largest p_t are chosen. The leptons are required to be isolated (see figure caption for details). More than 90% of the lepton pairs in this plot come directly from the t and $\bar{t}$ decays and not from the subsequent decays of charm and bottom. It can be seen from the figure that an integrated luminosity of 1 (10) pb^{-1} is sufficient to discover top in this mode[55].

In the Standard Model, the top branching ratios are known and a measurement of the production cross section can be used to determine the mass. The current theoretical uncertainly of 30%[56] on the production cross section implies that the smallest achievable error on M_t using this method is $\sim$ 20 GeV. However, if the top quark can decay into a charged Higgs, the branching ratio into Wb will differ from the Standard Model. This implies that an independent way of measuring the top quark mass is required.

The mass can be measured by reconstructing a $t\bar{t}$ event in the case where one quark decays semi-leptonically into an isolated lepton, an energetic neutrino, and a jet, and the other quark decays hadronically. In this channel, the largest background is $W(\rightarrow e\nu) + jets$ as the background from $b\bar{b}$ + jets is small provided that the leptons are isolated. To reduce this background, one has to require a second W boson in the event by detecting the jets produced by its hadronic decay and possibly to require the presence of b quarks in the event. Since there are a large number of partons in the final state, the effect of jet overlap on the reconstruction efficiency is an important issue. We have addressed this by simulat-

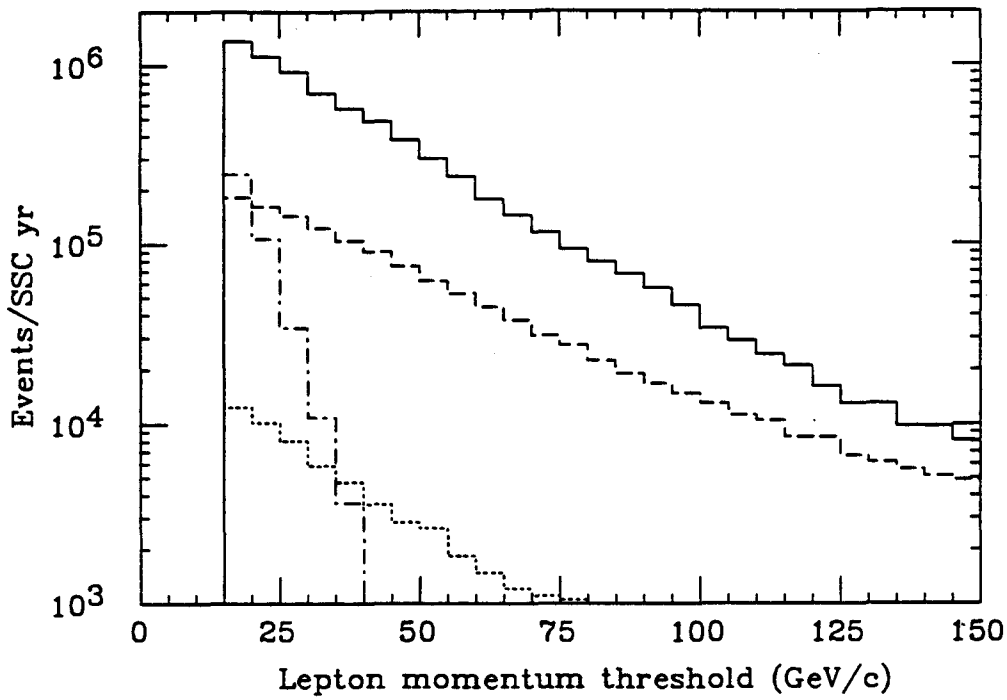

FIG. 34. The rate for the production of $e^{\pm}$ and $\mu^{\mp}$ from $t\bar{t}$ production and decay. Both the e and the μ have $p_t > p_0$ (*i.e.* the rate is integrated for $p_t > p_0$). The e and μ are required to be isolated, *i.e.* there is less than 2 GeV of additional energy in a cone of $\Delta R = 0.2$ around the lepton direction. The solid (dashed) curve has $M_t = 150$ (250) GeV. Also shown is the background from W pair production (dotted) and from Drell-Yan production of τ pairs (dot-dashed).

ing the tower-to-tower response of the calorimeter and reconstructing the jet directions and energies using a fixed cone clustering algorithm. Figure 35 shows the dijet mass spectrum in events where we have required three jets and an isolated electron with $p_t > 20$ GeV (details of the cuts are described in the figure caption). It can be seen that for $M_t = 150$ GeV, the dijet mass resolution of this detector is sufficient to see the peak at the W mass with a signal to background ratio better than 1:1 above both the combinatorial background and the physics background from the $W+3$ *jet* process. The apparent width of the W peak results not only from calorimeter resolution, but from kinematic reflections that occur when one of the b-jets is used to form the dijet system. This problem becomes more severe as the top mass increases and the E_t of the b jets rises. Hence, to convincingly demonstrate the existence of a W signal at higher top masses, we must be able to tag b quarks.

We have studied the b quark tagging efficiency as a function of the E_t of the b jet[57]. We require a secondary vertex containing at least two charged tracks separated from the event vertex by at least 3 σ. The tagging efficiency rises rapidly with b-jet E_t, and reaches a constant value of $\sim 50\%$ for $E_t \geq 50$ GeV and $|\eta_b| < 2$. The efficiency for tagging two b's in a $t\bar{t}$ event has been investigated as a function of the top mass. It rises from 10% for $M_{\rm top} = 120$ GeV to 21% for $M_{\rm top} = 180$ GeV.

In Fig. 36 we show the dijet mass distribution for $M_t = 200$ GeV where we have required that the events have two tagged b jets. With the b tagging, a peak at the W mass is clearly seen. Here the width of the peak is a result of the resolution of the

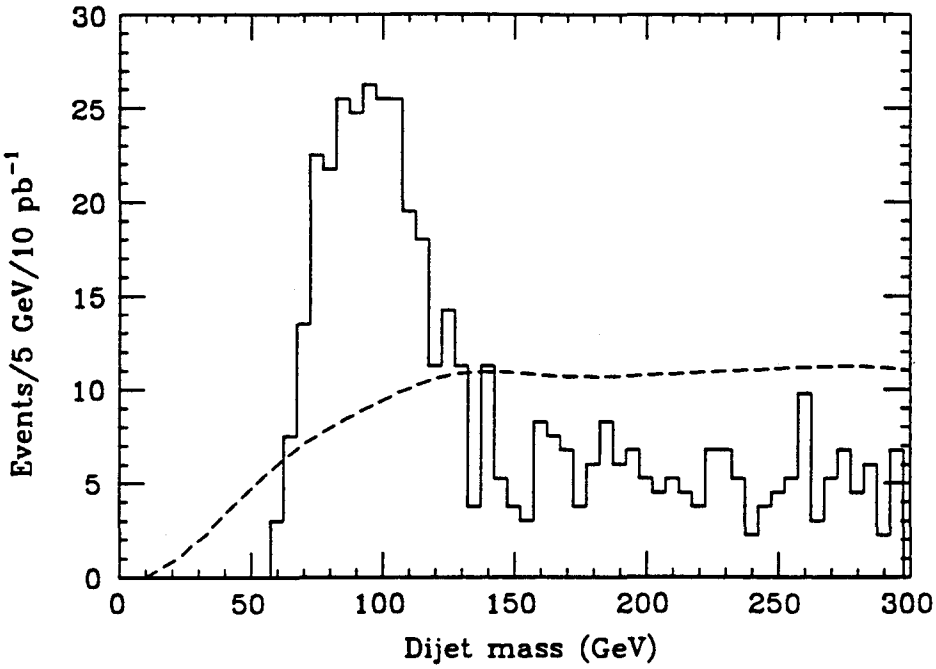

FIG. 35. The distribution (solid curve) in the invariant mass of the dijet system composed of the two jets with highest E_t arising from $t\bar{t}$ production and decay for $M_t = 150$ GeV. The system is required to have $p_t > 180$ GeV. The events are required to have an isolated electron with $p_t > 20$ GeV, at least 20 GeV of missing E_t, and three or more jets each with $E_t > 15$ GeV and $|\eta| < 3$. These jets required to be separated from each other by $\Delta R > 0.7$. The dashed curve shows the distribution from $W + jets$ final states. The top cross section satisfying this selection with a dijet mass < 110 GeV is ~ 25 pb.

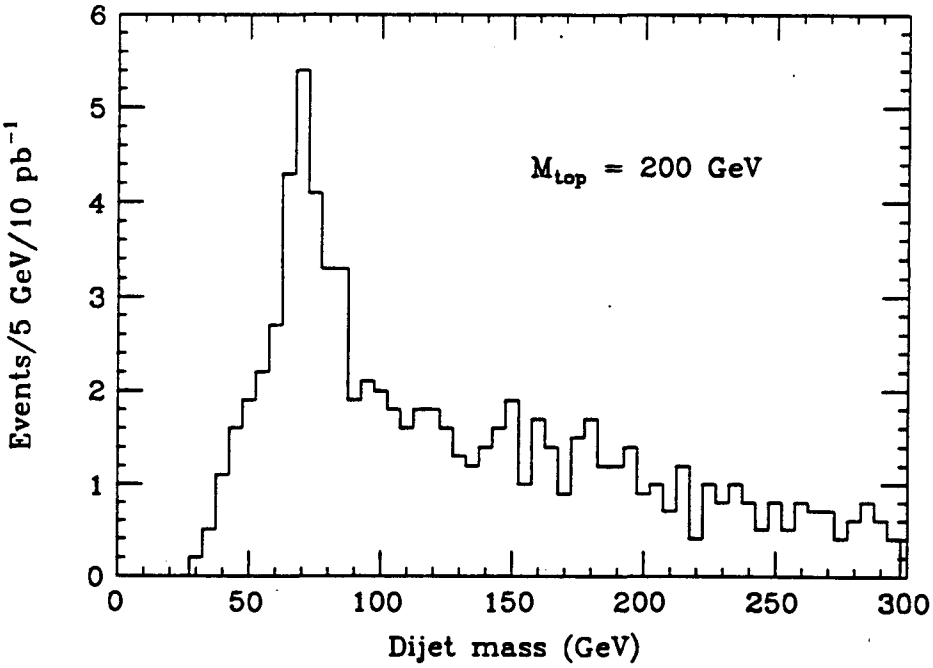

FIG. 36. The distribution in the invariant mass of the dijet system composed of the two leading jets in $t\bar{t}$ events for $M_t = 200$ GeV. The dijet system is required to have $p_t > 60$ GeV. The events are required to have an isolated electron with $p_t > 20$ GeV, at least 20 GeV of missing E_t, and three or more jets each with $E_t > 15$ GeV and $|\eta| < 3$. These jets required to be separated from each other by $\Delta R > 0.7$. The events are also required to have two tagged b–jets neither of which is used in the dijet distribution.

calorimeter. The presence of the tagged b's ensures that the background from $W + jets$ is negligible.

One can determine the top mass by using the invariant mass of the two jets forming the W and another jet. We show in Fig. 37 the invariant mass distribution obtained when we combine a tagged b quark jet with the two leading jets of Fig. 35 . We see a clear peak at approximately the top mass; the small mass shift from the expected value of 150 GeV would be removed by making a more detailed jet energy correction. With an average b quark tagging efficiency of 60%, this signal corresponds to a rate of ~ 2 pb. This analysis becomes more effective at heavier top quark masses, due to the increased p_t of the parent top quark and daughter b quark[58].

A comparison of the measured cross sections for $t\bar{t} \rightarrow e\nu\mu\nu b\bar{b}$ and $t\bar{t} \rightarrow e + jets$ provides a measurement of the top semileptonic branching ratio. If this branching fraction were not consistent with the Standard Model, it could be evidence for new physics—for example the presence of a charged Higgs particle.

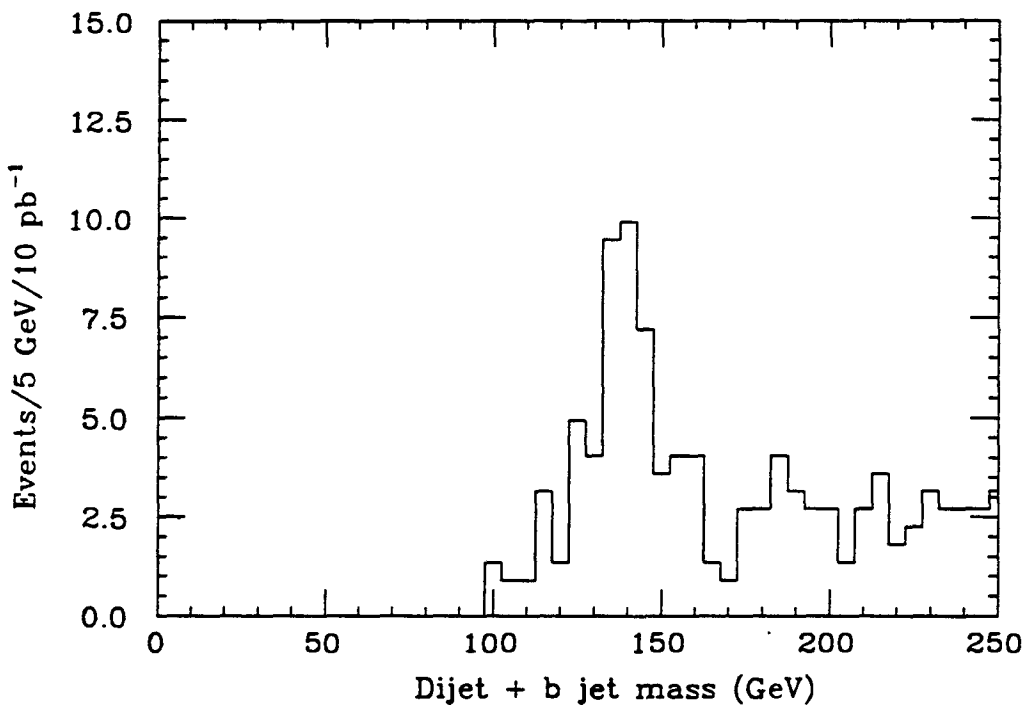

FIG. 37. The invariant mass of the system comprising the dijet pair from Fig. 35 and a tagged b jet. The 3-jet system is required to have $p_t > 180$ GeV and the dijet has invariant mass less than 110 GeV.

3.4. New Z boson

Some models that enlarge the gauge group of the Standard Model predict the existence of new charged and neutral gauge bosons. The details of the masses and couplings are model dependent. For definiteness, the couplings to quarks and leptons used in this

section are those of a Z_η defined in an E_6 model[59]. The branching ratio to charged leptons is 4% per species and the total width is $\Gamma_{Z_\eta} = 0.006 M_{Z_\eta}$. The current CDF limit of $\sigma \cdot \mathrm{B} < 1$ pb implies $M_{Z_\eta} \gtrsim 300$ GeV. For this study masses of 800 GeV and 4 TeV are used. The latter represents the approximate limit of discovery, while the former has a sufficiently large cross-section that one should be able to measure some of its properties.

Figure 38 shows the invariant mass spectra of dilepton pairs from the Z_η as well as the background from continuum Drell-Yan processes. There are no other relevant backgrounds. In the e^+e^- channel, the mass resolution of the detector is comparable to the natural width of the Z_η. Thus the mass can be determined and a limit can be placed on the width. To test universality in the μ and τ channels, the resolution must be sufficient to measure the rate. This figures shows that the broad peak in the μ channel enables the rate to be measured and a measurement of the branching ratio to $\mu^+\mu^-$ to be made.

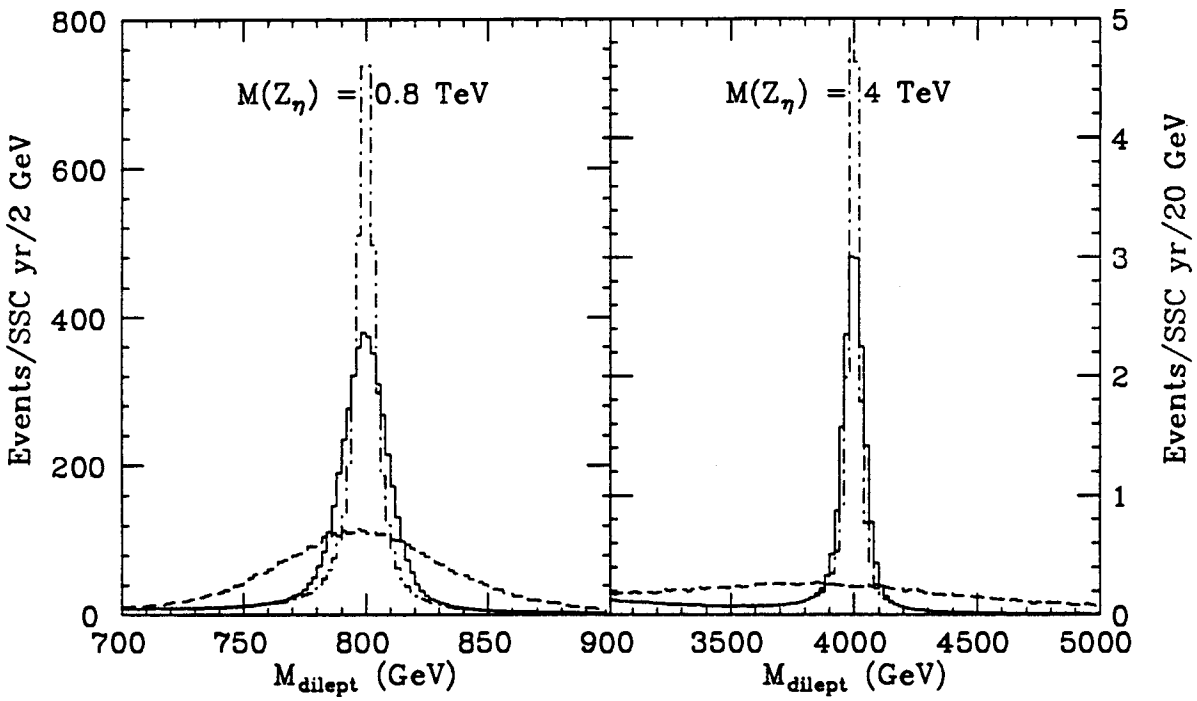

FIG. 38. The cross-section $d\sigma/dM$ for the production of a lepton pair (e^+e^- (solid curve) or $\mu^+\mu^-$ (dashed curve)) as a function of the lepton pair invariant mass. The background is from the continuum production of lepton pairs (Drell-Yan). The peaks correspond a Z_η with mass of 800 GeV and 4 TeV . The dotted curve shows perfect resolution.

In the case of the decay to τ, the situation is more complex. One can look in three final states: $e\mu$, e (or μ) π or π–π. In all cases, there is an irreducible background from the pair production of τ's (Drell-Yan) and from τ's produced in the decays of W's from $t\bar{t}$ events. In the case of an 800 GeV Z_η, the top background is larger than the signal by two orders of magnitude. For heavier Z_η masses, it is possible to reduce this background considerably by requiring that the tracks have large p_t, large invariant mass, be almost

back-to-back in azimuth, and that the events have missing E_t whose azimuthal angle is close to either of the tracks. Figure 39 shows the rate of production of $e\mu$, e (or μ) π or π–π pairs, where the particles are required to be isolated and to have $p_t > 200$ GeV. We have also required that there be at least 100 GeV of missing E_t and that the missing E_t vector in the transverse plane be within 30° of either track.

For sufficiently large values of the invariant mass of the two track system, the Z_η produces a small but statistically significant excess of events, allowing a test of universality. The process is rate-limited for a Z_η mass of 4 TeV; the rate would be 10 times greater if the mass were 3 TeV. There is an additional background from dijet events where both jets fragment into isolated particles. This is rare but the jet rate is very large. The missing energy requirement helps to control this background.

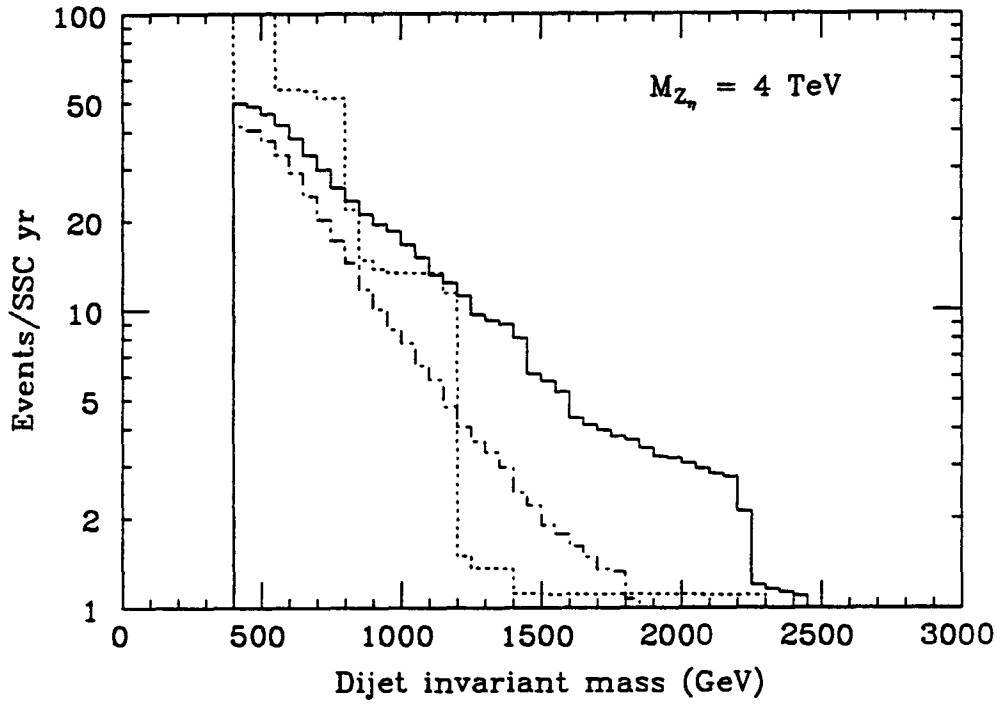

FIG. 39. The rate for the production of $e\mu$, e (or μ) π or π–π final states from the process $Z_\eta \to \tau\bar{\tau}$ with $M_{Z_\eta} = 4$ TeV. The pair is required to have invariant mass $M_{\tau\tau} > M_{\tau\tau_0}$. The tracks are required to have $p_t > 200$ GeV, to be back-to-back within 30° and to be isolated *i.e.* there is less than 5 GeV of additional energy in a cone of $\Delta R = 0.4$ around the track direction. The events are also required to have missing E_t of at least 100 GeV, and the missing E_t vector in the transverse plane is required to be within 30° of either track. Also shown is the background from $t\bar{t}$ production with $M_t = 150$ GeV (dotted) and the Standard Model prediction for Drell-Yan production of τ pairs also shown (dot-dashed) .

By measuring the asymmetry in the leptonic decays, one can gain information on the helicity structure of the couplings of the Z_η. Events are selected for which the Z_η is moving with pseudorapidity η. Since the large-x part of the distribution for a proton is more populated by quarks than antiquarks, for sufficiently large η the quark (anti-quark) that produced the Z_η is likely to have been moving in the same (opposite) direction as the Z_η itself. If the couplings of the quarks to the Z_η violate parity, the Z_η's will then be

produced with some preferred helicity. If the leptonic couplings also violate parity, then by determining the lepton sign one can determine an asymmetry

$$A = \frac{\int_0^{\pi/2} dN/d\cos\theta - \int_{\pi/2}^{\pi} dN/d\cos\theta}{\int_0^{\pi/2} dN/d\cos\theta + \int_{\pi/2}^{\pi} dN/d\cos\theta}$$

where θ is the angle between the direction of the positively charged lepton and the Z_η in the Z_η rest frame. This angular distribution, plotted in Fig. 40, clearly shows an asymmetry. In the case of a 4 TeV Z_η, the asymmetry is more pronounced in the muon channel since the forward muon system enables a better measurement of the signs of forward going leptons.

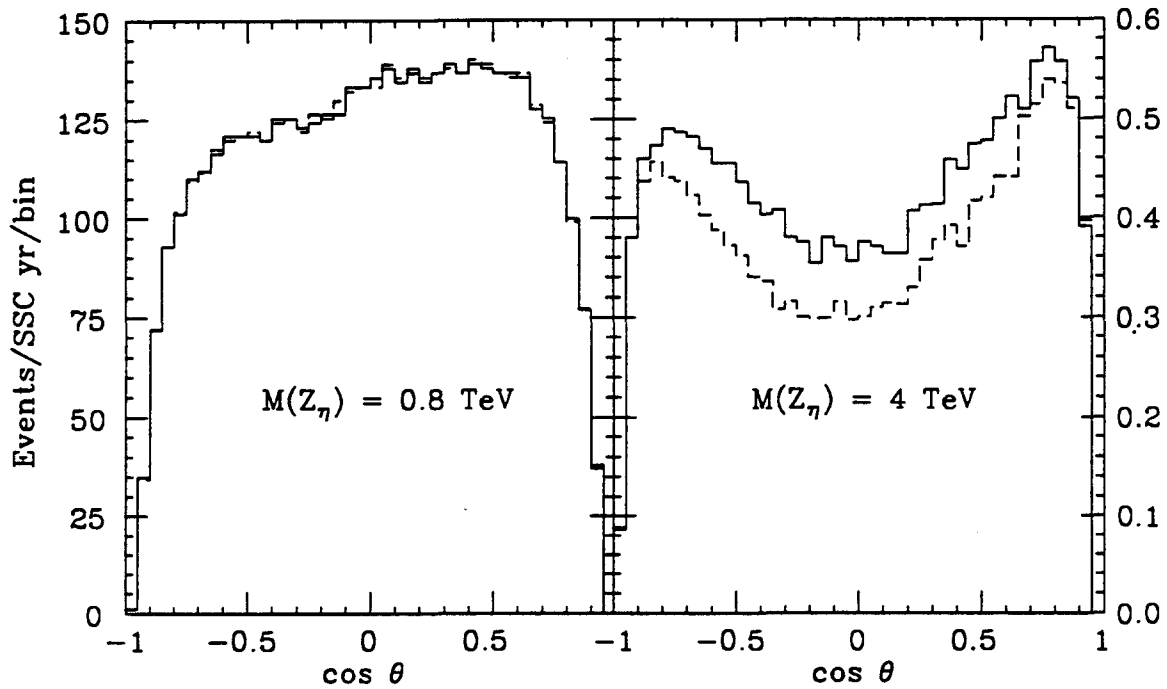

FIG. 40. The cross-section $d\sigma/d\cos\theta$ for the production of a lepton pair (e^+e^- (solid curve) or $\mu^+\mu^-$ (dashed curve)). for a Z_η with mass of 800 GeV and 4 TeV . The reconstructed dilepton invariant mass is required to be $M_{Z_\eta} \pm 100$ GeV in the former case and $M_{Z_\eta} \pm 1000$ GeV in the latter. The longitudinal momentum of the Z_η greater than 500 GeV (1 TeV) in the former (latter) case.

3.5. Gluinos

There are many possible signatures for supersymmetric particles depending on their masses and the masses of other supersymmetric particles into which they can decay. Here we consider a large signal coming from pair production of gluinos[60], one of which decays directly to a photino ($\tilde{\gamma}$) (leading to missing transverse energy) and a $q\bar{q}$ pair. The other gluino decays to $q\bar{q}\ q\bar{q}\ \tilde{\gamma}$. We choose this sequence because it is the dominant mechanism

for obtaining large missing transverse energy and occurs in about 20% of gluino pair production events[61]. We assume that the photino is massless, although the results are not sensitive to this assumption provided that the photino is much lighter than the gluino. This process can give rise to a final state of up to 6 jets and missing transverse momentum carried off by the photinos. The exact number of jets depends upon the jet definition. Here we shall define a jet to be a parton with transverse momentum greater that 50 GeV and a separation from other partons of $\Delta R > 0.7$. Some of the partons from the gluino decays are lost or merged together by this criterion. For $M_{\text{gluino}} = 250$ GeV, the final state with the largest rate has three jets in it. The signal that we therefore consider is three jets and missing E_t.

It is useful to distinguish two types of background: the irreducible physics background that is present even with a perfect detector and the detector dependent background that can arise from resolution effects. Once the detector induced backgrounds are smaller than the intrinsic physics backgrounds, further detector improvements do not enhance this signal. The physics background that we consider here is the production of a Z boson and 3 jets (where $Z \rightarrow \nu\bar{\nu}$). Other possible physics backgrounds, such as $W(\rightarrow \tau\nu) + 3\ jets$ are smaller than or comparable to this one; all such additional backgrounds are present even with a perfect detector. Backgrounds from an imperfect detector arise from the mismeasurement of the jet energies in QCD multi-jet events or from the loss of energy down the beam hole. The former is a more serious problem. The dominant background arises from the case where there is a very energetic jet whose energy is measured to be substantially below its true value due to the non-gaussian tail on the resolution function that we are using. In this case the missing E_t vector (in the plane transverse to the beam) is close to that of the jet with the largest E_t. A cut on the angle between these is effective in reducing this background. It can be seen from Fig. 41 that the assumed detector resolution is then good enough to reduce mismeasured QCD background below the irreducible physics background and that the gluino signal can be clearly extracted. In the case of $M_{\text{gluino}} = 1$ TeV the missing E_t is larger although the production rate is less; the signal is easier to extract in this case [62].

3.6. Quark compositeness

The measurement of $d\sigma/dE_t$ for jets can be used to study models of quark substructure and to search for exotic particles decaying into two jets. If quarks are made of more fundamental objects with a binding scale of order Λ, one can expect a 4–fermion interaction between quarks for momentum transfers below Λ of the form[63]:

$$\mathcal{L} = -\frac{g^2}{2\Lambda^2}(\overline{u}_L\gamma^\mu u_L + \overline{d}_L\gamma^\mu d_L)(\overline{u}_L\gamma_\mu u_L + \overline{d}_L\gamma_\mu d_L)$$

Here g is the coupling strength of the interaction responsible for binding the quark constituents. We shall follow convention and choose $g^2/4\pi \equiv 1$. The inclusive jet cross section will receive a contribution from the interference of this term with that arising from gluon exchange. This contribution does not fall as fast with the transverse energy

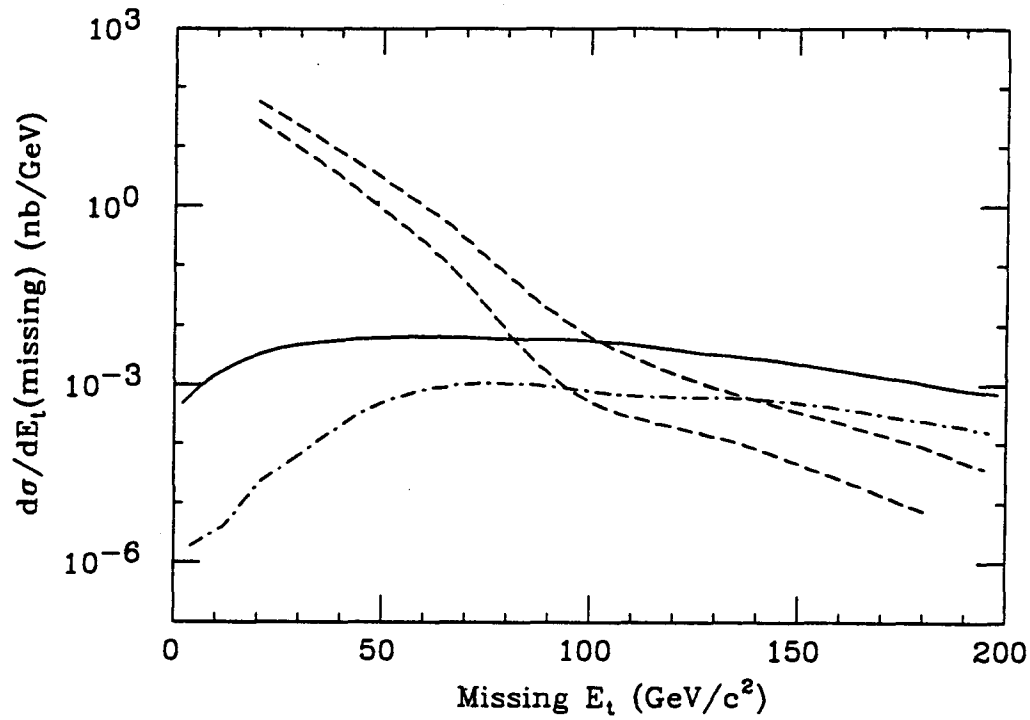

FIG. 41. Missing transverse energy distributions resulting from gluino (of mass 250 GeV) pair production (solid curve), $Z(\rightarrow \nu\bar{\nu})$ plus 3 jets (dash-dotted curve) and QCD background (dashed curves). The last arises from events with 3 mismeasured jets or 4-jet events in which one jet escapes though the beam hole. The gluino pair decay chain $\tilde{g}\tilde{g} \rightarrow q\bar{q}\tilde{\gamma}q\bar{q}q\bar{q}\tilde{\gamma}$ with a combined branching ratio of 20%. The events are required to have three jets each with $E_t > 50$ GeV separated from each other by $\Delta R < 0.7$. The upper (lower) dashed curve has a cut of $\phi > 20°(40°)$ where ϕ is the azimuthal angle between the missing transverse momentum and the nearest jet. This cut has little effect on the signal.

as QCD does; hence there will be a flattening of the cross section and an excess of events in the high E_t region.

To test for compositeness, the following technique can be used[64]. The predicted shape of $d\sigma/dE_t$ from QCD plus a compositeness term is calculated for a range of structure functions and Q^2 scales and for a range of values of Λ. The overall normalization of each curve is forced to agree with the data in the region where the effect of the compositeness term is small (this removes any systematic uncertainty in the normalization of the measured cross section). An appropriate χ^2 is then calculated in the high E_t region.

We define the maximum compositeness scale attainable at the SSC to be the value of Λ that would produce at least 100 events in a region of E_t where the cross section exceeds the QCD prediction by more than 50%. in one year of running at $\mathcal{L} = 10^{33}$ cm^{-2}s^{-1}. This value is $\Lambda \sim 30$ TeV. Figure 42 shows the ratio of the predicted jet cross section, including compositeness, to the QCD predicted cross section for values of $\Lambda = 30$, 25, 20 and 15 TeV. Also shown on the figure is the deviation from the QCD prediction that results from the jet energy resolutions described in this section. It can be seen that resolution smearing, even when non-gaussian tails are included, is a small effect on the QCD signal.

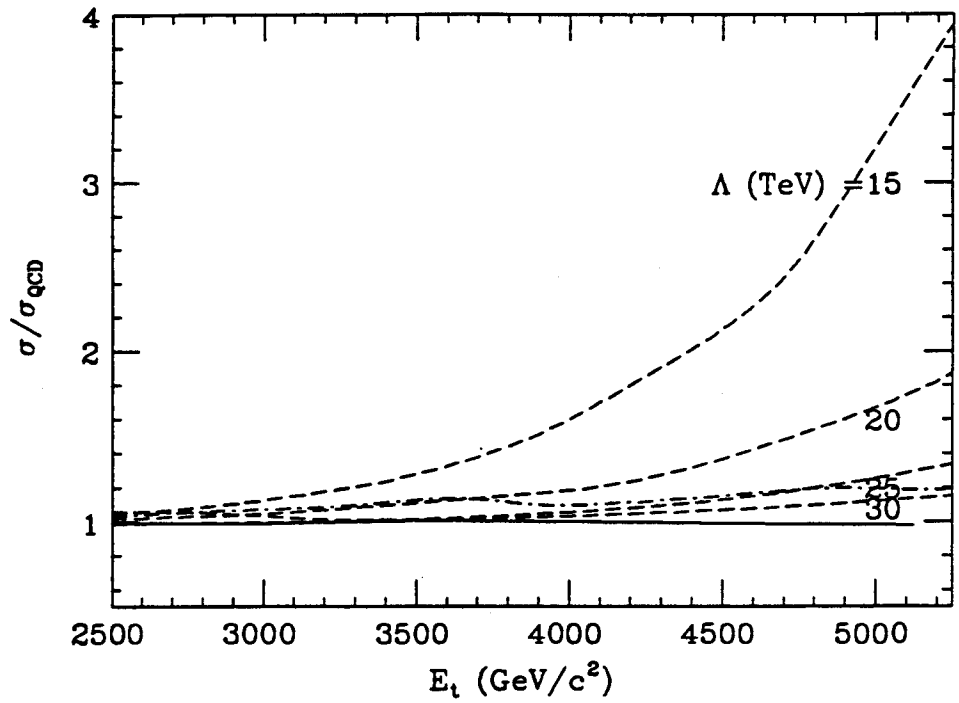

FIG. 42. The ratio of the observed jet cross section including compositeness to the QCD predicted cross section for values of Λ = 30, 25, 20 and 15 TeV (dashed). For 1 SSC year, these values correspond to an excess of events over QCD of 70, 5500, 1600, and 7800. The solid curve shows the effect of resolution alone. The dot-dashed curve shows the effect of an E_t-dependent error on the energy scale, arranged so that it is correct for $E_t < 2$ TeV and deviates linearly above this energy so that it is 2% high at 5 TeV. This corresponds to a "worst case scenario" for SDC. In all cases the jets are required to have $|\eta| < 1$.

The flattening of the jet cross section that results from compositeness cannot be mimicked by an energy-independent error on the measurement of jet E_t. Such an error will change the normalization but not the shape of the observed distribution. For comparison, we have included in Fig. 42 a curve showing the effect of an energy dependent miscalibration of the jet energy scale. The maximum size of the miscalibration over the range of interest is 2%; the resulting distribution is comparable in size to a 25 TeV compositeness effect[65]. Unlike the other physics examples discussed in this chapter, here our ability to detect new physics may be limited by resolution effects rather than event rates or intrinsic (detector independent) backgrounds.

4. Simulation work to be done

The examples presented in the previous section were based upon simple detector parametrizations. Such parametrizations are useful for a preliminary evaluation of detector performance, but more detailed Monte Carlo efforts are an essential ingredient of the detector design process. These efforts provide a guide to the relevant advantages or disadvantages of any particular choice of detector design or technology and allow an assessment of the ability of the final detector design to achieve the collaboration's physics goals. Work has already begun in this area[66].

At present, there are a large number of diverse, and partially overlapping, simulation

activities within the SDC. Some of these activities have developed within the context of the subsystem proposals; others represent the first attempts to produce general SSC detector simulation packages. The SDC intends to merge these efforts into a single, unified simulation framework. Our goal is to produce a fast and accurate simulation and to use this simulation to evaluate detector subsystems.

The steps necessary to achieve this goal include:

(*a*) Surveying existing physics and detector simulations.

(*b*) Comparing results for areas in which more than one technique exists.

(*c*) Defining (with the subgroup on computing) the software environment in which the overall simulations will be developed. This includes the establishment of coding ground rules.

(*d*) Defining the framework that will allow different detector descriptions with common outputs for comparisons.

(*e*) Defining data structures for geometry/detector response specification, physics generator output, simulation output and analysis output.

(*f*) Establishing a library of simulation software and a set of maintenance and distribution procedures for this software. We expect the primary source code to reside at the SSC Laboratory.

Once a suitable simulation framework exists, detailed comparative studies of SDC detector design issues will be performed. Most of the comparisons can be effectively carried out by small (2–4) teams of physicists with well defined goals and realistic deadlines. We estimate that it will require about ten such teams, or approximately 20 FTE to carry out the program of simulation work needed to develop a proposal. The teams will be set up by and report back to the simulation organizers. We emphasize that our manpower estimate does not include the considerable amount of work needed to establish the detector descriptions. This work will mainly be carried out by members of the detector subgroups.

We will need support for the acquisition of a number of simulation development systems of the server+workstations kind. The location of these systems will be determined by the organizational structure that is developed and the distribution of the working teams. The acquisition of these systems should be done in close consultation with the SSC Laboratory staff and the SDC computing group to ensure future compatibility of resources. It is also most important that those responsible for providing the centralized SSC computing facilities understand our needs (*e.g.* the first simulations will be simple and fast but will potentially produce a lot of data and heavy I/O load) and react accordingly.

5. Detector assembly, facilities and test beam requirements

We have begun to study the design of the underground hall and to develop descriptions of the surface facilities needed at the SSC Laboratory for the SDC detector. This study examines:

(*a*) Above-ground *vs.* below-ground assembly tradeoffs.

(*b*) Underground hall floor-space requirements for the simultaneous assembly of the muon system and the calorimeter.

(*c*) Construction schedules for the detector based on time and motion studies (see the following section).

(*d*) Manpower requirements for detector assembly.

(*e*) Needs for cranes, tooling, and fixtures necessary to build and service the detector.

(*f*) Constraints on auxiliary service areas, including a layout of the shafts and support buildings necessary for operation of the detector.

(*g*) Utilities requirements, including power requirements (60 Hz, 400 Hz, HVAC, DC, *etc.*), heat removal (A/C, ICW, CHW, LCW, and RAW), cryogenic systems (helium, liquid argon, liquid nitrogen), and gas systems.

(*h*) Safety requirements for detector construction and operation.

This work is being coordinated with Physics Research Division of the SSC Laboratory, and will be part of the basis for the facilities report to be compiled by the Division. This work is only beginning, and must be continued with the assistance of the SSC Laboratory.

5.1. Assembly scenario for the Type-S detector

We have made preliminary assessments of the assembly procedure for a detector similar to the Type-S solenoid design. For purposes of determining assembly methods and underground hall requirements, a detector design was "frozen" some months ago. This model detector does not correspond precisely to any of our current examples, but it is nevertheless similar enough to provide important information. It employs a Type-S solenoid surrounded by a modular calorimeter assembled into five calorimeter bays: three central bays, each 3 m long, and two endcap bays. One significant difference between this detector and the one described in previous sections is the shape of the external iron muon toroids, which were chosen to have a square rather than an octagonal cross-section. Square iron toroids were used in the intermediate-angle region since they, rather than the air-core toroids, would have the greatest impact on the design of the underground hall floor. This design has been used in estimating fabrication schedules and in examining the construction dynamics. Figures 44 through 46 are three-dimensional representations of this detector during three phases of construction. Figure 44 shows the hall six months after beneficial occupancy. The floor area of the hall is 28 m wide (x direction) by 81 m long (z, or beam line direction). It is connected to the surface by a construction shaft in the lower left corner of the figure (not shown) and two auxiliary shafts along the top

edge of the picture. Also not shown are the two small utility and cable shafts for the detector. During assembly, the hall is temporarily partitioned into two large volumes: one for assembly of the muon iron toroids and a second smaller volume for calorimeter construction. Starting in the lower left hand corner of the figure and proceeding diagonally to the upper right hand corner we see (*a*) the first of four square intermediate-angle muon toroid half-sections with a square cutout for the beam line, (*b*) the bottom layer of the barrel muon toroid (*c*) the outline of a wall separating the muon iron assembly area from the calorimeter assembly area, and (*d*) an empty mechanical support for holding up one of the central calorimeter bays. Calorimeter modules are brought into the hall through the auxiliary shaft shown in the upper left hand corner of the figure.

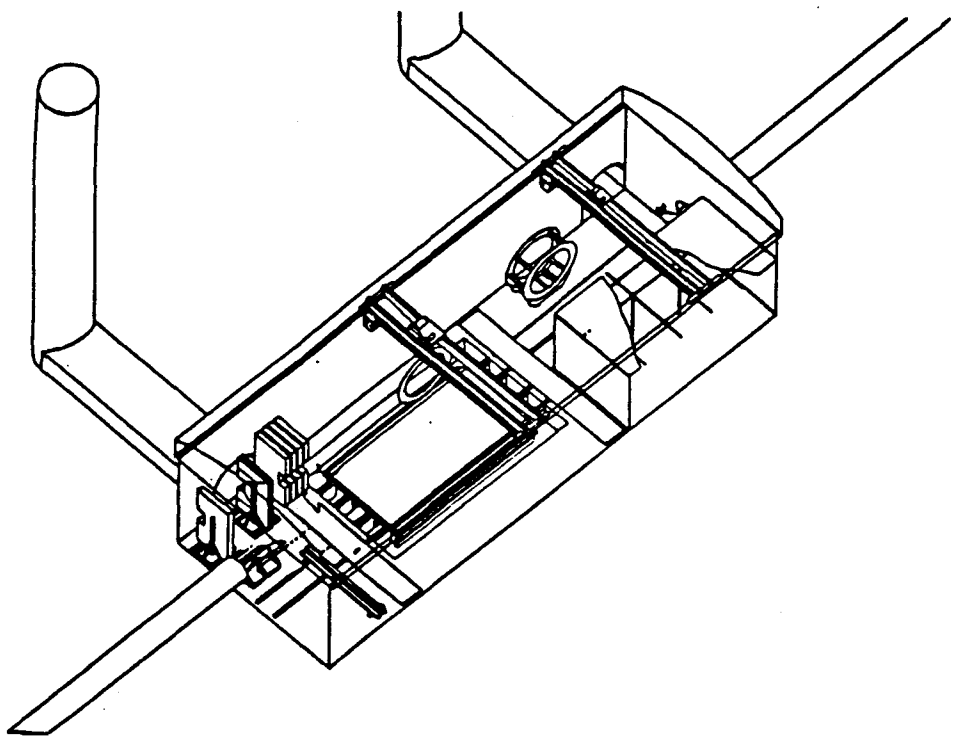

FIG. 44. State of the hall and detector 6 months after beneficial occupancy of the hall.

Figure 45 is the same view of the hall 12 months into the construction of the detector. Proceeding as above we see (*a*) the beginning of the third intermediate-angle toroid half-section, (*b*) the floor and two completed walls of the barrel muon toroids (including temporary bracing), (*c*) two completed intermediate-angle toroid half-sections in storage locations, and (*d*) two completed central calorimeter bays and a third under construction. The two completed calorimeter bays have been moved into a closed room for debugging and cosmic-ray testing. Sufficient space (approximately 3 m) has been left around each of these bays to allow access along all surfaces by personnel.

The state of the hall after 18 months is shown in Figure 46. Here the last of the muon intermediate-angle toroid half-sections is being assembled, the "roof" of the barrel

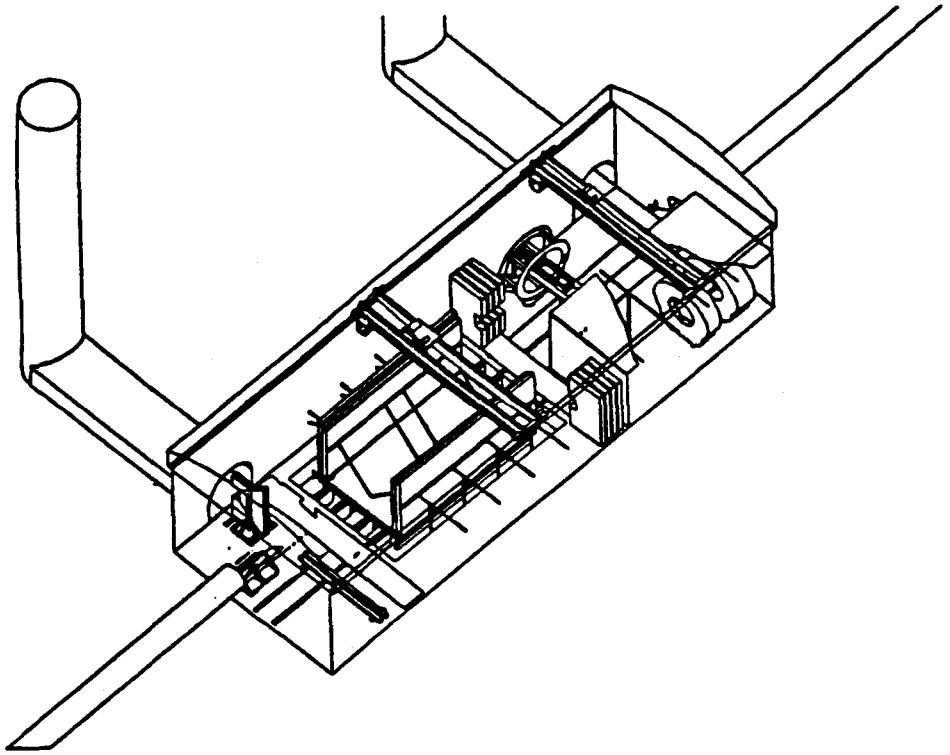

FIG. 45. State of the hall and detector 12 months after beneficial occupancy of the hall.

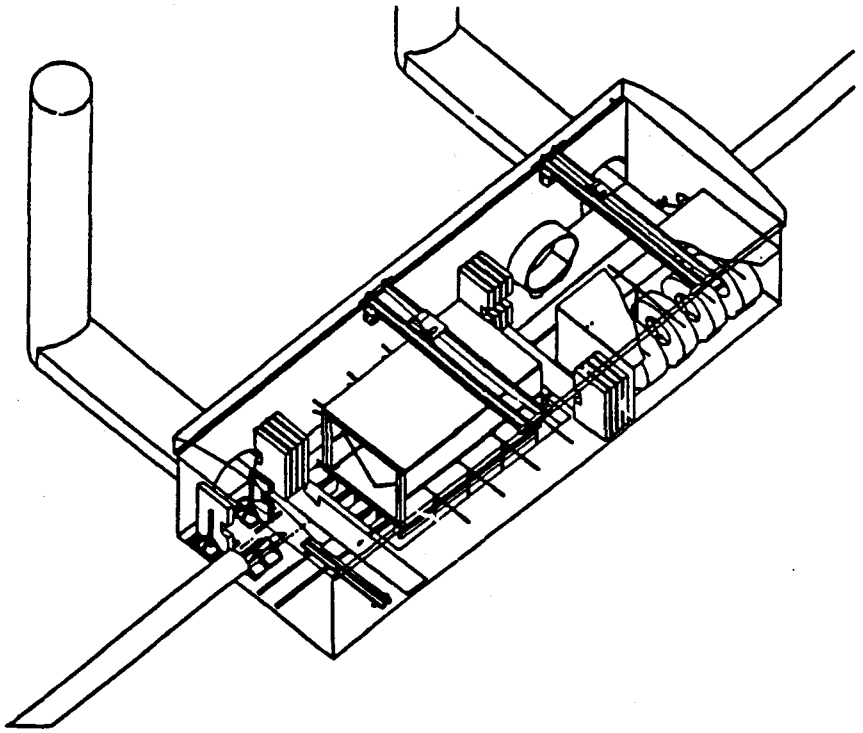

FIG. 46. State of the hall and detector 18 months after beneficial occupancy of the hall.

muon toroid has been fabricated but not yet lowered into place, four calorimeter bays are complete, and the last endcap calorimeter bay is being assembled.

At each stage in the construction, care has been taken to insure that fixtures and equipment can be brought into the hall efficiently and without conflicting with other work. For example, while the coils on the barrel muon toroids are being tested, the iron-rigging crews are assembling the muon intermediate-angle toroids. Studies of the remaining assembly sequence are continuing. These include completion of the calorimeter, insertion and field-mapping of the coil, installation of tracking systems, and assembly of the forward calorimeters and shielding. This study will also produce a preliminary list of the power and facilities requirements of the detector.

5.2. Test beam requirements

The plans for test beam work for the SDC detector can be summarized by dividing the need into the following categories: (*a*) R&D that has already begun and will for the most part be finished by the end of 1993; (*b*) prototype development that will mostly occur in the period 1992 to 1995; (*c*) system tests that will begin once prototypes are verified, and thus be done mostly during the period 1993 to 1997; (*d*) calibration that will start as soon as production versions of detector components are available and continue beyond the initial runs of the SDC detector (1995 to 2000). In these categories we anticipate the following needs (in hours of beam time).

Table 10

Anticipated test beam time needs for various subsystems (in hours).

Item	R&D	Prototyping	System Tests	Calibration
Calorimetry	2000	2000	2000	2000
Tracking	200	500	500	0
Muon System	Parasitic	500	500	0

A review of time that is expected to be available test beams in US laboratories is shown in Fig. 47. As can be seen, there is a serious shortage of potential test beam time before test beams are available at the SSC Laboratory, except for the 1993 fixed target run at Fermilab. This puts a premium on organizing efforts toward utilization of the current and 1993 fixed target runs at Fermilab. Once test beams are available at the SSC Laboratory, the SDC would expect to occupy full-time a minimum of one beam and will likely require at least part-time use of a second beam.

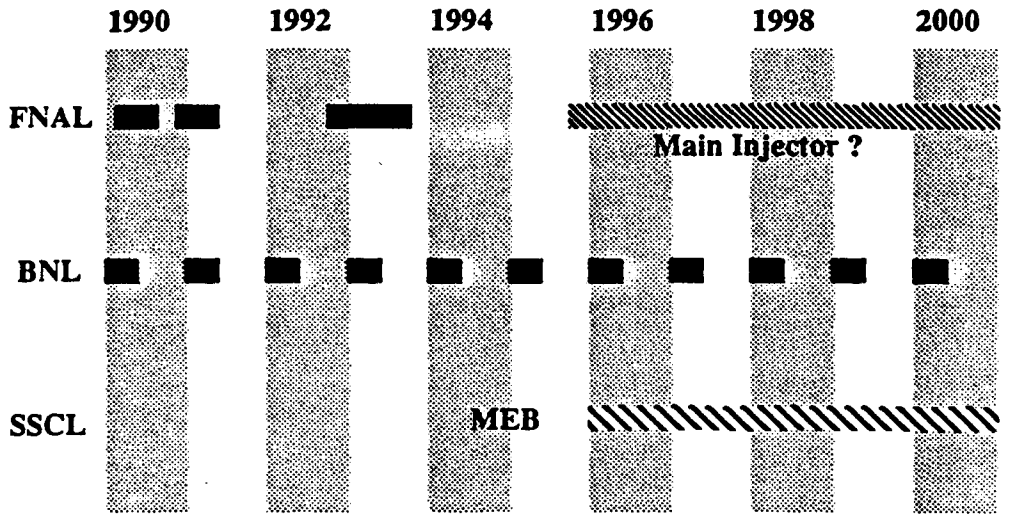

FIG. 47. Available test beam time at major laboratories during the next decade.

6. Detector cost and schedule estimates

We have made a preliminary estimate of the cost of the SDC detector and the results are given in Table 11. The total cost is about $630M in FY90 dollars. To arrive at this cost estimate, the short-solenoid design shown in Fig. 3 was selected as an example. We have used a methodology similar but not identical to that employed by a recent SSC detector cost panel[67]. In this procedure a matrix of unit costs of detector components at the simplest level and an equally simple parametrization of the detector in terms of tons, channels, *etc.* is used to arrive at a final cost. Two additional costs are then added: contingency and the cost of engineering, design and inspection (EDI). The latter is taken as 20% of the cost of the components, including contingency. We recognize that this type of cost estimate, at best, will give only a preliminary answer as to the cost of the detector. One of primary reasons for the request for support in this Expression of Interest is to obtain funding for making a conceptual design and preliminary engineering design in enough detail to obtain a reliable "bottoms-up" cost estimate for the SDC detector proposal.

Although we have used the methodology of the cost panel, we have also examined some of the unit costs in more detail. Differences from the unit cost matrix given in Ref. 67 are explained briefly below. We have accepted the remainder of the unit costs as given, pending a more detailed review by us.

We have received preliminary cost information that bears on the cost of steel for the muon system. These data indicate that the steel (including magnetizing coils) in the muon system will cost about $0.80/pound. This is nearly a factor of two larger than the estimate of SSC cost panel.

Based upon developments of application-specific integrated circuits (ASICs) supported under the SSC R&D program over the last few years, we have derived a new

Table 11

SDC detector cost estimate.

SYSTEM	UNIT	NO. OF UNITS	CODE	UNIT COST (000's)	SUBTOTAL	SUBSYSTEM SUBTOTAL	TOTAL	SUBSYS/TOTAL %
SPECIAL PURPOSE DETECTOR								
Si VERTEX(INCLUDES PIXEL DETECTOR)	METER**2	33	SVD2	1,000	33,000			
CONTINGENCY ON Si VERTEX (30%)					9,900			
						42,900		6.8%
TRACKING								
CENTRAL TRACKING - BARREL	KWIRES	251	TC1	100	25,100			
CENTRAL TRACKING - INTERMEDIATE	KWIRES	60	TC1	100	8,000			
CONTINGENCY ON TRACKING (30%)					9,330			
						40,430		6.4%
CALORIMETRY								
BARREL CALORIMETER	TONNES	3,414	C4	17	58,038			
END CALORIMETER (2)	TONNES	1,836	C4	17	31,212			
FORWARD CALORIMETER (2)	TONNES	75	C4	17	1,300			
RETURN YOKE STEEL	TONNES	2,153	MS1	2	3,596			
CONTINGENCY ON CALORIMETRY (30-40%)					26,374			
						122,519		19.5%
MUON DETECTORS								
MUON TRACKING, BARREL	METER**2	8,264	MS3	3	16,725			
MUON TRACKING, ENDS (2)	METER**2	1,336	MS4	5	7,132			
MUON SCINTILLATOR COUNTERS (3-LAYERS)	METER**2	8,926	TS1	1	5,542			
MUON MAGNETIZED Fe BARREL TOROID	TONNES	20,626	MS2	2	36,302			
MUON AIR CORE TOROIDS (2)	SYSTEM	2	AM4	20,000	40,000			
CONTINGENCY ON MUON DET. (30-40%)					35,710			
						141,411		22.5%
MAGNETS								
SUPERCONDUCTING SOLENOID	SYSTEM	1	AM2	25,000	25,000			
IRON TOROID POWER SUPPLIES (1)	SYSTEM	1	AM6	2,600	2,600			
He CRYO SUPPORT SYSTEM	SYSTEM	3	AM6	2,600	7,800			
CONTINGENCY ON MAGNETS (25%)					8,850			
						44,250		7.0%
ELECTRONICS								
CALORIMETRY 1 (EM & HADR. TOWERS)	KCHAN	90	E2	250	22,500			
CALORIMETRY 2 (PRE-RADIATOR)	KCHAN	10	E1	125	1,250			
MUON TRACKING	KCHAN	100	E1	125	12,500			
MUON SCINTILLATOR TRIGGER	KCHAN	14	E2	250	3,500			
CENTRAL TRACKING - BARREL	KCHAN	251	E1	125	31,375			
CENTRAL TRACKING - INTERMEDIATE	KCHAN	60	E1	125	7,500			
FORWARD CALORIMETRY	KCHAN	7	E2	250	1,750			
CONTINGENCY ON ELECTRONICS (50%)					40,188			
						120,563		19.2%
ON-LINE COMPUTING	SYSTEM	1	E7	10,000	10,000			
CONTINGENCY ON COMPUTING (25%)					2,500			
						12,500		2.0%
EDIA								
(20% OF ABOVE)						104,914		16.7%
				GRAND TOTAL(FY90 K$)			629,487	

unit cost estimate for electronics that will be used for central wire chamber tracking and muon tracking. These estimates include high voltage distribution, decoupling capacitors, thin film resistors, various ASICs (including radiation-tolerant ASICs where needed), active support for the electronics, cables to electronics outside the tracking volume, terminations, electronics (including controls) outside the tracking volume, trigger elements, data acquisition elements, prototype development, and installation of the electronics. The result is that we believe that a cost of $125 per wire channel is a reasonable estimate, as compared with $250 per wire assumed by the most recent cost panel. We have also applied this unit cost to wire electronics for muon tracking, although the estimate has been made assuming the more demanding environment in the central tracking region.

Our preliminary estimate of the cost of the superconducting solenoid is $25M. Advanced Cryomagnetics, Inc., working with ANL, has estimated the cost of each superconducting toroid to be $20M.

The cost of the silicon vertex detector has been estimated on the basis of a cost per square meter of instrumented silicon, rather than as a lump sum as was done by the SSC cost panel. The calorimeter parameters and costs that appear in Table 11 are appropriate for a lead-liquid argon calorimeter. If a Pb/Fe scintillator calorimeter model were used instead, the total detector cost estimate would be the same to within a few percent. Calorimeter costs include the cost of a preradiator system. Our present estimate does not include the possibility of using uranium. For calorimeter electronics we have continued to use $250 for tower readout including all cables, installation, trigger, DAQ, etc. but have reduced the cost of the strip or pad readout for preradiators or detectors near shower maximum to the $125 per channel cost.

The design of the SDC detector is at a very early stage. Nevertheless we feel that it is appropriate to include contingency in our cost estimate and have made a very preliminary analysis of the contingencies required for each of the detector subsystems. The contingency factors are given in Table 12 and reflects our judgement about the level of risk associated with each system.

Using the unit costs given in Table 11, the contingency factors given in Table 12, and the EDI cost at 20%, we obtain the cost estimates given in Table 11. The total cost is about $630M in FY90 dollars.*

The construction schedule for the SDC detector is also at a rudimentary stage. A high-level schedule is shown in Fig. 48 and is based upon an SSC turn-on date in late 1998.

Clearly a detailed schedule requires choice of key technologies and sufficient engineering design to make a credible assignment of durations. The budget request in this EoI will support, in part, the design and engineering work needed to make this assessment.

* We have not corrected the unit costs obtained by the panel or as modified by us to take account of escalation between FY89 and FY90. The uncertainties in these estimates are much greater than the few percent escalation factor.

Table 12

Preliminary contingency factors for the subsystems of the SDC detector.

Silicon detector + electronics	30%
Inner tracking	30
Solenoid	25
Calorimetry ($\|\eta\| < 3$)	30
Muon iron, chambers, scintillator	30
SC toroids + chambers	40
Forward calorimetry	40
Electronics/DAQ/trigger	50
On-line control/monitor	25

We recognize that the overall SSC schedule is uncertain and that new information about the schedule will become available by summer of this year. It is the goal of the SDC collaboration to have an operational detector ready to take data when the collider is first capable of delivering beams for experiments. Our choices of technology and detector parameters will be made to meet this goal, taking into account a realistic appraisal of the SSC construction schedule.

7. Organization and management of the collaboration

7.1. Governance

The U.S. part of the Solenoidal Detector Collaboration grew out of several initially independent efforts centered at LBL, ANL, and Fermilab, all of them with strong university participation. These efforts were all aimed at the design of a solenoidal detector for high-p_t physics at the SSC. At the same time, a large number of Japanese high-energy physicists organized and participated in a series of workshops in Japan aimed at the design of a large SSC detector, also based on a solenoidal magnet. At a workshop in September 1989, the various groups decided to combine their activities and develop a single EoI. An international Interim Steering Committee was set up whose principal tasks were the preparation of a governance document and the setting up of an appropriate collaboration management structure. A draft version of the governance document was extensively discussed at the first collaboration meeting in mid-December at Fermilab, and a final version was subsequently ratified by a large majority of the collaborators. Because of space limitations, we do not submit the actual governance document as part of this EoI, but simply summarize the main elements of the management structure. These consist of two representative groups, the Institutional and Executive Boards, a Spokesperson with three Deputy Spokespersons, and a technical organization. The Institutional Board with one representative from each collaborating institution deals with general policy issues.

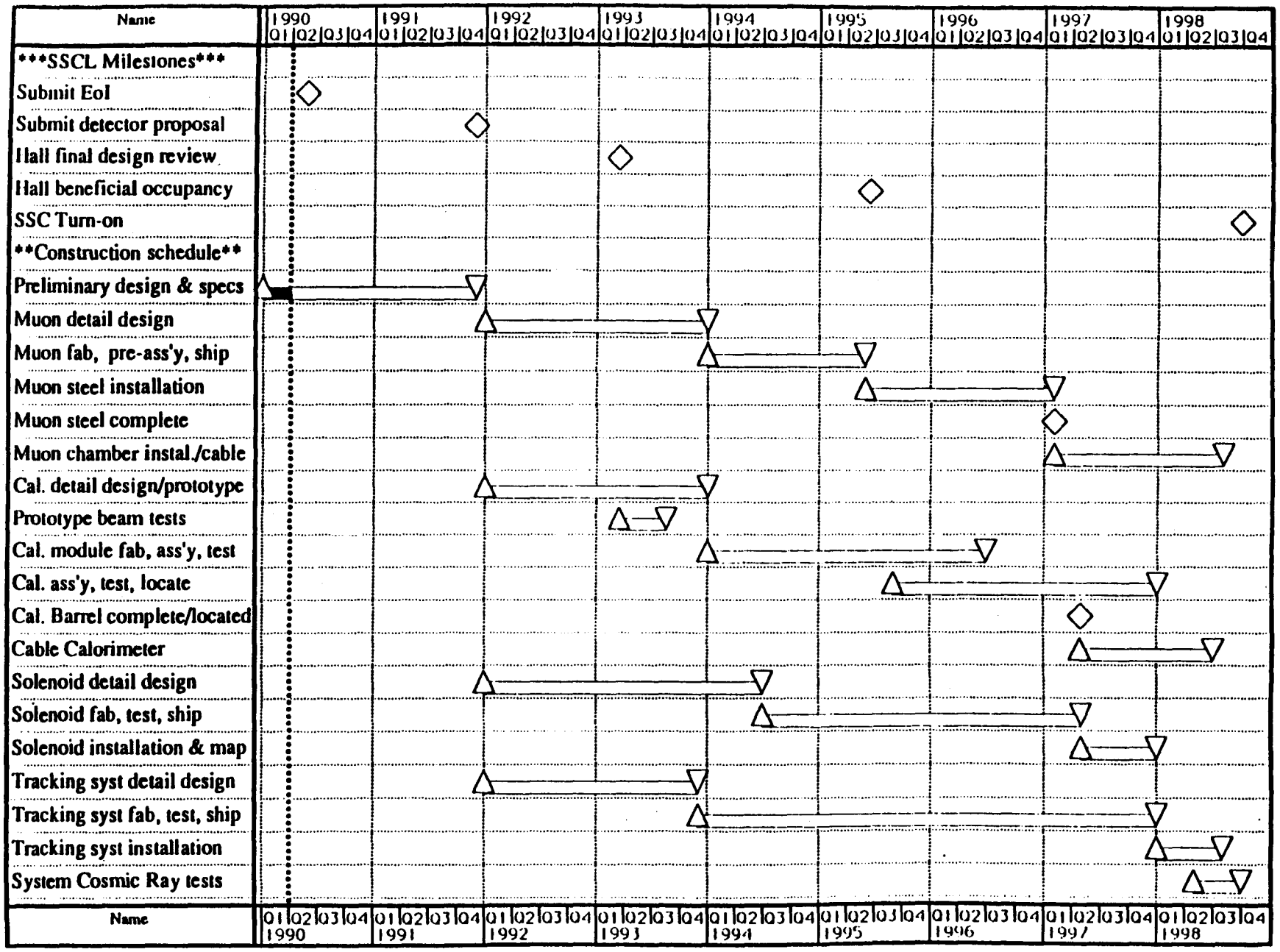

FIG. 48. Construction schedule for the SDC detector.

4/90

The Executive Board with seventeen members, elected by the collaborators, provides, in concert with the Spokesperson, the scientific direction of the experiment. The Executive Board membership includes seven from outside the U.S. The Executive Board appoints the Spokesperson, the Deputies, and approves other major appointments. The Spokesperson is the representative of the collaboration in scientific, technical, and managerial concerns. The three Deputy Spokespersons, from Japan, Europe, and the U.S./Canada, provide support and assistance to the Spokesperson. The technical organization consists of a Technical Manager, Technical Board, and Technical Steering Committees for the various detector subsystems. In addition, the research activities funded through the subsystem R&D programs have their own spokespersons.

7.2. Structure and Responsibilities

The principal officers of the SDC are listed at the top of Table 13. Their terms of office extend through the proposal approval period (unless there is major restructuring arising from the EoI process). To guide the development of the SDC proposal, a series of technical steering committees associated with the various subsystem areas have been organized. Their Co-Chairpersons are also shown in Table 13. The membership of these steering committees is in the process of appointment. The Co-Chairpersons together with the Spokesperson, Deputy Spokespersons, and Technical Manager constitute the Technical Board for the Collaboration. It is expected that technical decisions in the various subsystems will be made by the relevant steering committees in consultation with the appropriate experts and the Technical Manager. For making choices between different technologies, we expect that recommendations will be made by the steering committees augmented by additional technically knowledgeable members of the collaboration appointed by the Spokesperson in consultation with the Technical Manager and the Executive Board. As required by the Collaboration By-Laws, a written document giving a detailed analysis of the basis for the recommendation will be prepared, and presented for discussion at a collaboration meeting. The decision will be made by the Spokesperson and approved by the Executive Board.

7.3. Procedures for Admission of New Members

It is the responsibility of the Collaboration Institutional Board to set up the process for the admission of new collaborators. As of now only an interim procedure applicable up to EoI submission has been put in place. This consists simply of asking the candidate institutions to provide lists of potential collaborating scientists, and allowing two weeks for comments from the collaboration, to be followed by an electronic ballot by institutions. Approval by 75% of the collaborating institutions leads to immediate admission. Approval by less than 75% would lead to further discussion at the next collaboration meeting, with a subsequent ballot.

Table 13

Management for the Solenoidal Detector Collaboration

SPOKESPERSON:

G. Trilling (LBL)

DEPUTY SPOKESPERSONS:

G. Bellettini (University of Pisa)
D. Green (FNAL)
T. Kondo (KEK)

TECHNICAL MANAGER:

M. Gilchriese (LBL)

EXECUTIVE BOARD:

D. Bintinger (SSCL)
S. Errede (U. Illinois)
G. Feldman (Harvard)
E. Gabathuler (U. Liverpool)
G. Hanson (U. Indiana)
K. Kondo (Tsukuba U.)
S. Mori (Tsukuba U.)
Y. Nagashima (Osaka U.)
T. Ohsugi (Hiroshima U.)
L. Price (ANL)
R. Ruchti (U. Notre Dame)
A. Seiden (UCSC)
R. Thun (U. Michigan)

CHAIRPERSONS OF TECHNICAL STEERING COMMITTEES:

Calorimetry
A. Maki (KEK)
L. Nodulman (ANL)
M. Strovink (tentative) (LBL)

Computing and analysis software
K. Amako (KEK)
A. Baden (U. Maryland)
L. Price (ANL)

Detector integration and experimental facilities
J. Cooper (Fermilab)
R. Kadel (LBL)

Electronics, data acquisition, and trigger
M Campbell (U. Michigan)
A. Lankford (SLAC)
W. Smith (U. Wisconsin)
Y. Watase (KEK)
H. H. Williams (U. Pennsylvania)

Muon systems
G. Feldman (Harvard U.)
S. Mori (Tsukuba U.)
R. Thun (U. Michigan)

Physics and detector performance
K. Kondo (Tsukuba U.)
L. Price (ANL)
J. Siegrist (SSCL)

Superconducting magnets
R. Kephart (Fermilab)
A. Yamamoto (KEK)

Tracking
J. Elias (Fermilab)
W. Ford (U. Colorado)
T. Ohsugi (Hiroshima U.)

8. Preparation of the proposal and budget request

Preparation of the proposal for the SDC detector will require the efforts of all of the physicists in the collaboration and the diligent work of a large engineering team. We are requesting funds in this EoI to support, in part, engineering design leading to a full conceptual design and related cost and schedule estimates for the construction of the SDC detector. It is our assumption that essentially all of the research and development on detector components that will be used in the SDC detector will be supported by funds provided through subsystem R&D proposals in FY91. A significant part of the engineering needed to prepare a proposal will come from existing resources in the US or from institutions in the collaboration outside the United States. Our budget request only covers the additional, critical engineering to be done in the United States.

Table 14

The schedule for preparation of cost and schedule estimates for the SDC detector and for preparation of the proposal. It is assumed that the proposal is due in November of 1991.

Milestone	Date
Establish technical management procedures	June 1990
Review SSCL schedule	July 1990
Establish preliminary WBS	Oct. 1990
1st cost estimate for proposal	Nov. 1990
1st schedule estimate for proposal	Dec. 1990
Internal review of cost and schedule	Jan. 1991
2nd cost and schedule	Apr. 1991
2nd review of cost and schedule	May 1991
Final cost and schedule and review	Sept. 1991
Proposal outline	Mar. 1991
1st draft of proposal	May 1991
Review draft	June 1991
2nd draft of proposal	Aug. 1991
Final draft of proposal	Sept. 1991
Final internal review of proposal	Oct. 1991
Submit proposal to SSCL	Nov. 1991

8.1. Preparation of the proposal

Our schedule for the preparation of the proposal is shown in Table 14. This timetable is closely linked to the schedule for review of technology R&D and definition of key detector parameters and technologies that is presented later. Preparation of a credible cost estimate and construction schedule is a key component of the preparation of the proposal. There will be a close linkage between the choice of detector parameters and the cost. Hence we will set up a number of formal stages of internal cost review, emphasizing the tradeoffs between physics performance and cost. We recognize that the cost of the SDC detector will be approximately one order of magnitude greater than any previous US collider detector. To adequately justify this expenditure will inevitably require more effort than before and no doubt more reviews. In this regard, we have assumed that there will be a major cost and schedule review by the SSCL and/or DOE of the SDC detector design 6-9 months after acceptance of the proposal. Part of our budget request is to allow us to adequately prepare cost and schedule estimates for the proposal as a basis for more detailed work later.

In previous sections we have presented designs, often alternative designs, for the components of the SDC detector and preliminary design options for the overall detector, upon which our present cost estimate has been based. Although the basic concept of a solenoidal detector is clear, all of the key dimensions and parameters remain to be fixed and key technology choices remain to be made. The basic viability, not to mention detailed design, of important tracking and calorimeter technologies is uncertain and more R&D is needed to remove this uncertainty. We do not believe it possible to present at this time a credible schedule for selection of every important technology in the SDC detector (or for that matter any other 4π general purpose SSC detector). An important ingredient in this determination is also the overall SSC schedule, about which new information will become available subsequent to a DOE review in June.

We have established a timetable to review important technologies, to fix key dimensions for preparation of the proposal and to do preliminary engineering design in preparation for cost and schedule estimates. The timetable is given in Table 15. For most of the major subsystems, the intent is to review R&D, prepare a conceptual design, prepare a cost estimate, do preliminary engineering if appropriate and iterate on this process. The key goals in CY90 are to select a solenoidal magnet geometry (a choice between Types S/I or L), to define the tracking volume for the purposes of the proposal and to develop a conceptual design of the muon system leading to preliminary engineering design of muon steel and toroids. In CY91, some of the key goals will be to develop an integrated conceptual design of the tracking system, a preliminary engineering design of the superconducting solenoid, preliminary engineering designs for the calorimeter system, with different options if necessary, and a conceptual design of the electronics, data acquisition and trigger system. We will make a selection of or reduction in the number of calorimeter technologies in CY91 if our appraisal of the SSC schedule and of the feasibility of various calorimeter technologies indicates the need to do so.

Table 15

Timetable for technical decisions and review in preparation for a proposal for the SDC detector.

Milestone	Date
Solenoidal magnet related:	
Select geometry (Type S/I or L)	Sept. 1990
Fix tracking volume	Nov. 1990
Start preliminary engineering design	Nov. 1990
Complete preliminary engineering design	Apr. 1991
Review design	May 1991
Fix design for proposal	Aug. 1991
Tracking ($\|\eta\| < 3$):	
R&D review	July 1990
1st conceptual design, with options	Oct. 1990
Review conceptual design	Nov. 1990
Start preliminary engineering designs	Nov. 1990
Interim design review	Feb. 1991
Complete preliminary engineering designs	May 1991
Review design	June 1991
Reduce options, if necessary	July 1991
Fix design for proposal	Aug. 1991
Calorimetry ($\|\eta\| < 3$):	
R&D review	July 1990
1st conceptual designs	Oct. 1990
Review conceptual designs	Nov. 1990
Start preliminary engineering designs	Nov. 1990
1st interim design review	Jan. 1991
2nd interim design review	Mar. 1991
Complete preliminary engineering designs	May 1991
Review preliminary engineering designs	May 1991
Reduce options, if necessary	June 1991
Revise preliminary design	Aug. 1991
Fix design for proposal	Sept. 1991
Muon system ($\|\eta\| < 3$):	
Complete conceptual design	Sept. 1990
Review conceptual design	Oct. 1990
Start preliminary engineering design of iron	Nov. 1990
Start preliminary engineering design of tracking	Dec. 1990
Initiate feasibility study of SC toroids with industry	Dec. 1990
Interim review	Feb. 1991
Complete preliminary design of iron	Mar. 1991
Complete preliminary design of tracking	Apr. 1991
Complete feasibility study of SC toroids	May 1991
System review	May 1991
Revise design and review	Aug. 1991
Fix design for proposal	Sept. 1991
Forward system:	
1st conceptual design	Jan. 1991
Review conceptual design	Feb. 1991

Start preliminary engineering design	Mar. 1991
Interim review	May 1991
Complete preliminary engineering design	July 1991
Review preliminary design	Aug. 1991
Fix design for proposal	Aug. 1991
Electronics, data acquisition, and trigger:	
Review of design status and R&D	July 1990
Define trigger (physics) requirements	Aug. 1990
Define overall requirements	Sept. 1990
1st overall system conceptual design	Jan. 1991
Review conceptual design	Jan. 1991
Define subsystem requirements	Feb. 1991
Review subsystem requirements	Mar. 1991
Finish subsystem conceptual design	June 1991
Revised overall system conceptual design	July 1991
Review conceptual design	Aug. 1991
Fix designs for proposal	Aug. 1991
Computing, networking and software:	
Establish video links (LBL, ANL, FNAL, SSCL)	Aug. 1990
Review simulation effort	Aug. 1990
Define goals for simulation effort	Sept. 1990
Review goals	Oct. 1990
Assign responsibilities for simulation	Nov. 1990
Conceptual design of software framework	Jan. 1991
Review conceptual design of software framework	Feb. 1991
Assignment of subtasks	Mar. 1991
Review of simulation effort	Mar. 1991
Complete initial simulations	May 1991
Revise simulation results	July 1991
Revised conceptual design of software framework	July 1991
Review conceptual design of software framework	Aug. 1991
Complete simulation for proposal	Sept. 1991
Fix software description for proposal	Sept. 1991

Institutions within the collaboration will assume responsibilities for meeting these goals and for preparing the proposal. A few subcontracts to industry will also be needed. A matrix of responsibilities and tasks or subsystems is shown in Table 16. The institutions in the collaboration will assume the responsibility for performing the relevant research and development and for conceptual and engineering design. Most of the support for these activities is expected to be forthcoming from the major subsystems R&D program and from existing resources, except as presented in the next section. As design and technological choices are made, the assignment of responsibilities will change accordingly, leading to institutional responsibilities for construction of components after approval of the proposal.

Table 16

Technical responsibilities in preparation of the proposal. The last column indicates if funds are requested in this Expression of Interest. In most cases support for research and development and design is assumed to be provided via funding for major R&D subsystems proposals or by other sources.

Responsibility	Institutions	Comments	EoI funds Requested?
Mechanical and System Design			
Accelerator interface	SSCL	Final focus quads	No
Pixel detector array	LBL, U. of Hawaii	R&D under subsystems program	No
Silicon strip array	UC Riverside, UC Santa Cruz, Hawaii, Johns Hopkins, Pittsburgh, FNAL, LBL, LANL, Dubna Hiroshima U, Hiroshima Inst., KEK, Nagoya U.,Niigata U., Pisa, Oxford, RAL	R&D and preliminary engineering design under subsystems program	No
Central tracking wire chambers	U. Colorado, Duke Florida State, U. of Florida, Indiana, KEK, LANL Liverpool, U. of Michigan, ORNL, RAL, Texas A&M	R&D and some engineering under subsystems program.	No
Scintillating fibers for tracking	FNAL, U. of Illinois at Chicago, U. of Illinois at Urbana, Notre Dame, ORNL, Osaka City U., Penn. State, Rice, UT Dallas, U. of Tsukuba, UCLA, Purdue, Johns Hopkins	R&D under subsystems program	No
Integration of tracking systems	LANL, LBL, ORNL, Westinghouse	Overall mechanical and electrical integration	Yes
Superconducting solenoid	FNAL, KEK U. of Tsukuba	Preliminary design	Yes
Muon iron and chamber supports	SSCL,PSL, KEK, FNAL	Preliminary design	Yes
S. C. muon toroids	ANL, FNAL, U. of Tsukuba	Feasibility study	Yes
Muon tracking chambers	Arizona, ANL, U. of Colorado, FNAL, Harvard, U. of Illinois, KEK, U. of Michigan, U. of Minnesota, Osaka City U., Rice, Rochester, U. of Tsukuba Tufts, U. of Washington, Wisconsin, Maryland, Brandeis	R&D under subsystems program	No

Calorimetry R&D and preliminary engineering design

Liquid argon	FNAL, KEK Florida State, LBL, U. of Maryland, U. of Mississippi, ORNL, Rochester, Tokyo Inst. of Tech. U. of Washington, Dubna	R&D and preliminary engineering under subsystem program.	No
Warm liquid	Brandeis, LBL FNAL, Florida State, Harvard, Kyoto U., Niigata U. U. of Penn., Tohoku U., Tohoku Gakuin U., Saitama Health U.	R&D and preliminary engineering design under subsystem program	No
Scintillating Plate	ANL, Florida, FNAL State, U. of Miss., ORNL, VPI, FNAL, U. of Wisconsin, Purdue Tokyo Metro. U., Dubna	R&D and preliminary engineering design under subsystem program	No
Scintillating Fiber	FNAL, KEK, Purdue, Rockefeller Rutgers, UC San Diego, U. of Illinois, U. of Michigan, U. of Rochester, U. of Tsukuba, U. of Washington, Saga U. Texas A&M	R&D and preliminary engineering design under subsystem program	No
Integration of calorimeter systems	ANL,FNAL,LBL KEK, Westinghouse	Overall mechanical and electrical integration	Yes

Electronics and Related Systems Design and Preliminary Engineering

Detector Specific Front End Electronics

Pixel Detector Array	See above	Covered under system	No
Silicon Strip Array	See above	Covered under system	No
Wire chambers	KEK, Oxford, U. of Penn, RAL Univ. of Michigan Liverpool	Some aspects covered under subsystem R&D.	No
Scintillating fibers	FNAL	Covered under system	No
Calorimetry	ANL, FNAL, LBL, KEK, Harvard	Some aspects covered under subsystem R&D	No

Data Acquisition System

All aspects	Brown, Illinois, RAL, Univ. of Penn., Washington, Univ. of Colorado, ANL, FNAL, KEK, LBL, Fukui U., U. of Mississippi	Conceptual design and some preliminary engineering design	Yes

Trigger System

All aspects	FNAL, Oxford, Brown RAL, Univ. of Penn. ANL, Pisa, U. of Tsukuba, Univ. of Michigan,Wisconsin, Univ. of Chicago, KEK, LBL, U. of Mississippi	Conceptual design and some preliminary engineering design	Yes

Computing and Software Development

Physics simulation	ALL	For detector design and evaluation of performance	No
Development of multiprocessor UNIX-based system	SSCL, FNAL KEK	Assist in providing software for utilizing large UNIX-based system at SSCL for simulation	No
Networking and video coordination	ANL, FNAL, LBL SSCL, KEK, Tohoku U.	Develop and implement advanced networking and video conferencing strategy	Yes
Analysis software	ALL	Develop overall software framework	Yes

Project Coordination and Administration

Experimental facilities interface	SSCL, FNAL, LBL	Work with SSCL to define facilities requirements	Yes
Technical managment and project coordination	LBL, SSCL	Coordination by spokesman and technical management	Yes
Reserve	LBL, SSCL	Funds reserved to adapt to rapidly developing detector design	Yes

8.2. BUDGET REQUEST

Our budget request for FY91 is given in Table 17. As we have already noted, the funding request will cover only a small fraction of the required effort. Our funding level request assumes an expansion in FY91 of the subsystems R&D program by about a factor of two to cover critical R&D issues associated with detector subsystems. In this regard Table 16 is a better representation of the very broad efforts of the collaboration, whereas Table 17 reflects only the immediate need for modest additional support of engineering and coordination activities.

Table 17

SDC budget request for FY91

	OPERATING(K$)	EQUIPMENT(K$)
Integration of tracking systems - LANL, LBL, ORNL, Westinghouse†	775	155
Superconducting solenoid design - FNAL	80	20
Superconducting toroid design - ANL, FNAL, industrial partner	375	10
Muon iron and chamber support design - FNAL, Univ. of Wisconsin(PSL)†	225	60
Integration of calorimeter systems - ANL, FNAL, LBL, Westinghouse†	725	150
Data acquisition and trigger systems design - Univ. of Chicago, FNAL, LBL, Univ. of Michigan, Univ. of Wisconsin	500	285
Video/networking - ANL, FNAL, LBL	45	150
Software engineering - ANL, FNAL, LBL	400	55
Technical coordination and management - LBL	800	110
Project reserve - LBL, SSCL	700	650
GRAND TOTALS	4625	1645

† Additional involvement is anticipated by many university groups in the design of these systems and the development of prototypes.

Our funding request covers a fraction of the systems-level design integration required for tracking and calorimetry, primarily mechanical systems and mounting and cabling of electronics. We are also requesting funds to aid in the preliminary design of the superconducting solenoid, much of which will occur via work at KEK, and to begin a feasibility study of superconducting air-core toroids with an industrial firm, which is yet to be selected. We expect to complete a preliminary design of the iron structure and chamber

supports required for the muon system by the time the proposal is submitted. This will be a joint effort of Fermilab, KEK, the SSC Laboratory and the Physical Sciences Laboratory (PSL) at the University of Wisconsin. We are also requesting funds to support data acquisition and trigger design related specifically to the SDC detector. These areas, particularly the trigger aspects, have received very little support in the subsystems R&D program and are critical to the success of our detector. Funds to support videoconferencing equipment are also requested. The collaboration is now using videoconferencing systems at LBL, Fermilab, and the SSC Laboratory, and we anticipate a very substantial increase in this use, leading to the need for dedicated equipment for the SDC. It is essential that such connections also be established with Europe and Japan. A video link between Pisa and Fermilab is being planned by the Italian CDF group. Its capability will have to be expanded for the SDC effort. A connection to Japan is being studied, and will be implemented as soon as possible.

Support for professional software engineering leading to an integrated software framework for the analysis and other software of the collaboration is also requested. Funds for technical coordination by the Spokesperson and the technical management of the collaboration would support systems-level engineering and coordination of the overall detector design, personnel for cost and schedule estimates and some administrative needs. Finally, we believe that it is imperative to have a reasonable reserve to be able to respond to a very rapidly changing situation in FY91. Our detector design will proceed rapidly, leading to a number of technological choices for which additional R&D, design work, and prototype development will be needed. Funding provided by the major subsystems R&D program will not cover this work.

9. References

1. CDF Collaboration, *Proc. 25th Rencontres Moriond: Electroweak Interactions and Unified Theories* (1990); H. Jensen, Invited talk at the APS meeting, Washington DC, April 1990.
2. P. Langacker, in Particle Data Group, "Review of Particle Properties," Phys. Lett. (to be published 1990).
3. Y. Takaiwa, "Effects of Non-uniform Magnetic Field on Tracking", Proceedings of the International Workshop on Solenoidal Detectors, KEK (25 April 1990).
4. L. R. Cormell and G. P. Yost, "Accelerator Parameters Relevant to Detector Design", SSC Laboratory Report SSCL-264 (April 1990).
5. "Report of the Task Force on Radiation Levels in the SSC Interaction Regions," ed. by D. E. Groom, SSC Central Design Group Report SSC-SR-1033 (June 1988).
6. D. E. Groom, *Proc. of the 1988 Summer Study on High Energy Physics in the 1990's,"* ed. by F. J. Gilman and S. Jensen, Snowmass CO, July 1988 (1989).
7. D. E. Groom, "Report of the Task Force on Radiation Testing," ed. by R. Thun, SSCL Report, (to be published, 1990).
8. T. A. Gabriel and R. A. Lillie, SSC Central Design Group Note SSC-N-545 (1988).
9. "SSC Site Specific Conceptual Design Report (Draft), SSC Laboratory (May 1990).
10. "Report of the Ad Hoc Committee on SSC Physics," SSC Laboratory Report SSC-250 (December 1989).

11. "The Feasibility of Experiments at High Luminosity at the Large Hadron Collider," J. H. Mulvey, ed., CERN 88-02 (1988).

12. S. Parker, Nucl. Instrum. Methods **A275**, 494 (1989).

13. "SSC Detector R&D Proposal: Development of Technology for Pixel Vertex Detector," (Spokesperson: D. Nygren) (1989).

14. D. R. Nygren, "Silicon Tracking Devices for the SSC, *Proc. of the 1988 Summer Study on High Energy Physics in the 1990's*, ed. F. J. Gilman and S. Jensen, Snowmass, Colorado, July 1988 (1989).

15. G. Kramer *et al.*, "Silicon PIN Diode Hybrid Arrays for Charged Particle Detection: Building Blocks for Vertex Detectors at the SSC," 1989 International Industrial Symposium on the Super Collider, New Orleans LA (Feb. 8–10, 1989) (SLAC-PUB-4942).

16. S. Holland and H. Spieler, "A Monolithically Integrated Detector-Preamplifier on High-Resistivity Silicon," to be published in IEEE Trans. Nucl. Sci. (April 1990).

17. "Subsystem R&D Proposal to Develop a Silicon Tracking System," pp. 25–28 (Spokesperson: A. Seiden) (1989).

18. G. G. Hanson, B. B. Niczyporuk and A. P. T. Palounek, Nucl. Instrum. Methods **A283**, 735 (1989).

19. D. G. Cassel, G. G. Hanson *et al.*, "Report of the Central Tracking Group," *Proceedings of the 1986 Summer Study on the Physics of the Superconducting Supercollider*, ed. by R. Donaldson and J. Marx, Snowmass, CO (1986), p. 377.

20. G. A. Beck *et al.*, Nucl. Instrum. Methods **A283**, 471 (1989).

21. H. Grässler *et al.*, Nucl. Instrum. Methods **A283**, 622 (1989); S. Ahlen *et al.*, "Proposal to Develop an Integrated High-Rate Transition Radiation Detector for the SSC," SSC PC-011 (October 1989); B. Dolgoshein, "The Transition Radiation Detector for High-Lorentz-Factor Particle Identification at High-Luminosity Hadron Colliders," *Proc. of the ECFA Study Week on Instrumentation Technology for High-Luminosity Hadron Colliders*, Barcelona, Spain (1989), p. 650.

22. *Proc. of the Workshop on Scintillating Fiber Detector Development for the SSC*, Vol. 1 & 2 (Nov. 1988).

23. M. Atac, W. Foster, and M. Lundin, Fermilab Report FN-537 (Mar. 1990).

24. M. D. Petroff and M. G. Stapelbroek, IEEE Trans. Nucl. Sci. **NS-36**, 158 (1989); M. D. Petroff and M. Atac, IEEE Trans. Nucl. Sci. **NS-36**, 163 (1989).

25. S. Parker,"A Proposal to Develop a VLSI Pixel Device for Particle Detection" (31 May 1987); addendum (16 July 1987).

26. "SSC Detector Subsystem Proposal: Central and Forward Tracking with Wire Chambers."

27. "SSC Detector Subsystem Proposal: A Hybrid Straw Tube/Scintillating Fiber Tracking Detector."

28. "SSC Detector Subsystem Proposal: A Scintillating Fiber Tracking System."

29. "CDF Endcap EM Calorimeter Test Results," S. Mikamo *et al.*, *Proc. of the Gas Calorimeter Workshop*, Fermilab (1982), pg 22.

30. E. M. Wang, *Proc. of the Tuscaloosa Workshop on Calorimetry for the SSC*, ed. R. Donaldson and M. G. D. Gilchriese, Tuscaloosa AL (March 1989), World Scientific (to be published 1990).

31. S. Mori *et al.*, "HCD Hermetic Collider Detector," Institute of Applied Physics University of Tsukuba (Feb 1990).

32. T. Kondo, "An Air-Core Solenoidal Detector (ACS) for High p_t Physics at the SSC," Fermilab Workshop on Solenoidal Detectors for the SSC, Batavia IL (Sept. 1989).

33. *Proc. of the Workshop on Radiation Hardness of Plastic Scintillator*, Tallahassee FL (19–21 March 1990) (to be published.)

34. SSC Subsystem R&D Proposal: Front End Electronics Development for SSC Detectors (1989).

35. Y. Sakai, *Calorimeter First Level Trigger Rates at the SSC*, KEK preprint, (1990).

36. A. Lankford, E. Barsotti, and I. Gaines, in *Proceedings of the 4th Pisa Meeting on Advanced Detectors: Frontier Detectors for Frontier Physics*, La Biodola, Isola d'Elba, Italy (May 21–26, 1989), SLAC-PUB-5042, Nucl. Instrum. Methods (to be published 1990).

37. E. Barsotti *et al.*, "A Scaleable Parallel Open Architecture Data Acquisition System for Low to High Rate Experiments, Test Beams, and all SSC Detectors," IEEE Trans. Nucl. Sci. (to be published 1990).

38. R. Partridge, "An SSC Data Acquisition Architecture," to be published in *Proc. of Computing in High Energy Physics*," Santa Fe NM (Apr. 9–13, 1990).

39. I. Hinchliffe and M. D. Shapiro, SSC-SDE-35,"Parametrizations of Detector Resolutions for SDE"

40. Internal CDF note.

41. J. J. Gunion *et al.*, "The Higgs Hunter's Guide."

42. J. F. Gunion, G. Kane and J. Wudka, Nucl. Phys. **B299**, 293 (1988).

43. R. W. Brown and K. O. Mikaelian, Phys. Rev. **D19**, 922 (1979).

44. E. W. N. Glover and J. J. van der Bij, Nucl. Phys. **B321**, 561 (1989).

45. I. Hinchliffe and R. M. Barnett, Lawrence Berkeley Laboratory Report LBL-28273 (1990).

46. B. W. Lee, C. Quigg and H. Thacker, Phys. Rev. **D16**, 1519 (1977).

47. S. Weinberg, Phys. Rev. **D13**, 974 (1976); L. Susskind, Phys. Rev. **D20**, 2619 (1979).

48. R. S. Chivukula and M. Golden, Fermilab Report FNAL-Pub-89/256-T (1989).

49. I. Hinchliffe and M. D. Shapiro, SSC-SDE-36, "Z_η Production with the SDC Detector."

50. E. Eichten *et al.*, Rev. Mod. Phys. **56**, 579 (1984).

51. M. Mangano SSC-SDE-32, "Production of Techniomega $\rightarrow \gamma Z \rightarrow \gamma \ell^+ \ell^-$ "

52. M. S. Chanowitz and M. K. Gaillard, Nucl. Phys. **B261**, 379 (1985).

53. M. S. Chanowitz, Lectures at the 1989 SLAC Summer Institute, Lawrence Berkeley Laboratory Report LBL-27730.

54. D. Dicus and R. Vega, Nucl. Phys. Rev. **B329**, 533 (1990).

55. L. Galtieri, SSC-SDE-38, "Study of Top Pairs into $e\mu$ at SSC Energies"

56. G. Altarelli *et al.*, Nucl. Phys. **B308**, 724 (1988).

57. B. Hubbard, SSC-SDE-31, "Efficiency for b-jet Tagging in $t\bar{t}$ Events,"

58. R. J. Hollebeek, P. K. Sinervo and H. H. Williams, SDC-30

59. V. Barger *et al.*, "Signature for Extra Gauge Bosons of E_6 at the SSC" in *Proc. of the 1986 Snowmass Summer Study*, ed. J. Marx and R. Donaldson, FNAL (1987).

60. For a review, see I. Hinchliffe, Ann. Rev. Nucl. Part. Sci. **36**, 505 (1986).

61. R. M. Barnett, J. F. Gunion and H. E. Haber, Phys. Rev. *D37*, 1892,(1988).

62. R. M. Barnett E. Carlson and I. Hinchliffe, SSC-SDE-10, Lawrence Berkeley Laboratory Report LBL-27797.

63. E. Eichten, K. Lane and M. Peskin, Phys. Rev. Lett. **50**, 811 (1983).

64. F. Abe *et al.*, Phys. Rev. Lett. bf 62, 613 (1989).

65. M. Shapiro, SSC-SDE-37, "Study of Compositeness Signals at SSC Energies"

66. See, for example, "Workshop on Physics and Detector Simulation for SSC Experiments," SSC Laboratory, Dallas Texas.

67. "Cost Estimates of SSC Experimental Systems," SSC Laboratory Report SSC-SR-1045 (December 1989) (Draft).